

The Effects of Outgassing Through Cylindrical Walls on the Transport Coefficients

A Thesis
Submitted to the College of Engineering
of Nahrain University in Partial Fulfillment
of the Requirements for the Degree of
Doctor of Philosophy
in
Chemical Engineering

by

Luma Hikmat Yaseen

B.Sc. 1997
M.Sc. 2000

Jumada II
July

1427
2006

Certification

We certify that this thesis entitled " **The Effects of Outgassing through Cylindrical Walls on the Transport Coefficients**" was prepared by **Luma Hikmat Yaseen** under our supervision at Nahrain University/College of Engineering in partial fulfillment of the requirements for the degree of Doctor of Philosophy in Chemical Engineering

Signature: 

Name: **Prof. Dr. Nada B. Nakkash**
(Supervisor)

Date: 15/8/2006

Signature: 

Name: **Ass. Prof. Dr. Mohammed N. Latif**
(Supervisor)

Date: 15/8/2006

Signature: 

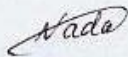
Name: **Prof. Dr. Q. J. Slaiman**
(Head of Department)

Date: 15/8/2006

Certificate

We certify, as an examining committee, that we have read this thesis entitled "**The Effects of Outgassing through Cylindrical Walls on the Transport Coefficients**", examined the student **Luma Hikmat Yaseen** in its content and found it meets the standard of thesis for the degree of Doctor of Philosophy in Chemical Engineering.

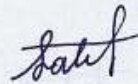
Signature:



Name: **Prof. Dr. Nada B. Nakkash.**
(Supervisor)

Date: 15/8/2006

Signature:



Name: **Ass. Prof. Dr. Mohammed N. Latif**
(Supervisor)

Date: 15/8/2006

Signature:



Name: **Ass. Prof. Dr. Balasim A. Abid**
(Member)

Date: 13/8/2006

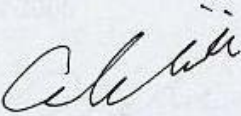
Signature:



Name: **Ass. Prof. Dr. Khalil E. Al-Jumaily**
(Member)

Date: 13/8/2006

Signature:



Name: **Ass. Prof. Dr. Cecilia K. Haweel**
(Member)

Date: 17/8/2006

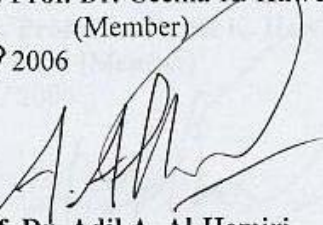
Signature:



Name: **Ass. Prof. Dr. Malek M. Mohammed**
(Member)

Date: 15/8/2006

Signature:

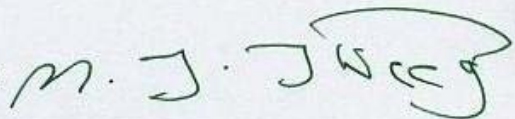


Name: **Prof. Dr. Adil A. Al-Hemiri**
(Chairman)

Date: 14/8/2006

Approval of the College of Engineering

Signature:



Name: **Prof. Dr. Muhsin J. Jweeg**
(Acting Dean)

Date: 29/8/2006

Abstract

Abundant data on the momentum, heat and mass transfer is available in the literature. Most of this data is confined to impermeable surfaces. It is known from studies concerning flat plates that blowing into the boundary layer can severely reduce the transport coefficients (friction factor, mass and heat transfer coefficients). This work studies the influence of blowing on the friction factor and mass transfer coefficient for the flow normal to a tube bank with outgassing porous cylinders. The friction factor and the mass transfer coefficients are measured for the investigated range of Reynolds number and blowing rate, and expressed in terms of various dimensionless groups.

A test rig was built for the present work purposes consists of a rectangular duct (20.3×11.3 cm). Five rows of three tubes of porous tube in staggered arrangements fixed across the duct with 1.5 pitches (both longitudinal and transversal). The outside and the inside diameters of the tubes were 25.4 and 21.4 mm respectively.

Measurements for the friction factor was done for $3000 < Re < 17,000$ and blowing rate up to 4×10^{-3} . It was found that the blowing into boundary layer for cylinders increase the overall friction factor from 10% up to 50% depending on the blowing rate.

The mass transfer coefficient was measured for $5000 < Re < 16,000$ and blowing rate $10^{-5} < \dot{m}/G_{\infty} < 10^{-3}$. A new definition for the blowing rate was

used and expressed by the mass transfer driving force. Two successful formulas were modified to account the outgassing effect on the mass transfer coefficient. The mass transfer coefficient for the outgassing boundary layer can be obtained by first determining the non-blowing coefficient and multiplying it with the correction factor ϕ . The first one modified to account the density variation associated with the boundary layer change and the final model obtained given as:

$$St_m Sc^{2/3} = \frac{0.51 Re^{-0.5} \left(\frac{\rho_s}{\rho_\infty} \right)^{0.4}}{(1 + \beta_m)^{4.7}}$$

With the coefficient of determination $R^2 = 0.93$.

The second model depends on the flat plate correction factor and the final formula for the model was:

$$St_m Sc^{2/3} = 0.5 Re^{-0.5} \left(\frac{\ln(1 + \beta_m)}{\beta_m} \right)^{9.94}$$

With the coefficient of determination $R^2 = 0.92$.

These two models are found to be in agreement with the literature data.

Reduction of about 80% in the mass transfer coefficient has been obtained due to the outgassing.

Table of Contents

Title	Page
Abstract	I
Table of Contents	III
Nomenclatures	VI
List of Tables	IX
List of Figures	X
Chapter One: Introduction	1
Introduction	1
Chapter Two: Literature Survey	4
2.1 Introduction	4
2.2 Basic Duct Hydraulics	4
2.3 Flow across Tube Banks	7
2.4 Effect of Transpiration on Transport Coefficients	11
2.4.1 Momentum Transfer	11
2.4.2 Heat Transfer	14
2.4.3 Mass Transfer	15
2.5 Review of Previous Works	17
Chapter Three: Transport Phenomena in Tube Banks	26
3.1 Introduction	26
3.2 Fluid flow in Tube Bank	26
3.2.1 Geometrical Description of a Tube Bank and General Definitions	26
3.2.2 Overall Pressure Drop	28
3.2.3 Friction Factor	29
3.2.4 Influence of Outgassing on the Pressure Drop	30
3.3 Heat Transfer	31
3.3.1 Definitions	31
3.3.2 Correlations	32
3.3.3 Influence of Outgassing on Heat Transfer	32
3.4 Mass Transfer	33
3.4.1 Definitions	33
3.4.2 Correlations	34
3.4.3 Influence of Outgassing on Mass Transfer	35
3.5 Analogies	35
Chapter Four: Experimental Work	41
4.1 Introduction	41

4.2 General Concepts	41
4.3 Experimental Facilities and Instrumentation	42
4.3.1 Experiment Apparatus	47
4.3.1.1 Induced Centrifugal Fan	47
4.3.1.2 Wind Tunnel	47
4.3.1.3 Air Rotameters	48
4.3.1.4 Water Rotameter	48
4.3.1.5 Digital Thermometers	48
4.3.1.6 Relative Humidity Meter	49
4.3.1.7 Pitot Tube	49
4.3.1.8 Pump	49
4.3.1.9 Water Bath	49
4.3.2 Test Section	49
4.3.2.1 Compressed Air Control	50
4.3.2.2 Pressure and Temperature Difference across the Test Section	51
4.3.2.3 Velocity Measurement	52
4.3.2.4 The Plastic Tube Bundle	53
4.3.2.5 PVC Flanges	53
4.3.2.6 Hot Water Control	53
4.4 Calibrations of the Instruments	54
4.4.1 Volumetric Air Flow	54
4.4.2 Rotameters	55
4.4.2.1 Air Rotameter	56
4.4.2.2 Water Rotameter	57
4.4.3 Thermometers	58
4.5 Measurement Procedures	61
4.5.1 Fluid Flow Test	61
4.5.2 Mass Transfer Test	62
Chapter Five: Results and Discussion	63
5.1 Introduction	63
5.2 Friction Factor Measurement	63
5.2.1 Friction Factor Measurement for non- Blowing Case	65
5.2.1.1 Comparison with Literature	68
5.2.1.2 Error Analysis	69
5.2.2 Friction Factor Measurement with Blowing	72
5.2.2.1 Friction Factor Measurement at Constant Blowing Factor	77
5.2.2.2 Friction Factor Measurement at Constant Reynolds Number	80
5.3 Mass Transfer	84
5.3.1 Mass Transfer Variables Measurements	85

5.3.2 Mass Transfer Results	86
5.3.2.1 Mass Transfer Data Presentation	86
5.3.2.2 Mass Transfer Correlations	94
5.3.2.3 Comparison with Literature	103
5.3.2.4 Error Analysis	106
Chapter Six: Conclusion and Recommendations	108
6.1 Conclusions	108
6.2 Recommendations	109
References	111
Appendices	
Appendix A: Physical Properties	A-1
Appendix B: Derivation of Kays and Crawford Correction	B-1
Appendix C: Results	C-1

Nomenclature

Symbols:

A	channel cross section, m^2
B_m	mass transfer driving force
c_p	specific heat, J/kg.K
D	diffusion coefficient, m^2/s
d	diameter, m
f	friction factor
G	mass flux in wind tunnel, $kg/m^2.s$
g	mass transfer conductance, $kg/m^2.s$
h	heat transfer coefficient, $J/m^2.s$
h_m	mass transfer coefficient, $kg/m^2.s$
J	Colburn J factor
k	thermal conductivity, $W/m\ ^\circ C$
L	length of the tube bundle, m
l	length of one tube, m
\dot{m}	mass flux through the tube walls, $kg/m^2.s$
m_{evap}	evaporated water, $kg/m^2.s$
n_{rows}	number of rows in the tube bank
n_{tubes}	number of tubes per row
Nu	Nusselt number ($h d / k$)
P	pressure, kPa
Pr	Prandtl number ($\mu c_p / k$)
\dot{Q}	transferred energy, J/s
\dot{q}	heat flux, $J/m^2.s$
R^2	correlation coefficient
Re	Reynolds number ($\rho U_s d / \mu$)
St_h	heat transfer Stanton number ($h / G c_p$)
St_m	mass transfer Stanton number (h_m / G)
Sc	Schmidt number (ν / D)
Sh	Sherwood number ($h_m d / \rho D$)
T	temperature, K or $^\circ C$
U	velocity in the direction normal to the tube bank, m/s
\bar{u}	mean velocity in the x-direction, m/s
$\overline{u'v'}$	the turbulent shear stress in a two dimensional boundary Layer, m^2/s^2
V	volumetric flow rate, m^3/s

\bar{X}	body forces acting on a fluid in the x-direction per unit Volume, N/m^3
x	mass concentration
x	pitch of a tube bank
y	coordinate normal to the surface

Abbreviations:

ACE	Alabama Cryogenic Engineering
DNS	Direct numerical simulations
LES	The large-eddy-simulation

Greek symbols:

β	blowing factor
μ	dynamic viscosity, kg/m.s
ν	kinematic viscosity, m^2/s
\bar{v}	mean velocity in the y-direction, m/s
P	perimeter, m
ρ	density, kg/m^3
ϕ	correction function to account for outgassing

Superscripts:

$^{\circ}$	value of the corresponding variable for the non-blowing case
$''$	per unit surface
\cdot	per unit time

Subscripts:

a	air
atm	atmospheric
c	in minimum free flow area
cl	center line
corr.	Corrected
f	friction
h	heat transfer
l	longitudinal
m	mass transfer
max	maximum

min	minimum
pred.	predicted
rota.	rotameter
s	at surface
s	superficial
T	transferred substance state
t	transversal
uncorr.	uncorrected
o	at surface
∞	in the free stream

List of Tables

Table	Title	Page
Table 4.1	Characteristics of the Tube Bank	51
Table 5.1	Friction Factor Results for the Non-Blowing case	67
Table 5.2a	Friction Factor Measurements with $\beta_f=0.0042$	73
Table 5.2b	Friction Factor Measurements with $\beta_f =0.0031$	74
Table 5.2c	Friction Factor Measurements with $\beta_f=0.0015$	74
Table 5.3a	Friction Factor Measurements at Re=13446	75
Table 5.3b	Friction Factor Measurements at Re=10151	76
Table 5.3c	Friction Factor Measurements at Re=5900	76
Table 5.4	Mass Transfer Results	88

List of Figures

Figures	Title	Page
Fig. 2.1	Flow across Cylinder	8
Fig. 2.2	Tube Bank Arrangements	8
Fig. 2.3	Stagnation Point of the Cylinder	10
Fig. 2.4	Boundary Layer Separation on a Cylinder in Cross Flow	10
Fig. 3.1	Geometry of a Tube Bank	27
Fig. 4.1	Test Rig	45
Fig. 4.2	Tube Bank Arrangement	46
Fig. 4.3	Rig Photograph	46
Fig. 4.4	Correlation of the Total Flow Rate as a Function of Center Line Pressure	56
Fig. 4.5	Calibration of Air Rotameter	57
Fig. 4.6	Calibration of Water Rotameter at Different Temperatures	58
Fig. 4.7	Calibration of Thermometer(1)	59
Fig. 4.8	Calibration of Thermometer(2)	59
Fig. 4.9	Calibration of Thermometer(3)	59
Fig. 4.10	Calibration of the Thermocouples	60
Fig. 5.1	Pressure Drop in the Non-Blowing Tube Bank	70
Fig. 5.2	Friction Factor for the Non-Blowing Tube Bank	70
Fig. 5.3	Comparison of the Measured Friction Factor with the Literature for the Non-Blowing Case	71
Fig. 5.4	Expected Errors on the Predicted and Experimental Friction Factors in the Non-Blowing Tube Bank	71
Fig. 5.5	Expected Absolute Errors on the Friction Factors in the Non-Blowing Tube Bank	72
Fig. 5.6	Effect of Re on the Pressure Drop	78
Fig. 5.7	Friction Factors in the Blowing Tube Bank as a Function of Re for Constant β_f	78
Fig. 5.8	Comparison of the Data with Debusschere-Ragland Work with Different Blowing Factors	79
Fig. 5.9	f/f^o for Different Values of Blowing Factor	79
Fig. 5.10	Pressure Drop Variation with the Blowing Factors	81
Fig. 5.11	Friction Factors in the Blowing Tube Bank as a Function of β_f	82
Fig. 5.12	Friction Factors in the Blowing Tube Bank as a Function of β_f^*	82

List of Figures (Continued)

Fig. 5.13	f/f^o as a Function of β_f	83
Fig. 5.14	f/f^o as a Function of β_f^*	83
Fig. 5.15	Evaporation Flux as a Function of Surface Temperature for Different Re	92
Fig. 5.16	Evaporation Flux as a Function of B_m for Different Re	92
Fig. 5.17	Mass Transfer Coefficient as a Function of β_m for Different Re	93
Fig. 5.18	Mass Transfer Coefficient as a Function of Surface Temperature	93
Fig. 5.19	Evaporation Flux as a Function of h_m for Different Re	94
Fig. 5.20	$St_m Sc^{2/3}$ as a Function of β_m for Different Re	100
Fig. 5.21	Comparison of the Correction Factor of Model 1 to the Data Points	101
Fig. 5.22	St_m^o as a Function of Re of Model 1	101
Fig. 5.23	Comparison of the Correction Factor of Model 2 to the Data Points	102
Fig. 5.24	$St_m Sc^{2/3}$ as a Function of Re of Model 2	102
Fig. 5.25	$St_m Sc^{2/3}$ as a Function of β_m for Different Re	104
Fig. 5.26	Comparison of the Correction Factor to the Data Points	104
Fig. 5.27	Comparison of the Correction Factor to the Debusschere-Ragland Data Points for Model 1	105
Fig. 5.28	Comparison of the Correction Factor to the Debusschere-Ragland Data Points for Model 2	105
Fig. 5.29	The Residual as a Function of the Blowing Factor	106
Fig. 5.30	The Residual as a Function of Re	107

CHAPTER ONE

Introduction

Predictions of heat transfer, mass transfer, and flow characteristics around cylinders in tube bundles are important in relation to various engineering aspects. A large number of studies have been carried out concerning the features of heat transfer and hydrodynamic phenomena of tube bundles. The generalization of large amount of experimental data, through similarity studies, and the constant improvement of the existing experimental techniques, allowed a better comprehension of thermal and hydrodynamic phenomena in the tube banks, therefore there is an extensive literature on transport coefficient for impermeable walls. Little quantitative information is available on porous surfaces (especially for the cylinder walls) and how the blowing or suction affects on the transport coefficients for these geometries.

The term “*transpiration*” is used collectively to refer to injection or blowing through porous surfaces. Wall-bounded turbulent flows with surface transpiration have been of great interest since the early 1950s, when blowing was first investigated as means of cooling aerodynamic surfaces under high-velocity flight conditions. Film-cooling techniques commonly used in cooling gas-turbine blades resemble transpired boundary layers. The transpired fluid absorbs thermal energy from the porous surface and reduces heat transfer rates substantially. Mass transfer and diffusion problems involving evaporation or sublimation (or condensation) from the porous wall necessitate

modeling of flow with transpiration. The effect of transpiration on the flow development in a boundary layer is also found to be significant: When fluid is injected, the boundary layer becomes thicker, the skin friction decreases, and turbulent fluctuations are enhanced. Direct applications of flow with transpiration in filtration and diffuse separation of gaseous isotopes. Combustion-induced flow fields in solid-propellant rocket motors can be thought of as mass injection from the burning surface. The wide range of engineering applications necessitates in-depth analysis of boundary layers under the influence of surface transpiration.

The whole tree or chunk wood combustor is one of a practical example in which the mass transfer rates are high enough such that the transport coefficients for impermeable wall do not hold. In such a whole tree combustor, a fuel bed of tree segments resembles a bank of tubes [1, 2].

Wood combustion is a complex process, in which the external gas phase reactions, the surface char reactions, and the internal pyrolysis reactions at the surface of the yet unaffected wood are coupled together. The pyrolysis products and moisture flow outward through the char layer driven by the transient heat transfer from the surface temperature, these gases move through the char layer to the outside creating a heavily outgassing surface. At the surface of the char, oxygen diffusing inward from the external flow and carbon dioxide and water vapor from both the internal pyrolysis reaction and diffusion from the free stream react with the char. This causes the reaction rates in the bed to be mainly limited by heat and mass transfer to and from the logs, rather than by reaction kinetics. It is obvious that an accurate estimation of heat and mass transfer coefficients is needed to predict the combustion rate

in this deep bed combustor, therefore, the influence of outgassing on transport coefficients must be considered.

Determination of heat and mass transfer coefficients is complicated by the irregular geometry of the system, the temperature variations in the bed and the condition of a heavily transpired boundary layer. The present study focuses on the influence of the outgassing on the transport coefficients over a tube banks. These transport coefficients are known to decrease due to blowing in the boundary layer [3], little data for this phenomenon is available. The data that is available is mostly confined to flows over flat plates or is for the case of small blowing rates, which do not affect the transport coefficients. Therefore, a test rig was built to examine the problem experimentally. To reduce the complexity of the problem, the flow normal to a tightly packed tube bank containing regular inert cylinders was studied. The cylinders installed were porous tubes which enabled an outgassing boundary layer to be created by blowing air through the walls. The center tube was used to evaporate water from its surface. The friction factors and the mass transfer coefficients for this tube were measured as a function of the flow rate in the tube bank and the amount of blowing in the boundary layer.

CHAPTER TWO

Literature Survey

2.1 Introduction

Much progress on the heat, mass transfer and flow characteristics for different geometries has been achieved in the past decade and the study of flow with transpiration effect has attracted more attention recently. However, thorough the interactions and mixing mechanism between the transpired fluid and the main flow still need further investigation, especially for those containing significant rate of heat and mass transfer and complicated geometry

2.2 Basic Duct Hydraulics

Duct air moves according to three fundamental laws of physics: conservation of mass, conservation of energy, and conservation of momentum.

Conservation of mass simply states that an air mass is neither created nor destroyed. From this principle it follows that the amount of air mass coming into a junction in a ductwork system is equal to the amount of air mass leaving the junction, or the sum of air masses at each junction is equal to zero.

Conservation of mass is often referred to as "conservation of flow", because of the change of flow that can result from change in pressure and temperature (air density).

Air flow through a duct system creates three types of pressures: static, dynamic (velocity), and total. Each of these pressures can be measured. Air conveyed by a duct system imposes both static and dynamic (velocity) pressures on the duct's structure. The static pressure is responsible for much of the force on the duct walls. However, dynamic (velocity) pressure introduces a rapidly pulsating load.

Static pressure is a measure of the potential energy of a unit of air in the particular cross section of a duct. Air pressure on the duct wall is considered static. Imagine a fan blowing into a completely closed duct; it will create only static pressure because there is no air flow through the duct.

Dynamic (velocity) pressure is the kinetic energy of a unit of air flow in an air stream. Dynamic pressure is a function of both air velocity and density

The static and dynamic pressures are mutually convertible; the magnitude of each is dependent on the local duct cross section, which determines the flow velocity.

Total pressure, the sum of static and dynamic pressures in a particular duct cross section, is:

$$\text{Total pressure} = (\text{Static pressure}) + (\text{Dynamic pressure})$$

Pressure loss is the loss of total pressure in a duct or fitting. There are three important observations that describe the benefits of using total pressure for duct calculation and testing rather than using only static pressure [4]:

- Only total pressure in ductwork always drops in the direction of flow. Static or dynamic pressures alone do not follow this rule.
- The measurement of the energy level in an air stream is uniquely represented by total pressure only. The pressure losses in a duct are represented by the combined potential and kinetic energy transformation, i.e., the loss of total pressure.
- The fan energy increases both static and dynamic pressure. Fan ratings based only on static pressure are incorrect.

The **law of energy conservation** states that energy cannot disappear; it is only converted from one form to another. This is the basis of one of the main expressions of aerodynamics, the *Bernoulli equation*. Bernoulli's equation in its simple form shows that, for an elemental flow stream, the difference in total pressures between any two points in a duct is equal to the pressure loss between these points, or:

$$(\text{Pressure loss})_{1-2} = (\text{Total pressure})_1 - (\text{Total pressure})_2$$

Conservation of momentum is based on *Newton's law* that a body will maintain its state of rest or uniform motion unless compelled by another force to change that state.

The total drag on any body consists of skin friction drag and form drag. The skin friction drag is a result of the viscous forces acting on the body while the form drag is due to the unbalanced pressure forces on the body. The sum of the two is called total or profile drag [5].

For turbulent flow in a duct of non-circular cross-section, the *hydraulic mean diameter*, D_H may be used in place of the pipe diameter d , and the formulae for circular pipes can then be applied without introducing a large error. This method of approach is entirely empirical.

The *hydraulic mean diameter* D_H is defined as four times the *hydraulic mean radius* r_H . Hydraulic mean radius is defined as the flow cross-sectional area divided by the wetted perimeter as given below:

$$D_H = \frac{4 A}{P} \quad (2.1)$$

where A is the cross-sectional area, and P is the perimeter, or the total length of the surface which is in contact with the fluid in one cross section.

2.3 Flow across Tube Banks

While the engineer may frequently be interested in transport phenomena and flow characteristics of flow systems inside tubes or over flat plates, equal importance must be placed on the flow which may be achieved by a cylinder in cross flow, as shown in Fig. 2.1. The tube rows of a bank are either staggered (triangular) or aligned (square) in the direction of the fluid

velocity as shown in Fig. 2.2. The configuration is characterized by the tube diameter (d), and by the transverse pitch and longitudinal pitch measured between tube centers. Flow conditions within the bank are dominated by boundary layer separation effects and by wake interactions.

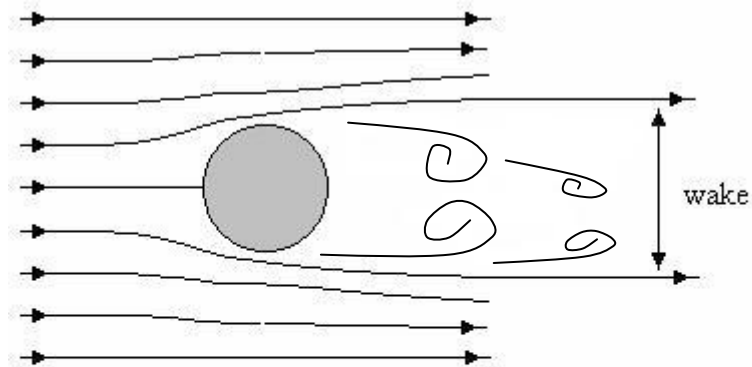


Fig. 2.1: Flow across Cylinder.

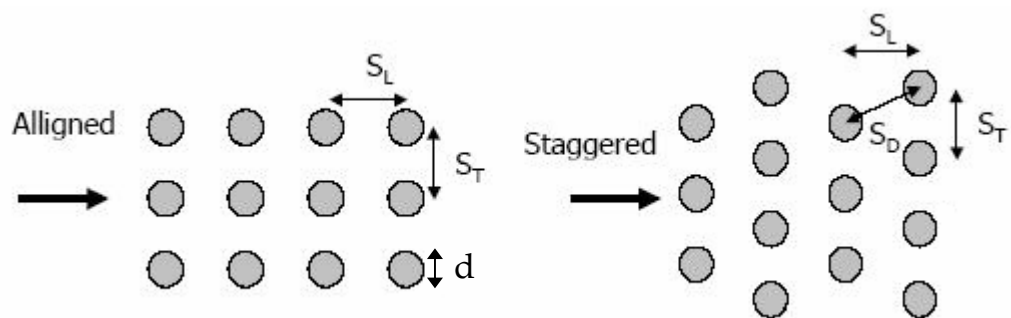


Fig. 2.2: Tube Bank Arrangements.

Consistent with boundary layer theory, the pressure through the boundary layer is essentially constant at any x -position on the body. In the case of the cylinder, one might measure x -distance from the front stagnation point of the cylinder (Fig. 2.3). Thus the pressure in the boundary layer should follow that of the free stream for potential flow around a cylinder provided this behavior would not contradict some basic principle which must apply in the boundary layer. As the flow progresses along the front side of the cylinder, the pressure would decrease and then increase along the back side of the cylinder, resulting in an increase in free stream velocity on the front side of the cylinder and a decrease on the back side. The transverse velocity (the velocity parallel to the surface) would decrease from a value of U_∞ at the outer edge of the boundary layer to zero at the surface. As the flow proceeds to the back side of the cylinder, the pressure increase causes a reduction in the velocity in the free stream and through out the boundary layer. The reverse flow may begin in the boundary layers near the surface, i.e., the momentum of the fluid layers near the surface is not sufficiently high to overcome the increase in pressure. When the velocity gradient at the surface becomes zero, the flow is said to have reached a separation point [6, 7, 8]:

$$\text{Separation point at } \left. \frac{\partial u}{\partial y} \right|_{y=0} = 0$$

As the flow proceeds past the separation point, reverse flow phenomena may occur. The phenomenon of boundary layer separation is indicated in Fig.2.4. Eventually, the separated flow region on the back side of the cylinder becomes turbulent and random in motion.

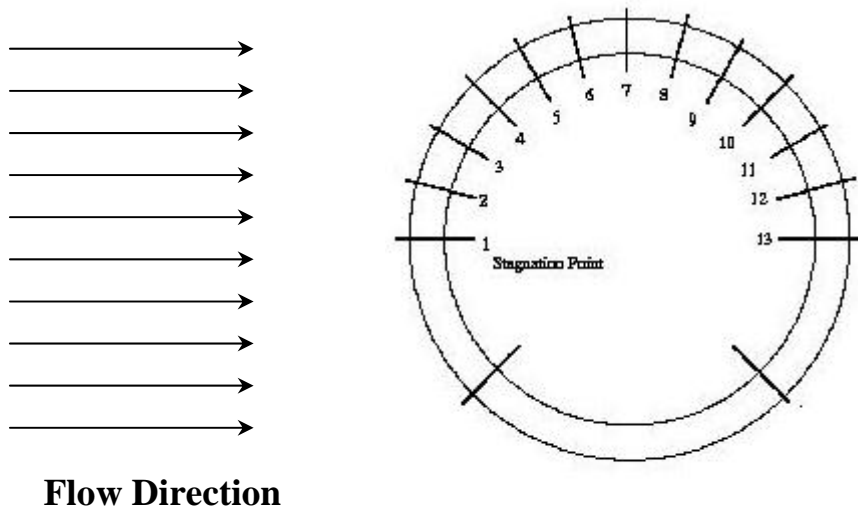


Fig. 2.3: Stagnation Point of the Cylinder[6].

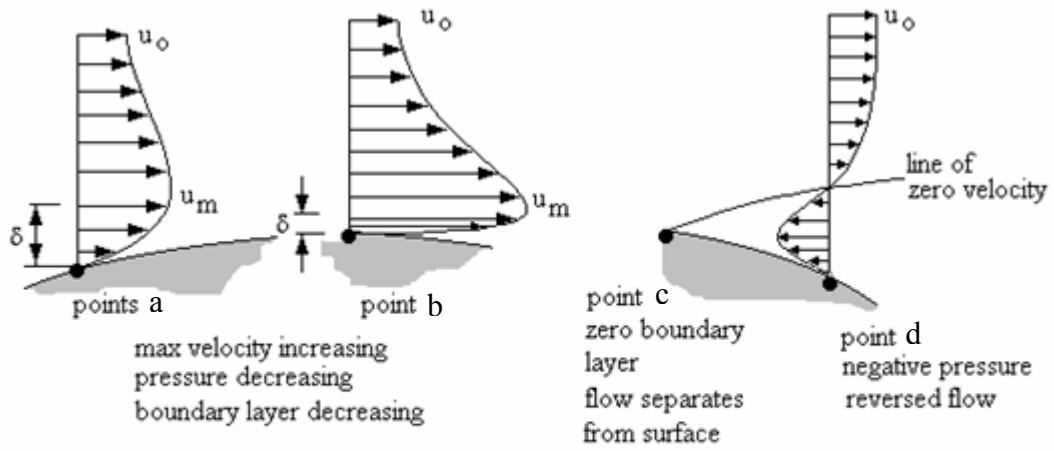


Fig. 2.4: Boundary Layer Separation on a Cylinder in Cross Flow[7].

In other words, two important effects affect the drag (Fig 2.4):

Outside the boundary layer, the velocity increases up to point b so the pressure acting on the surface goes down. The boundary layer thickness δ gets smaller until point c it is reduced to zero and the flow separates from the surface. At point d , the pressure is negative. This change in pressure is responsible for the form drag.

Inside the boundary layer, the velocity is reduced from maximum velocity to zero and skin friction drag results [9].

2.4 Effect of Transpiration on Transport Coefficients

2.4.1 Momentum Transfer

For the case of the impermeable wall, the normal component of velocity v_o for the turbulent boundary layers is zero. Nonzero values of v_o can occur if the wall is porous and fluid is "*blown*" or injected in the boundary layer, or is withdrawn or "*sucked*". Evaporation or condensation or mass transfer, in general, lead to nonzero values of v_o . This adds a strong stream wise convective acceleration to the near wall boundary layer. The term transpiration or the transpired boundary layer is used as a general description interchangeable with blowing, suction, mass transfer at the surface.

For laminar boundary layers it was found that similarity solutions exist for nonzero values of v_o provided that a blowing parameter, essentially β_f is

maintained constant, the constant β_f results in an equilibrium turbulent boundary layer.

Transpiration alters the structure of the turbulent boundary layer rather considerably, affecting the sheer-stress distribution, and also strongly affecting the sub layer thickness. The transpired boundary layer can be calculated quite adequately by finite-difference techniques using the mixing-length model [3, 10].

Kays and Crawford [3] used an alternative method by starting with the momentum partial differential equation for the flow over a flat plate in the x_i -direction for the two dimensional "steady" turbulent boundary layers:

$$\rho \bar{u} \frac{\partial \bar{u}}{\partial x} + \rho \bar{v} \frac{\partial \bar{u}}{\partial y} = -\frac{d\bar{P}}{dx} + \frac{\partial}{\partial y} (\tau - \rho \overline{u'v'}) + \bar{X} \quad (2.2)$$

For the constant property with negligible body forces the boundary layer momentum equation is recast using *Newton's law of viscosity* to become:

$$\bar{u} \frac{\partial \bar{u}}{\partial x} + \bar{v} \frac{\partial \bar{u}}{\partial y} = -\frac{1}{\rho} \frac{d\bar{P}}{dx} + \frac{\partial}{\partial y} \left(\nu \frac{\partial \bar{u}}{\partial y} - \overline{u'v'} \right) \quad (2.3)$$

where the *Newton's law of viscosity* is:

$$\tau = -\mu \frac{\partial u}{\partial y} \quad (2.4)$$

And,

$$\overline{u'v'} = -\varepsilon_M \frac{\partial \bar{u}}{\partial y} \quad (2.5)$$

Kays and Crawford integrated eq.2.3 across the turbulent boundary layer and assuming the eddy viscosity is not affected by transpiration and they found a reasonable approximate procedure by multiplying the friction coefficient of the non-outgassing case with a correlation equation $\varphi(\beta_f)$ to account the effect of the transpiration on the friction of the outgassing case as given below:

$$\frac{f}{f^o} = \varphi(\beta_f) \quad (2.6)$$

$$f^o = 0.0287 Re_x^{-0.2} \quad (2.7)$$

Substitute eq. 2.7 into eq.2.6 to get:

$$f = 0.0287 \varphi(\beta_f) Re_x^{-0.2} \quad (2.8)$$

The superscript o indicates for the non-blowing state, and β_f is the friction blowing factor.

The influence of outgassing on the friction factor for flow through a staggered row tube bank was measured by **Debusschere and Ragland** [11]

and the constant property approximation does not hold. They got the following correlation for the friction factor in non-blowing tube bank:

$$f^o = 39.0 Re^{-0.25} \quad \text{for } 3000 < Re < 16,000 \quad (2.9)$$

They found the overall friction factor (eq. 2.9) increases when compressed air is blown through the pores of all tubes,.

2.4.2 Heat Transfer

The effect of transpiration on the thermal turbulent boundary layer is very similar to the effect on the momentum boundary layer described in the previous sections, the transpired flow described in that section can be developed in precisely the same manner for the Stanton number as for the friction coefficient and the heat transfer blowing factor β_h is introduced rather than the friction blowing factor as given below [3, 11]:.

$$\frac{St_h}{St_h^o} = \varphi(\beta_h) \quad (2.10)$$

Kays and Crawford gives the following expression for the flow over a flat plate in the no-blowing state (with the assumptions given previously):

$$St_h^o Pr^{0.4} = 0.0287 Re_x^{-0.2} \quad (2.11)$$

For $0.5 < Pr < 1.0$ and $5 \times 10^5 < Re_x < 5 \times 10^6$.

Substitute eq. 2.11 into eq.2.10 to get:

$$St Pr^{0.4} = 0.0287 \varphi(\beta_h) Re_x^{-0.2} \quad (2.12)$$

According to eq.2.10, **Debusschere and Ragland** got the following correlation for heat transfer for the flow across tube bank:

$$St_h Pr^{2/3} = 1.54 \varphi(\beta_h) Re_d^{-0.5} \quad (2.13)$$

And they found that the heat transfer coefficient reduce as blowing increase.

2.4.3 Mass Transfer

A large rate of mass transfer to or from the surface leads to the transpired turbulent boundary layer problem.

Kays and Crawford said if all fluid properties are assumed constant, it makes no difference if the fluid crossing the surface is chemically the same or different from the free –stream fluid. For the present purposes it was assumed complete similarity, and this allow to make use of the turbulent boundary layer heat-transfer solutions with only a change of names of the variables and parameters. Thus eqs. 2.10 and 2.12 should be applicable. The blowing factor β_h is, of course, the same as the mass transfer driving force when g/G_∞ is substituted for St_m [3]. Thus

$$\frac{St_m}{St_m^o} = \frac{g}{g^o} = \varphi(\beta_m) \quad (2.14)$$

where β_m is the mass transfer blowing factor, g is the mass transfer conductance in kg/s.m^2 and it is equal to the mass velocity of the main stream multiplied by the Stanton number ($g = G_\infty St_m$), and λ is a diffusion coefficient, and μ is the dynamic viscosity of the fluid.

If the free-stream velocity is constant and the mass transfer rate is small (small B_m), then $g \rightarrow g^o$, and eq. 2.12 should be directly applicable for a gas mixture:

$$\frac{g^o}{G_\infty} \left(\frac{\mu}{\lambda} \right)^{0.4} = 0.0287 Re_x^{-0.2} \quad (2.15)$$

Substitute eq. 2.15 into eq.2.14 to get:

$$St_m \left(\frac{\mu}{\lambda} \right)^{0.4} = 0.0287 \varphi(\beta_m) Re_x^{-0.2} \quad (2.16)$$

Considering eq.2.14 applicable for mass transfer **Debusschere and Ragland** found the following correlation for mass transfer for the flow across tube bank:

$$St_m Sc^{2/3} = 0.76 \varphi(\beta_m) Re_d^{-0.5} \quad (2.17)$$

And they found that the mass transfer coefficient was reduced as blowing was increased.

2.5 Review of Previous Works

Transpiration flow is very important in many engineering applications. It is an unusual form of wall turbulence because the turbulence is created by the injection of fluid normal to the wall, as opposed to friction associated with flow parallel to the wall.

An extensive experimental work on flows with surface transpiration was carried out at the *Massachusetts Institute of Technology* by **Mickley *et al.***[12], between 1967 and 1975 many experiments were carried out at Stanford to study the characteristics of transpiration on boundary layers. **Simpson *et al.*, in 1969** [13], **Julien *et al.*, in 1972**[14], and many others made extensive measurements of mean velocity profiles, skin friction coefficients, and Reynolds stresses in transpired boundary layers over a flat plate. A comprehensive review of experiments and other studies on transpiration can be obtained by **Kays and Crawford, in 1993** [3], they studied suction and blowing in a boundary layer for the flow parallel to a flat plate. Overall, it appears that the influence of blowing or suction on the transport processes can be accounted for by multiplying the respective transport coefficients with a correction factor. This correction factor depends on the amount of outgassing, represented by a blowing factor

Spalding and Evans, in 1961 [15] provide self-similar solutions for mass transfer through laminar boundary layers. Even though the effect of finite outgassing rates is taken into account, the solutions in [15] only apply to very specific configurations and involve the assumption of uniform properties. **Lessner and Newman, in 1984** [16] studied the hydrodynamics

and mass transfer equations for porous wall flow channel over a large range of Reynolds number and Schmidt number and analyzed the low Re, high Sc case and the intermediate range treated by numerical methods. **Hirata *et al.*, in 1990** [17] investigated the development of velocity and concentration fields for turbulent air flow in a porous tube with carbon dioxide gas injection. From the variations of shear stress and diffusion flux in the flow direction in addition to those of velocity and concentration, it was found that the flow was fully affected up to the tube center in a region more than fifteen times the diameter downstream from the entrance. This study presents that the turbulent Schmidt number is not affected by the flux and the expressions for mixing length and turbulent Schmidt number obtained in this study may be applied to the estimation of characteristics of flow and mass transfer in a membrane module. **Mustafa, in 1991**[18] investigated the theoretical, computational and experimental treatment of the flow through porous tube. Results indicated that due to the physical variation of the actual wall structural properties overall effect using a permeability parameter offers an integral influence of all the parameters on the flow through the porous tube. Model and test results showed that an increase in down stream pressure was expected to account for the transfer of axial momentum of the permeating fluid through the porous wall into axial pressure increase. **Debusschere and Ragland, in 1998** [11] investigated the influence of the blowing on the transport coefficients for flow through a staggered row tube bank was measured and they concluded that because of outgassing, heat and mass transfer coefficients reduced and new blowing factors and correction functions that were obtained quantify the effect of outgassing on the transport coefficients.

Danny, in 2002 [19] provided guidelines for the selection of porous plate for, the characteristics of micro-hole porous skins for the turbulent skin

friction reduction technology (micro-blowing technique). The hole angle, pattern, diameter and aspect ratio were the parameters considered for his study.

Inger and Babinsky, in 2000 [20] have recently proposed a new theory to predict the mass flux versus pressure difference relationship, based on a solution of the continuity equation, the momentum equation and the ideal gas equation, for each hole independently (i.e. a large distance is assumed to exist between holes). **Inger and Babinsky** assumed that the average value of skin friction over the entry length is some constant greater than its fully-developed value and they gave an expression for the average value of skin friction over the entire length of the hole. A method including a simple but accurate analytical description of the 'entry effects' in a broader analytical description of the compressible flow through a porous plate has been developed and tested by **Galluzzo and Babinsky, in 2002** [21, 22]. The results apply to any size of circular hole (not just the small holes in porous plates). It may be of interest to researchers (for example in the ink-jet industry) that the analytical results from this work apply for any fluid, not just perfect gases. Experimental results obtained show that very close agreement with the resulting expression for transpiration mass flux. **Galluzzo and Babinsky** proposed the factors that may explain this "blocking effect", the main factor was the secondary flow inside the entrance of holes. This secondary flow will appear as two adjacent vortices, whose axes are parallel but whose orientations are opposite to each other. These vortices will cause an increase in the rate of dissipation of energy in the flow, and hence will increase the pressure loss across the porous plate. Efforts are currently in progress to quantify this.

The effect of a tangential stream on the action of porous surfaces was first observed experimentally by **Bohning and Doerffer, in 2002** [23] in Germany. They reported that the transpiration flow is encountering a blocking effect when a tangential stream flows along the porous plate. This means that for the same pressure drop across the plate the mass flow rate is smaller than in the case without the stream. The effect is only present for suction. In the case of blowing no effect of a tangential stream has been noticed.

The large-eddy-simulation (LES) technique was used by **Piomelli *et al.*, in 1991**[24] to study the effects of transpiration on turbulent channel flows. Considerable improvement in predicting the wall-layer and turbulence characteristics was achieved. **Sumitani and Kasagi, in 1995** [25] performed direct numerical simulations (DNS) of flow through porous channels with blowing from one side and suction through the opposite wall at low transpiration rates. Results indicated that mass injection decreases the friction coefficient, but tends to stimulate the near-wall turbulence activity so that the Reynolds stresses and turbulent heat fluxes are increased, whereas suction has an inverse influence.

Flow evolution in a porous chamber with surface mass injection resembles the flow field ensuing from the burning of solid propellant in a rocket motor. An analytical description of the in viscid, rotational laminar flow field in such a configuration was first obtained by **Taylor, in 1956** [26] and later validated by **Culick, in 1966** [27]. **Beddini, in 1986** [28] investigated the development of turbulent flow fields through porous-walled ducts at large injection Reynolds numbers, indicating three different flow regimes. The velocity field develops in accordance with laminar flow theory near the head end and undergoes transition in the midsection of the chamber.

Transition of the mean axial velocity profiles occurs farther downstream in the fully developed turbulent flow field. These results were further validated by **Traineau *et al.*, in 1986** [29] through their experimental study on a nozzleless rocket motor at high injection Reynolds number and Mach number. The effect of compressibility on transition of the mean velocity profiles from their incompressible counter parts was elucidated in detail. A theoretical analysis of in viscid but rotational and compressible flow field in a porous duct with varying injection rates and favorable pressure gradients was carried out by **Balakrishnan *et al.*, in 1992**[30]. An experimental study of the flow field a porous chamber was carried out by **Dunlap *et al.*, in 1992** [31] at low injection Mach numbers, with turbulence properties measured at various locations.

Several numerical simulations have been performed to study the flow field within a rocket combustion chamber. **Sabnis *et al.*, in 1989**[32] and **Tseng, in 1992**[33] and obtained good comparison of the mean flow field with experimental data, but over predicted the turbulence intensity levels within the chamber. **Nicoud *et al.*, in 1995**[34] performed DNS at high injection rates in an attempt to reproduce flow conditions representative of a solid rocket motor to study the effect of high blowing rate on the wall layer.

In an effort to characterize unsteady motions in rocket motors, **Apte and Yang, in 2001** [35] performed LES of internal flow development in a three-dimensional rectangular rocket motor to obtain better predictions of turbulence properties and explored the physical aspects of the unsteady flow evolution in detail. A comprehensive numerical study of the unsteady flow evolution in a porous chamber with surface mass injection simulating a nozzleless rocket motor has been investigated numerically by means of an

LES technique and the effect of turbulence and fluid compressibility on the mean flow structure was examined in depth by **Apte** and **Yang**. They examined in depth the effect of turbulence and fluid compressibility on the mean flow structure and they found the mass injection is primarily decreasing the wall shear stresses. The flow field is governed by the balance between pressure gradient and inertia forces, as opposed to the viscous stresses and pressure gradient as in channel flows without injection. The flow evolution is characterized primarily by three nondimensional numbers: injection Reynolds number, centerline Reynolds number, and momentum flux coefficient.

Advancements in rocket propulsion technologies are needed to increase performance (and therefore payload capabilities) while reducing cost and complexity. Improved performance can theoretically be obtained by operating the rocket at previously unattainable conditions such as higher-pressure levels. A consequence of increasing chamber pressure is an increase in wall heat flux. This introduces the need for active cooling mechanisms such as transpiration cooling. In the past, transpiration cooling was considered, but the cost of producing the porous material was too expensive. **Alabama Cryogenic Engineering, Inc. (ACE), in 2005** [36] has developed a relatively inexpensive drawing process to fabricate metal plates with very small, uniformly distributed holes. These plates could be used for transpiration cooled combustion chambers and nozzle throats.

A one-dimensional thermal/fluid computational model was developed to predict the temperature distribution through the thickness of the wall and in the coolant. The model accounts for variable thermodynamic properties and the effect of surface blowing on the hot gas convective heat transfer. The final report describing the analysis has been submitted to ACE.

Collier, Jr. and Schetz, in 1984 [37] indicated that the turbulence intensity and Reynolds stress in the turbulence boundary layer increased with the increasing injection. Researches on transpiration cooling were conducted after 1990s. **Eckert and Cho, in 1994** [38] focused on Stanton number and the transpiration rate (the ratio of injected velocity and inlet velocity), and found that they were important indexes. The film cooling and transpiration cooling were compared through their heat performance. The flow field and structure would be changed when injected fluid from the bottom wall is added. **Cheng et al., 1994** [39] indicated that the heat transfer was increased but the pressure loss and friction coefficient were decreased with the increasing injection through the porous sheet. **Robet et al., in 1997** [40] added the coolant under the porous sheet and the flow with hot temperature up the sheet. The influence of wall injection was discussed in relation to factors of turbulence intensity, boundary layer, and friction coefficient of the wall. The analysis of the transient process further sheds light on flow structures and heat transfer.

Yang et al., in 2003 [41] experimentally studied the transient cooling processes with cold air injection from the bottom wall. Two mechanisms, porous-wall cooling and film-cooling were proposed to interpret the transition of cooling pattern due to the increase rate of wall injection

Study of convective heat transfer around a film cooled turbine blade with leading edge film cooling was conducted by some workers. Recent work on showerhead cooling was concentrated on models with rather large spacing of rows. **Mehendale and Han, in 1990** [42] investigated the influence of high free stream turbulence. The results indicated that the film effectiveness

decreased with increasing blowing ratio, with an inverse effect for the heat transfer coefficient. **Karni and Goldstein, in 1990** [43] varied the injection location relative to the stagnation line to investigate the cooling behavior of one single row at different blowing rate and it was reported that the mass transfer distribution was extremely sensitive to small changes in the injection hole location relative to the stagnation point. **Camci and Arts, in 1990** [44] used a three row configuration with holes at the stagnation point and they concluded that the leading edge film cooling was quite effective for low blowing rates and the free stream turbulence varied at constant film cooling parameters. **Hoffs *et al.*, in 1997** [45] investigated the effectiveness and heat transfer on a cylinder model with showerhead cooling. Higher effectiveness – but also increased heat transfer was in general observed for the four row configuration, with a 60% higher mass flow. The showerhead cooled cylinder was conducted for a three and four row configuration at zero and off-design incidences.

Ekkad *et al.*, in 1997 [46] investigated in details the heat transfer coefficients over a flat surface with one row of injection holes inclined stream wise at 35 deg for three blowing ratios. Three compound angles with air and CO as coolants were tested at an elevated free-stream turbulence condition. Heat transfer coefficients increase with increasing blowing ratio for a constant density ratio, but decrease with increasing density ratio for a constant blowing ratio. Heat transfer coefficients increase for both coolants over the test surface as the compound angle increases from 0 to 90 deg.

Riabov, in 2004 [47] studied the interactions of a diffusing outgas flow from a sphere nose opposing a hypersonic free stream is studied numerically

by the direct simulation Monte-Carlo technique. It has been found that strong influences of the blowing factor and on heat distributions along the spherical surface have been found. At large blowing factors, the injected gas significantly reduces heat flux in wide area near the spherical nose. This effect is more pronounced for light gas (helium) injection in the near-continuum flow.

Ogawa, in 1987 [48] studied the mass transfer in a mixed gas flow crossing a porous graphite cylinder placed in a high temperature environment in the presence of chemical reactions and in pore diffusion of oxygen. The main conclusions of this study is in the boundary layer mass transfer controlled regime the mean Sherwood numbers obtained in the experiment agreed fairly well with the obtained empirical relation of the mass transfer on the basis of the analogy between heat transfer and mass transfer and the corrosion rates of the intermediate regime between in-pore diffusion controlled regime and boundary layer mass transfer controlled regime were varied to be estimated from the empirical relations of the corrosion rate and the mean mass transfer coefficient.

CHAPTER THREE

Transport Phenomena in Tube Banks

3.1 Introduction

This chapter explains the theoretical background behind all of the measurements done. It will also clarify the definitions, correlations, effect of the blowing, and notations used throughout the whole text. The first part deals with momentum considerations while the two following sections handle heat and mass transfer. Finally, the frequently used analogy between heat, mass, and momentum transfer is explained in details.

3.2 Fluid Flow in a Tube Bank

3.2.1 Geometrical Description of a Tube Bank and General Definitions

The geometry of a tube bank is usually described as a function of the size (diameter d and length l) of the tubes used, and a series of non-dimensional parameters. Some of the definitions are illustrated in Fig. 3.1.

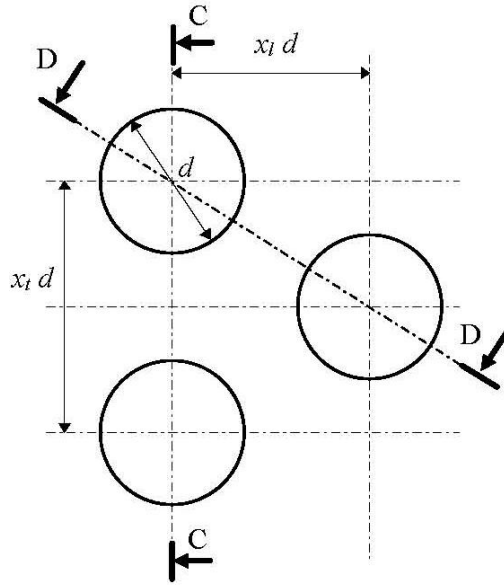


Fig. 3.1: Geometry of a Staggered Tube Bank.

The longitudinal pitch x_l is the distance between two rows of tubes in the flow direction divided by the tube diameter. The transversal pitch x_t gives the non-dimensional distance between two tubes in the direction perpendicular to the main flow. The total cross section area of the tube bank (A), the minimum free flow area (A_c), and the length of the tube bank (L) can be expressed as a function of these parameters:

$$A = x_t d n_{tubes} l \quad (3.1)$$

$$A_c = (x_t - 1) d n_{tubes} l \quad (3.2)$$

$$L = x_l d n_{rows} \quad (3.3)$$

The parameter n_{tubes} gives the number of tubes in one row of the tube bank and n_{rows} gives the number of rows (in the streamwise direction). Note that for this tube bank, the minimum free flow area is located in the cross section C-C. Depending on x_t and x_l , this area can also be located in the cross section D-D.

The Reynolds number in this study is defined as:

$$Re = \frac{U_s d}{\nu} \quad (3.4)$$

where ν is the kinematic viscosity of the fluid, d is the tube diameter, and U_s is the superficial velocity in the tube bank. This U_s is calculated by dividing the volumetric flow rate in the tube bank V by the total area A which means it is the velocity that would exist in a duct without tubes, but with the same outer dimensions as the tube bank. The mass flux G is calculated using the minimum free flow area A_c :

$$G = \rho \frac{V}{A_c} = \rho U_c \quad (3.5)$$

U_c is the velocity in this minimum free flow area and ρ is the fluid density.

3.2.2 Overall Pressure Drop

A variable of major practical concern in the study of the flow normal to a tube bank is the overall pressure drop Δp since this determines how much mechanical energy is lost. The pressure drop is a function of the geometry and the Reynolds number. A pressure drop equation is given in [49] but is

simplified and modified here to be consistent with all of the other definitions and used to define the friction factor as given:

$$\Delta p = n_{rows} \frac{\rho U_s^2}{2} f \quad (3.6)$$

3.2.3 Friction Factor:

The friction factor f is set by the fluid-wall interactions in the boundary layer around the tubes. One component of f is the viscous shear stress or skin friction. In tube banks however, this accounts for only a very small fraction of the total friction. The major contribution to the pressure drop results from the boundary layer separation creating a low pressure wake behind each cylinder. This means that the static pressure around the tube perimeter is unbalanced thereby exerting a net force on the cylinder, referred to as form drag. The magnitude of this form drag is strongly dependent on the position of the separation point on the cylinder [6, 8].

Data for the friction factor for a certain geometry and roughness in a non-blowing boundary layer is sometimes presented in the form [3, 49]:

$$f^o = a Re^b \quad (3.7)$$

These correlations only hold in a certain range of Re .

3.2.4 Influence of Outgassing on the Pressure Drop

Blowing in the boundary layer can affect the pressure drop in a tube bank by changing the skin friction and (or) by changing the position of the separation point.

For the skin friction in laminar boundary layers of the wedge flow type, some similarity solutions are given in [3]. For the turbulent boundary layer on a flat plate, an analytical model is derived in [3]. It is given in this investigation for completeness and because the form of it will be used to develop correlations for mass transfer as given in the previous chapter by eq.2.6:

$$\frac{f}{f^o} = \varphi(\beta_f) \quad (2.6)$$

The basic idea is that the friction factor for the outgassing boundary layer can be obtained from the friction factor for the non-outgassing boundary layer f^o by multiplication with a function $\varphi(\beta_f)$. The parameter f^o is only dependent on the geometry and the Reynolds number. It is clear that this is an implicit model for the friction factor f .

In this study, two blowing factor β_f definitions were used to represent the amount of outgassing given in [3]:

$$\beta_f = \frac{\dot{m}}{G_\infty} \quad (3.8)$$

And the other one,

$$\beta_f^* = \frac{\dot{m}'' / G_\infty}{f} \quad (3.9)$$

where the G_∞ is the mass flux is considered in the free stream and \dot{m}'' is the mass flux through the wall.

3.3 Heat Transfer

3.3.1 Definitions

The convective heat transfer \dot{Q} from a surface A at a temperature T_s to a fluid at T_∞ is generally expressed as:

$$\dot{Q} = A h (T_s - T_\infty) \quad (3.10)$$

The parameter h is the convective heat transfer coefficient. From an energy balance on an infinitesimal control volume containing the wall, it can be derived that :

$$\frac{\dot{Q}}{A} = q = -k \left. \frac{\partial T}{\partial y} \right|_o \quad (3.11)$$

which means the heat transfer coefficient can be calculated from temperature profiles as:

$$h = \frac{-k \left. \frac{\partial T}{\partial y} \right|_o}{(T_s - T_\infty)} \quad (3.12)$$

In this equation, k represents the thermal conductivity of the fluid and q is the convective heat transfer per unit surface and per unit time. The determination of the temperature profile in a boundary layer usually requires the solution of a coupled set of partial differential equations, the equations of motion and the energy equation. This is not always feasible and therefore a lot of correlations for the heat transfer coefficient have been derived from experimental data. These correlations are frequently expressed in terms of the non-dimensional Stanton number St_h , the Nusselt number Nu and the Prandtl number Pr [50, 51] :

3.3.2 Correlations

Considerable experimental data is available for heat transfer in tube banks without blowing and these data is usually presented in the form [3, 10]:

$$St_h^o Pr^{2/3} = a Re^b \quad (3.13)$$

3.3.3 Influence of Outgassing on Heat Transfer

Outgassing will affect the heat transfer since it changes the flow pattern and consequently the temperature profile in the boundary layer. In [3] it is suggested that the phenomenon can be modeled similar to the skin friction in an outgassing boundary layer:

$$St_h Pr^{2/3} = \varphi(\beta_h) St_h^o Pr^{2/3} \quad (3.14)$$

From the above equation it is obvious that $St_h Pr^{2/3}$ is only dependent on geometry and Reynolds number and is equal to the value of $St_h Pr^{2/3}$ for the non-outgassing case. The function $\varphi(\beta_h)$, with β_h being the generic symbol for a heat transfer blowing factor, represents the change in heat transfer due to blowing.

3.4 Mass Transfer

3.4.1 Definitions

Similar to heat transfer, convective mass transfer is generally expressed using the mass transfer coefficient h_m [3, 15] :

$$\dot{m} = h_m B_m \quad (3.15)$$

$$B_m = \frac{x_\infty - x_o}{x_o - x_T} \quad (3.16)$$

where \dot{m} represent mass transfer per unit area and per unit of time and B_m is the mass transfer driving force. B_m is calculated from the mass concentrations (of the substance that gets transferred) at the free stream (x_∞), at the surface (x_o) and at the transferred-substance state (x_T). This transferred-substance state (T-state) is defined such that there are no gradients either in temperature or concentration at the T state location. For most cases, that only one substance is transfer x_T will be equal to one. A more extensive definition and

treatment of these states is given in [3]. From a mass balance, it can be derived that:

$$h_m = \frac{-\rho D \left. \frac{\partial x}{\partial y} \right|_o}{(x_o - x_\infty)} \quad (3.17)$$

where D is the binary diffusion coefficient for the transferred substance into the surrounding medium. This means h_m can be determined from the slope of the concentration profile at the surface. Since this requires, in general, the solution of the equations of motion for each substance together with the energy equation, this is not always feasible. Consequently, correlations of experimental data can be very useful. These correlations can be expressed in terms of the mass transfer Stanton number St_m , the Sherwood number Sh and the Schmidt number Sc [50, 51]:

3.4.2 Correlations

For flow normal to tube banks, few abundant experimental data is available. Some data was found for a tube bank vibrating in a fluid at rest [52], and flow normal to a tube bank [11], this data is represented in the familiar form:

$$St_m^o Sc^{2/3} = a Re^b \quad (3.18)$$

All of this data is for the case of small mass transfer rates and is very often obtained by applying the **Chilton-Colburn** analogy to heat transfer data.

3.4.3 Influence of Outgassing on Mass Transfer

When mass transfer rates are large, the concentration profile in the boundary layer will change due to the flow rate induced by the mass transport coming from the wall. It is assumed that the influence of outgassing can be accounted for by multiplying the mass transfer coefficients for the case of negligible blowing by a function $\varphi(\beta_m)$ of the mass transfer blowing factor β_m :

$$St_m Sc^{2/3} = \varphi(\beta_m) St_m^o Sc^{2/3} \quad (3.19)$$

As in the heat transfer section, $St_m Sc^{2/3}$ is obtained from the non-outgassing case and is a function of Re and geometry only. Again, the function $\varphi(\beta_m)$, with β_m being the generic symbol for a mass transfer blowing factor, represents the change in mass transfer due to blowing.

3.5 Analogies

Based on similarities in the governing differential equations, analogies between the different transport processes can be observed. When certain assumptions are met, it is possible to convert heat transfer data into mass transfer or friction data and vice versa by a simple change of variables. The concept of valid analogy among mass, heat, and momentum transport is that the basic mechanisms are essentially the same. The similarity among the transfer phenomena and accordingly, the existence of the analogies, require that the following six conditions exist within the system:

- 1) There is no energy or mass produced within the system.
- 2) There is no emission or absorption of radiant energy.
- 3) There is no viscous dissipation.
- 4) The velocity profile is not affected by the mass or heat transfer, thus there is only a low rate of mass or heat transfer.
- 5) The physical properties are constant
- 6) The spectral fluctuations of the fluctuating quantities u', T' and c' must be similar.

The **Chilton-Colburn** [53] analogy is probably the best known example. The **Chilton-Colburn** analogy has proved useful since its introduction in 1933 because it is based on empirical correlations and not on the mechanistic assumptions that are only approximations.

This analogy can be written in terms of the **Colburn** J factors for heat and mass transfer and an appropriately defined friction factor c_f . The correlation of the heat transfer data obtained by **Colburn** is:

$$St_h Pr^{2/3} = \frac{c_f}{2} = J_h \quad (3.20)$$

from which,

$$J_h = \frac{Nu}{Re Pr^{1/3}} \quad (3.21)$$

Colburn applied this expression to a wide range data for flow and geometries and found it to be quite accurate for conditions where there is no form drag and $0.5 < Pr < 50$.

Chilton and Colburn [53] used mass transfer results of **Sherwood and Gilliland** and some unpublished data to examine their postulation. They showed that the J factor of heat transfer could also be used for estimating mass transfer coefficient. They found that the relation of J factor predicts the values of mass transfer coefficients in close agreement with experimental mass transfer data and they defined the mass transfer J factor as:

$$St_m Sc^{2/3} = \frac{c_f}{2} = J_d \quad (3.22)$$

from which,

$$J_d = \frac{Sh}{Re Sc^{1/3}} \quad (3.23)$$

The analogy is valid for gases and liquids within the range of $0.6 < Sc < 1000$. **Chilton and Colburn** stated that their analogy can be used not only for flow inside tubes, but also for flow across tubes and tube banks and flow over plane surfaces. The complete **Chilton-Colburn** analogy is:

$$J_h = J_d = \frac{c_f}{2} \quad (3.24)$$

This relates the three types of transport in one expression.

The friction factor c_f contains only the skin friction and no form drag. An important issue here, is that this analogy assumes small mass transfer rates which do not affect the flow pattern in the boundary layer (i.e. it is only applicable for the non-blowing case).

Kays and Crawford [3] an analogy between momentum, heat and mass transfer in an outgassing boundary layer is followed. The approach of [3] results in a set of correlations for friction, heat transfer, and mass transfer of the form (some of these equations given in chapter two):

$$f = f^{\circ} \varphi(\beta_f) \quad (2.6)$$

$$St_h = St_h^{\circ} \varphi(\beta_h) \quad (2.10)$$

$$St_m = St_m^{\circ} \varphi(\beta_m) \quad (2.14)$$

where the superscript $^{\circ}$ denotes the transport coefficient that would be observed in a boundary layer with the same geometry but with negligible blowing or suction. The above three equations give the general form of the correlations that are given previously in fluid flow, heat transfer, mass transfer sections.

For a flat plate with a constant property boundary layer, the correction function φ has the same form for momentum, heat and mass transport processes (**this relies heavily on the *Chilton-Colburn analogy***) :

$$\varphi(\beta) = \frac{\ln(1 + \beta)}{\beta} \quad (3.25)$$

The derivation of eq. 3.25 for the momentum transfer case is given in Appendix B. The respective blowing factor β have the following form:

$$\beta_f = \frac{\dot{m}/G_\infty}{f} \quad (3.9)$$

$$\beta_h = \frac{\dot{m}/G_\infty}{St_h} \quad (3.26)$$

$$\beta_m = \frac{\dot{m}/G_\infty}{St_m} \quad (3.27)$$

Debusschere and Ragland [11] analogy for the blowing tube banks relied on the **Kays and Crawford** [3] analogy which actually depends on the **Chilton-Colburn** analogy [53], they used the following equations to define the correction of the outgassing friction factor $\varphi(\beta_f)$ and to define the friction blowing factor β_f and to find the effect of outgassing on heat and mass transfer processes in general, a correlation for the experimental data was used in the following form:

$$\frac{St}{St^o} = \varphi(\beta) \quad (3.28)$$

and the following form for the function $\varphi(\beta)$ was chosen given in [15]:

$$\varphi(\beta) = \frac{1}{(1 + \beta)^c} \quad (3.29)$$

where,

$$\beta_h = \frac{\dot{m} \rho_a}{G \rho_w} \frac{1}{St_h} \quad (3.30)$$

and

$$\beta_m = \frac{\dot{m} \rho_a}{G \rho_w} \frac{1}{St_m} \quad (3.31)$$

Where $G = \rho U_c$, is the mass flux in the most narrow cross section between two tubes.

However, the correlations given in [3] are all for flat plates and constant property boundary layers. For cylindrical tube banks little data is available in [11], and for other geometries or for variable property systems, no information was found in the literature. Part of the objective of the present study is to examine what elements of this analogy still hold for the boundary layer around an outgassing cylinder with significant levels of combined heat and mass transfer in which the constant property approximation does not hold.

CHAPTER FOUR

Experimental Work

4.1 Introduction

It is a well known fact to prove the reliability of any model is when it matches the experimental work. Therefore; a test rig was designed and two types of experiments were conducted for the purpose of study the effect of outgassing on the friction factor and on mass transfer coefficient.

This chapter gives the general concepts of the present work. Second it gives the design of the rig and the details of the test section followed by the calibration of the used instruments. The measurements procedures are described at the end of this chapter.

4.2 General Concepts

Little quantitative information is available on how outgassing through cylindrical walls affects on the transport coefficients. For the purpose of expanding data, this thesis studies the influence of outgassing on the friction factor and mass transfer coefficients at the tube surface as in the surface of burning logs randomly stacked in a fixed bed combustor that was explained in

chapter one. The goal is to develop a correlation for this influence from measurements in an outgassing staggered tube bank. The technique used for mass transfer measurements are described and the chosen method is worked out in detail.

4.3 Experimental Facilities and Instrumentation

(Experimental Set-up)

A test rig was built for the present work consisting of a wind tunnel with staggered row tube bank; in the test rig, two main flows can be distinguished, the air flow and the water flow. These two flow directions are represented schematically in Fig. 4.1 and the details of the test section and the tube bank arrangement is shown in Fig. 4.2.

Fig. 4.1a, gives a view of the air flow in the test rig. Fig. 4.1b includes the cross section A-A of the tube bank, pictures the components of the water loop. The central tube (13), was set up to evaporate water. The others were used to simulate the general flow pattern in an outgassing tube bank by blowing compressed air through their walls. To have the best possible flow characteristics, an induced flow wind tunnel was built. Rather than blowing the air into the test section, the air was sucked through the tube bank by a centrifugal fan. The general operation of the test rig is as follows:

According to Fig. 4.1a, air drawn into the test section (2) by means of the exhaust fan (3). To have a good inlet profile, a contraction (1) was positioned up front. The inlet contraction was designed to give the air entering the test section with a flat velocity profile. After the tube bank, a centrifugal

fan was located and a slide valve (4) was used to vary the flow rates. To minimize the influence of the downstream turbulence a long straight distance of the duct with the same cross section as the test section was placed between the tube bank and the exhaust fan.

Compressed air was supplied from a compressor (5), which has a pressure gauge (6) through the main valve (7) and an air rotameter (8). The flow rate was measured by a Pitot tube and an inclined manometer (9). The pressure drop across the tube bank was determined with a differential pressure meter (10) connected to two static pressure taps both in front and behind the test section. The air temperature was measured by two thermocouples (11 and 11') and the relative humidity was obtained from a digital RH% meter (12) taking air samples on both sides of the tube bundle. The ambient temperature was measured by a digital thermometer.

On the water side (Fig. 4.1b), the most important part was the central tube (13), through which water was pumped by a pump (16), the water was heated in a thermostatic water bath (15) and went back into the tube. The water flow rate was obtained from the rotameter (18) and controlled by the main valve (17). The outlet water flow rate from the center tube was measured in a reservoir (19) with known volume and the reservoir was weighed before starting to determine the mass loss (i.e. the mass of the evaporated water) in the system. A very important variable was the outer surface temperature of the tube. This was measured using three thermocouples mounted on the tube wall (20).

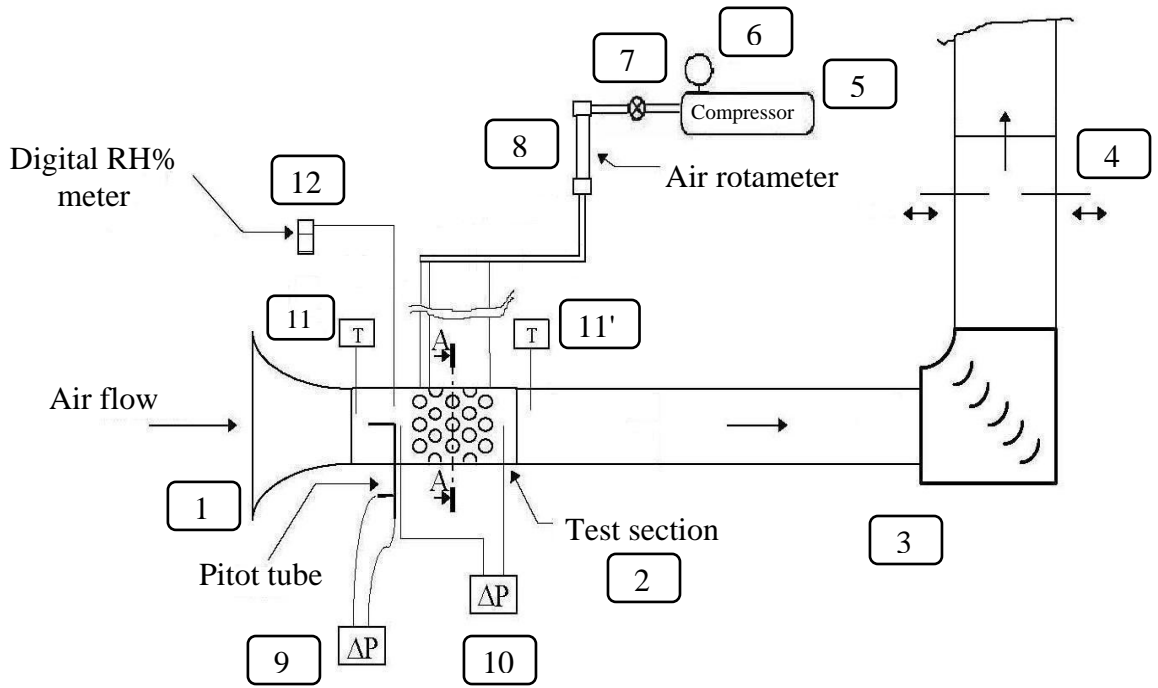
Two types of experiments were conducted. First, the overall friction characteristics of the tube bank were determined. Friction factors, with and

without outgassing were measured for different Reynolds numbers. The second set of experiments measured the mass transfer characteristics of the tube bank as a function of Reynolds number and outgassing.

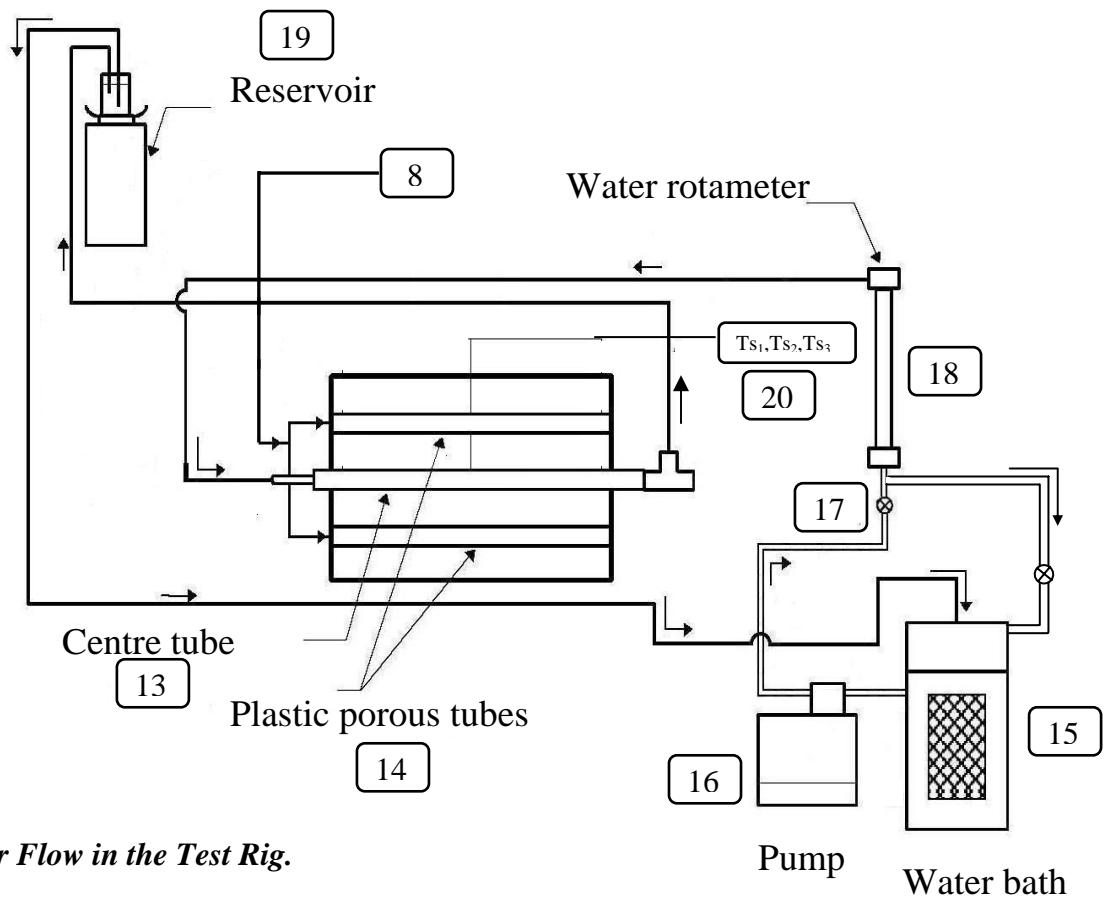
Several quantities need to be measured in order to be able to extract transport coefficients from the measurements. The most important are:

- bulk air flow rate
- pressure drop across the tube bank
- water evaporation rate
- surface temperature of the tube
- conditions of inlet air flow (temperature and humidity)

Apart from these variables, pressure drop across the tube bank is measured, as well as the conditions of the air flow behind the test section. The organization of all this is explained in the next sections. Fig. 4.3 shows the experimental rig Photograph.



a) Air Flow in the Test Rig.



b) Water Flow in the Test Rig.

Fig. 4.1: Test Rig.

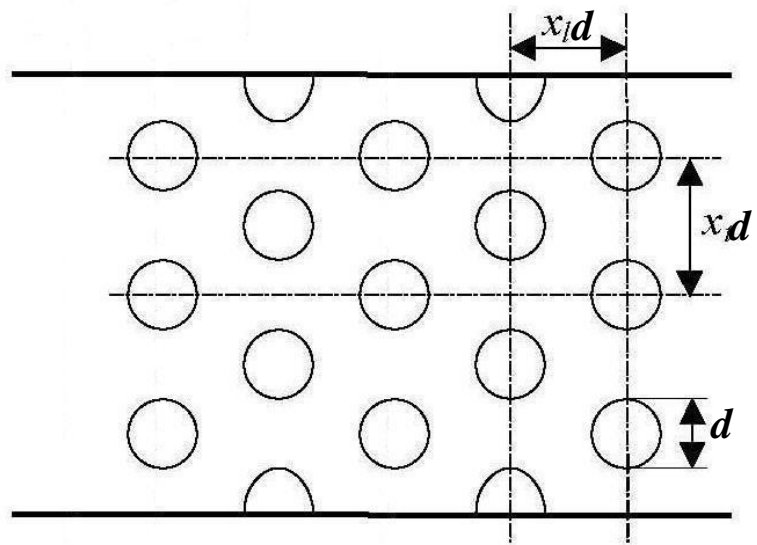


Fig. 4.2: Tube Bank Arrangement.

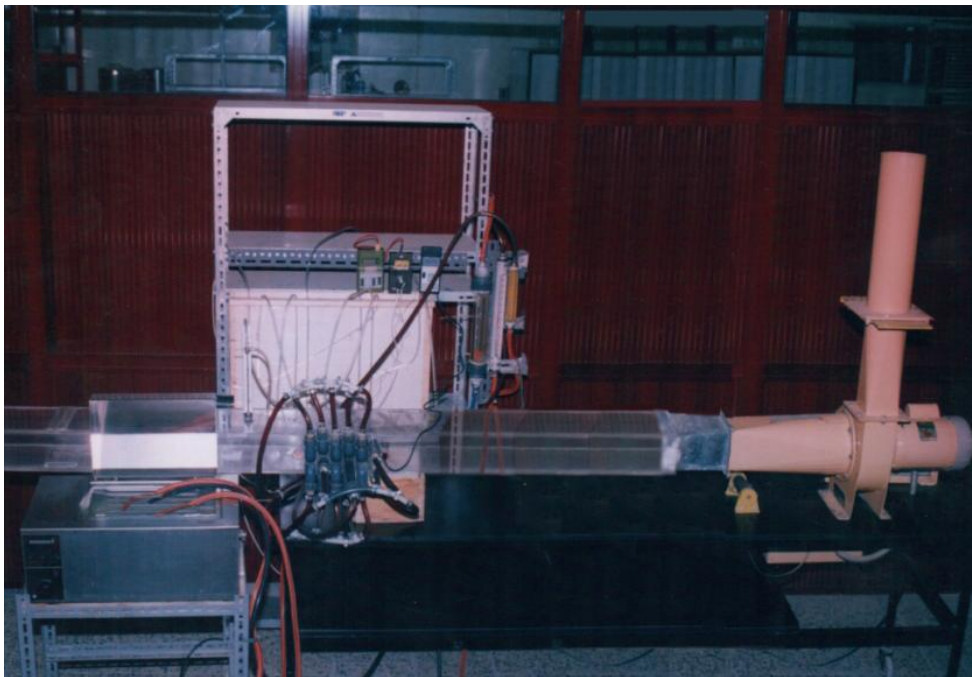


Fig. 4.3: Rig Photograph.

4.3.1 Experimental Apparatus

4.3.1.1 Induced Centrifugal Fan

The centrifugal fan used in the present experimental tests contains an A.C. motor gives 75 output watts and 50 Hz. The outlet cross sectional area is a circular shape with diameter equal to 12 cm.

Control valve systems are considered one of the important parts in any experimental system, therefore; the mass flow rate inside the tunnel in this study regulated through a gate valve located at the exhaust pipe of the induced centrifugal fan. This gate consists of a square plate and moves in a direction parallel to the axis of the exhaust pipe and perpendicular to its center axis. This plate has measures to give by its movements an opening area of the exhaust pipe of 0%, 10%, 20%, 30%, 40%, 50%, 60%, 80% 90%, 100% (fully opening). The movement of this gate valve permits partial and full opening for the exhaust pipe, therefore; mass flow rate inside the wind tunnel and the Reynolds number will be regulated in accordance.

4.3.1.2 Wind Tunnel

A rectangular wind tunnel was manufactured for the purpose of the present study. The wind tunnel was made of plexi glass with the thickness of 0.6 cm for the top and bottom sides and 1cm for the two other sides. The test section was a part of the wind tunnel consists of a packed tube banks mounted in a staggered arrangement across the tunnel.

4.3.1.3 Air Rotameters

Two calibrated air rotameters were used in the present work, the first one with the range 0-100 l/min at 20°C and the second with the range 6-52 m³/hr at 20 °C and under atmospheric pressure.

4.3.1.4 Water Rotameter

The calibrated water rotameter used in the experimental work has a flow rate range from 0 to 1000 ml/min at 20 °C.

4.3.1.5 Digital Thermometers

Three digital thermometers (model Mendes, GHT and Genway) were used in the present work to measure the temperature inside the duct and the ambient temperature. All the thermometers used in the present work experiments have sensors of *K-type* probe. Three readings for the air temperature were recorded along the y-axis of the duct in each side of the test section.

The thermocouples used to measure the surface temperature of the centre tube has very thin sensors made of nickel-nickel crom and its reader connected to a selector to change the sensor and these sensors *K-type* probes also.

4.3.1.6 Relative Humidity Meter

A digital relative humidity/temperature meter, type HT-3004, was used to measure the relative humidity and the sensor type for the humidity measurements was a high precision thin film capacitance sensor and the temperature one was naked bead type *K-type* thermocouple probe.

4.3.1.7 Pitot Tube

A Pitot-static tube made of stainless steel material was used to measure the air flow rates inside the tunnel

4.3.18 Pump

A centrifugal PVC water pump was used in the present work to supply the hot water from the water bath. The pump used has a pumping capacity about 24 m³/hr (for zero head) and 1 bar at the discharge side.

4.3.1.9 Water Bath

A thermostatic water bath, type memmert, was used to obtain a hot water for the experiments with the temperature range.10-95°C.

4.3.2 Test Section

The test section shown in Fig.4.1, where at least 5 rows of three tubes each were required since it takes about two tube rows before the turbulence level in a tube bank to overcome the entrance effects and the last row suffers

from exit effects. For the reason of comparison, the size of the tubes and their pitches were chosen that is documented in literature by **Kays and London** [49] and **Debusschere and Ragland** [11]. The final design dimensions are given in Table 4.1.

The porous tubes chosen were plastic (PVC tubes) with a pore size of approximately 0.5 mm which is the minimum pore size that can be obtained practically.

The walls of the test section were made out of Plexiglas so that the location of measurement probes was visible from the outside. Holes for the Pitot tube and the pressure taps were drilled at least 2 diameters away from the actual tube bank to minimize the effects on the flow pattern in the tube bundle.

4.3.2.1 Compressed Air Control

The compressed air used to blow through the walls of the tubes, and it was supplied from a compressor with a control valve to set the pressure and a pressure gauge to measure the pressure. There is another control valve in front of the air rotameter to control the air flow rate. It was not possible to keep the flow rate in the rotameter exactly constant for a long time during the run, where during normal, steady state operation though; fluctuations were sufficiently small such that manual adjustment was possible.

Table 4.1: Characteristics of the Tube Bank [11].

Rows of tubes	n_{rows}	5
Tubes per row	n_{tubes}	3
Outside diameter of tubes (mm)	d	25.4
Inside diameter of tubes (mm)	d_i	21.4
Length of tubes (mm)		203.2
Longitudinal pitch	x_l	1.5
Transversal pitch	x_t	1.5
Pore size (mm)		0.5
Total cross section (m ²)	A	203.2 mm by 114.3mm = 0.0232
Narrowest cross section (m ²)	A_c	0.0077

4.3.2.2 Pressure and Temperature Difference across the Test Section

The head loss was measured by a differential manometer. Pressure taps were located in the side wall of the plexi glass in front and behind the test section. The fluid used in the differential manometers was gas oil and its density measured in the lab using a standard picknometer for different temperatures and found an equation to express its density as a function of temperature for the given range, as given below:

$$\rho = 811.961 + 0.720148 T - 0.0209091 T^2 \quad (4.1)$$

where the correlation coefficient $R^2 = 1.00001$ and T in $^{\circ}\text{C}$.

For the air temperature measurements, calibrated digital thermometers were used and its probes located across the duct in front and behind the test section and they connected to digital readers.

4.3.2.3 Velocity Measurement

A Pitot-static tube was used in this study to measure the velocity of the air inside the duct. It was used to measure both the impact and static pressure and to find the dynamic pressure. This pressures was indicated with assistance of inclined manometer (with angle 20°), filled with the gas oil used in the measurement of the pressure difference mentioned in the previous section.

The velocity can be calculated at any position use the following equation:

$$U = \sqrt{\frac{2 \Delta p}{\rho}} \quad (4.2)$$

Where,

$$\Delta p = \Delta h(\rho_m - \rho)g \quad (4.3)$$

Δh is the head difference. The head difference was read at each 0.5 cm distance vertically to find the average air velocity.

4.3.2.4 The Plastic Tube Bundle

The plastic tubes were mounted in staggered arrangement as shown in Fig.4.1, and their ends were capped. The pores (0.5 mm) were in staggered arrangements along the plastic tubes with an equal longitudinal and transversal pitch of 2.5 mm.

For the mass transfer measurements, three thermocouples with string sensors (nickel-nickel crom) were positioned in the tube wall. These sensors were located in the middle cross section of the centre tube, at the forward stagnation point, and at the top and the bottom of the tube. These sensors connected to the one digital reader (*K- type*) have a selector to select the used sensor.

4.3.2.5 PVC Flanges

PVC flanges were used to fix and connect the tube bundles in the wind tunnel. The flanges were fitted on the out side surface of the PVC tubes and cemented by high quality PVC cement to prevent leakages.

4.3.2.6 Hot Water Control

The water heater provided warm water to the heat exchanger. The temperature of the water in the thermostatic bath was the way depends to control the water temperature.

The hot water supplied by a centrifugal PVC water pump and controlled by two valves made of PVC. One valve was placed at the entrance

of the test section in front of the water rotameter to control and adjust the center tube flow rate. Other valve was placed in the by-pass line to help in obtaining the desired flow rate in the test section and to circulate the water for obtaining constant solution temperature. By varying the water temperature inside the center tube, different values of mass transfer blowing factor could be obtained. Therefore, the mass transfer experiments were carried out for different values of temperatures ranged from 40°C to 90°C. At low temperatures (<40°C), very low evaporation rates were obtained that couldn't be measured accurately. In present work, the hot water temperatures couldn't exceed the temperature higher than 90°C because of the difficulties in pumping the water at highest temperature and measuring its flow rates.

4.4 Calibration of the Instruments

For the accuracy of the measurements, the instruments used in the test set-up were calibrated before starting the experiments.

4.4.1 Volumetric Air Flow

The air flow rate in front of the test section was measured with a Pitot tube. Since this only gives the velocity at one point at the time, integration over the cross section was necessary. The log-linear transverse method was used with measuring points located in a rectangular grid. The velocity at each measurement point was assumed to be the average of the velocity in the rectangle around it. The total flow rate was obtained by summing all the velocities each multiplied with their respective area.

The velocity distribution was recorded for different flow rates in order to obtain an estimate of the non-uniformity of the profile. It turned out that the non-uniformity, defined as $(U_{\max} - U_{\min}) / U_{\max}$ was smaller than 8 % for all profiles. It should be pointed out though that the highest non-uniformities were found at the lowest flow rates where the difference in the measured Δp 's (Δp being the total pressure minus the static pressure in the flow) was of the order of the resolution of the manometer. Since the measured velocity is proportional to $\sqrt{P_{tot.} - P_{stat.}} = \sqrt{P}$, a small error in Δp will cause large errors on the calculated velocity for these low flow rates which means the non-uniformity is not determined very accurately. For the highest flow rates, the non-uniformity dropped to about 3%.

To avoid the necessity of taking about 25 data points with a Pitot tube for each flow rate measurement, a correlation was developed between the total flow rate and the Δh at the center line. A good fit (correlation coefficient $R^2 = 0.997$) was obtained with the following formula:

$$V(m^3 / s) = 0.087 \Delta h_{cl}^{0.494} \quad (4.4)$$

where the volumetric flow rate is in m^3/s and Δh_{cl} is in mm gas oil. Fig.4.4 represents the above correlation for the flow rate.

4.4.2 Rotameters

There were two rotameters in the system, one measured the flow of the compressed air and the other measured the water flow rate.

4.4.2.1 Air Rotameter

The air rotameters were calibrated against a Root meter. The flow rates are converted into the equivalent flow rates at standard temperature. Assuming the temperature inside the rotameter was the same as in the surrounding. The calibration curves are given in Fig. 4.5, which gives the actual volumetric flow rate in m^3/hr as a function of the correlated reading.

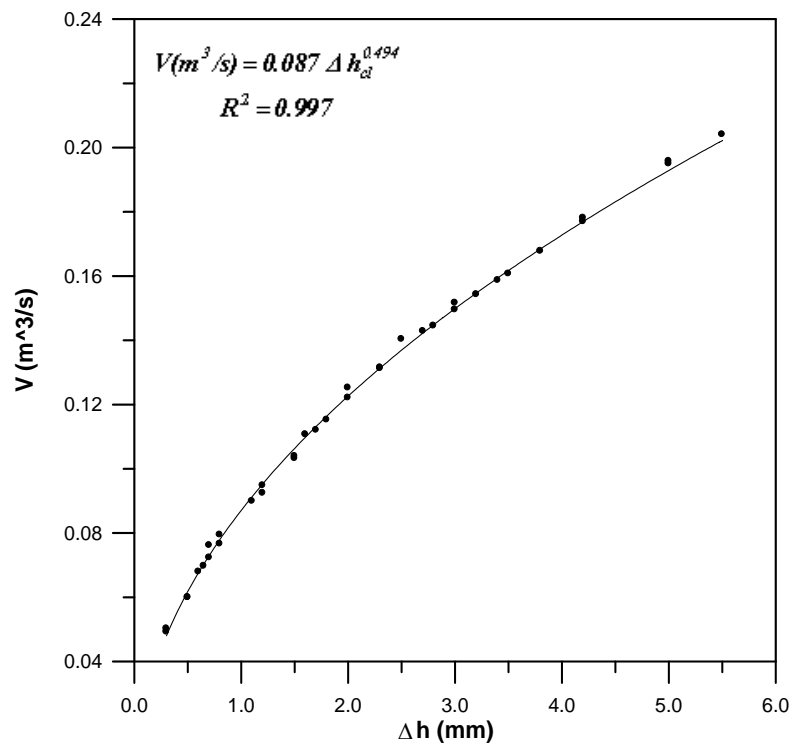


Fig. 4.4: Correlation of the Total Flow Rate as a Function of Center Line Pressure

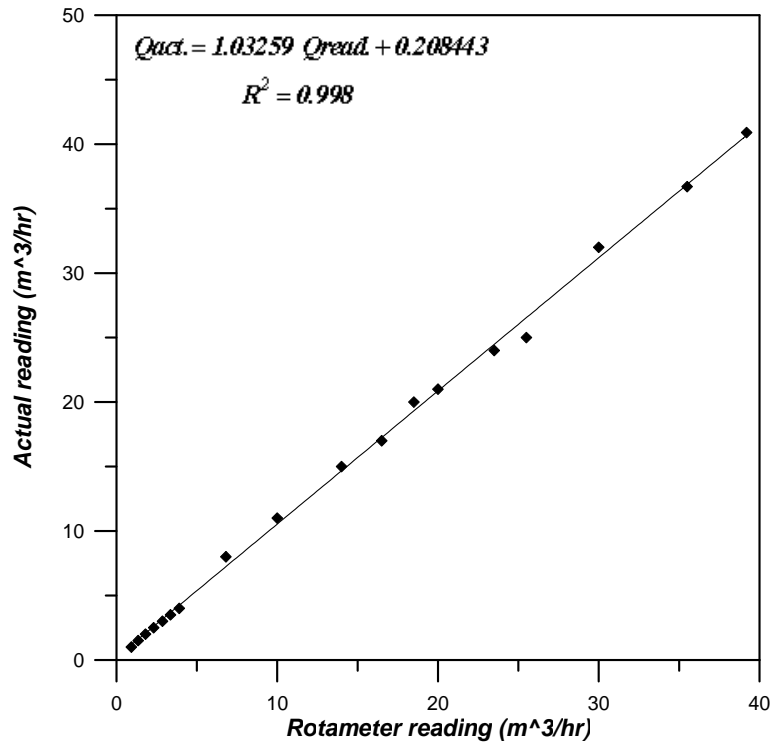


Fig. 4.5: Calibration of Air Rotameter.

4.2.2 Water Rotameter

The water rotameter was calibrated at each worked temperature by pumping known volumes of water through it at a constant flow rate and measuring the total pumping time by a stop watch. The calibration of the water rotameter for each working volumetric flow rate with different temperatures is given in Fig.4.6.

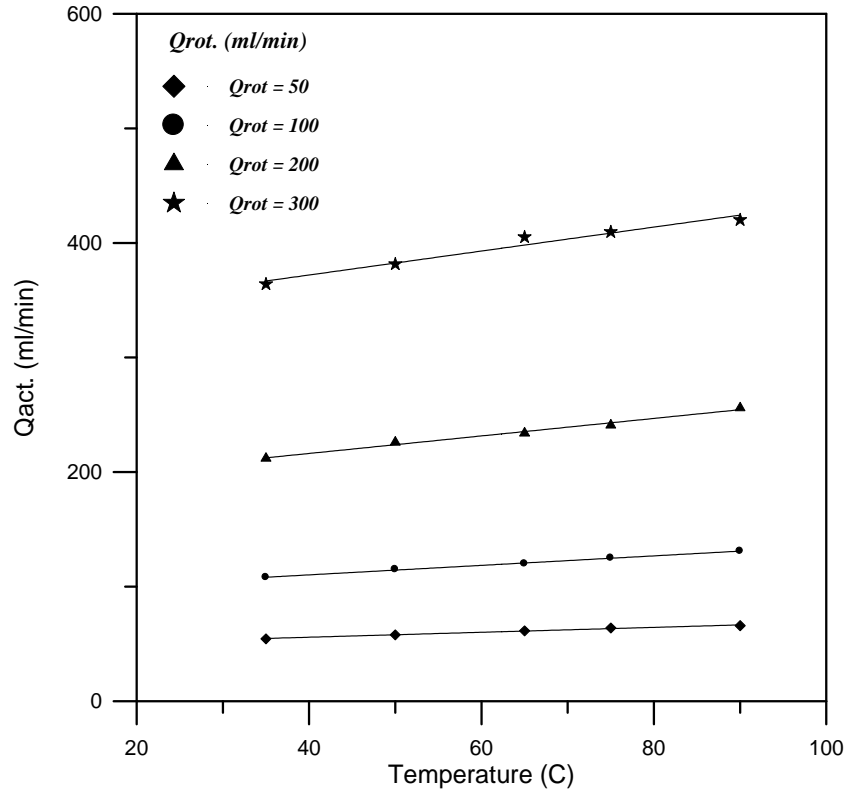


Fig. 4.6: Calibration of Water Rotameter at Different Temperatures.

4.4.3 Thermometers

Each of the digital thermometers used were calibrated with standard thermometer at the worked range of temperatures.

The calibration of the thermometers (Mendes, GHT and Genway models) used to measure the temperatures are given in Figs. 4.7, 4.8 and 4.9 respectively, while the calibration of the thermocouples used to measure the surface temperature of the center tube is given in Fig. 4.10. The accuracy of the readings was being with $\pm 2\%$.

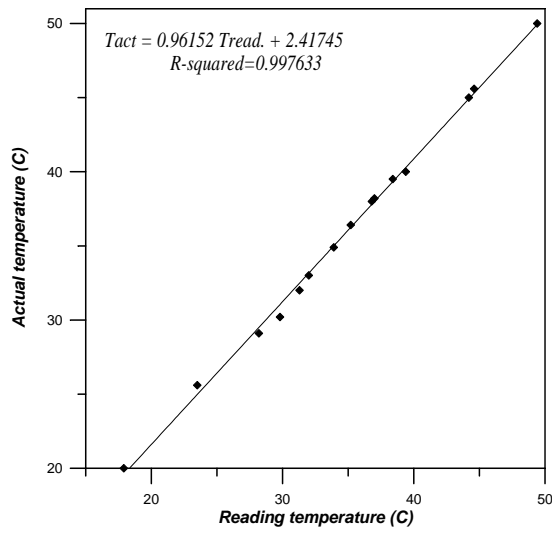


Fig. 4.7: Calibration of Thermometer (1).

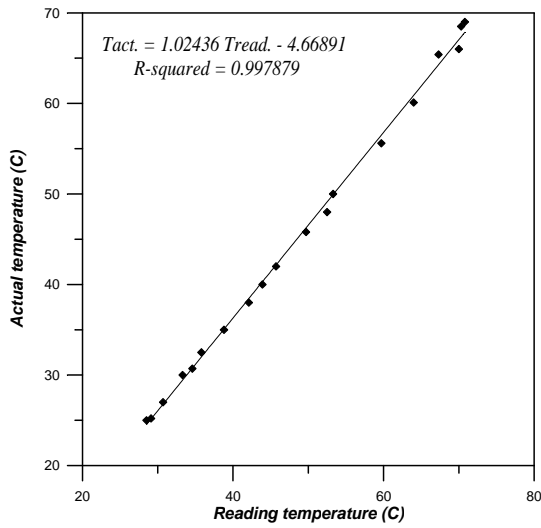


Fig. 4.8: Calibration of Thermometer (2).

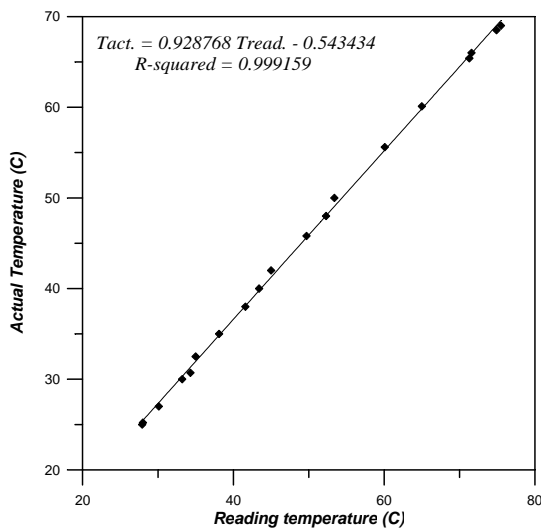


Fig. 4.9: Calibration of Thermometer (3).

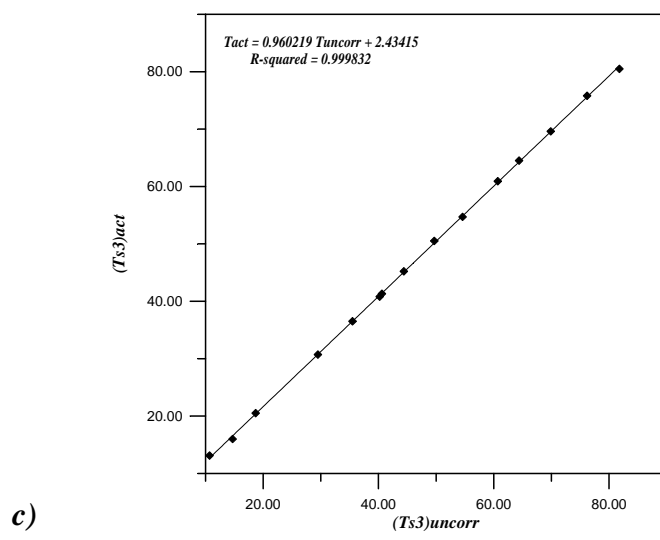
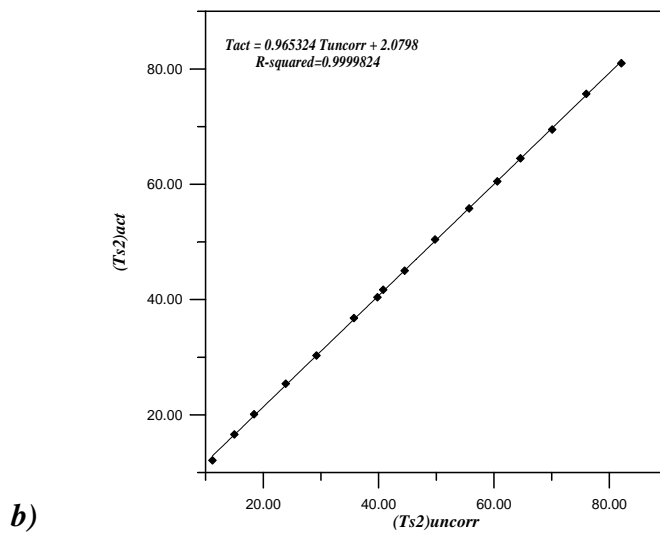
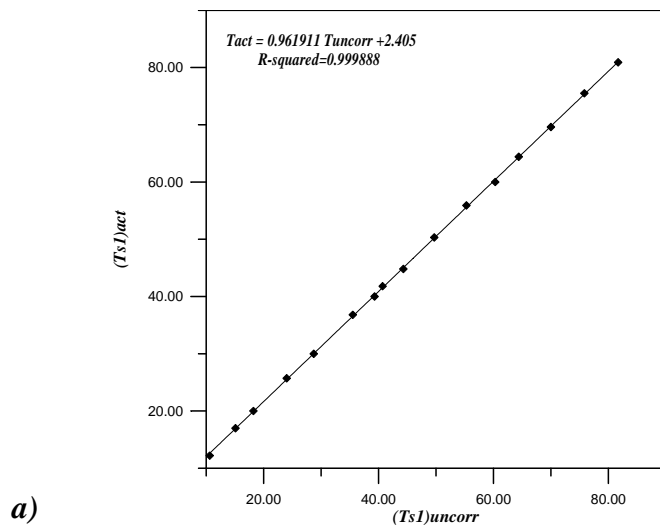


Fig.4.10: Calibration of the Thermocouples

4.5 Measurement Procedures

The test rig, as described in the previous sections, was used for two different types of measurements. Initially, fluid flow characteristics of the tube bank, i.e. friction factors and static pressure difference, were examined. Later on, tests concerning mass transfer were conducted.

4.5.1 Fluid Flow Test

For the pressure drop measurements, an air flow rate was set by valve (7) and was measured by Pitot tube (9). Various amount of outgassing were set by the valve and measured by the rotameter (8).

The static pressures were recorded in front of and behind the test section (10) using a differential manometers with a pressure taps in the wall of the wind tunnel.

The temperature of the ambient and the temperature in front and behind test section were also recorded (11, 11').

The above steps repeated for three outgassing rate and for each specified outgassing rate made about 12 runs for different air flow rate inside the tunnel controlled by the gate valve (4).

4.5.2 Mass Transfer Test

The following steps were taken in each data run (all numbers refer to Fig. 4.1b):

- 1) Switch on all electronic equipment.
- 2) Set the water bath (15) to the desired temperature.
- 3) Start up the pump (16) to make the water circulate and get all the air out of the system.
- 4) Adjust the air flow rate by valve (4).
- 5) Adjust the pump rate using valve (17) such that the tube wall is wet but not dripping.
- 6) When the outlet water from the centre tube starts to fill the reservoir (19), start the stop watch.
- 7) Record the relative humidity RH% (12) and the temperatures before and after the test section (11,11')
- 8) Read the Pitot tube pressures (9)
- 9) Record the water flow rate.
- 10) Record the temperatures of the surface of the centre tube (20).
- 11) Weighing the final mass of water in the reservoir and stop the stopwatch.
- 12) To take another data point, e.g. at a different water temperature, adjust the water bath set point, and start the whole process over again.

Usually about 10 data points for different water temperatures were taken in one run of constant Reynolds number.

CHAPTER FIVE

Results and Discussions

5.1 Introduction

The conversion of the data into non-dimensional results with an analysis of the data and error discussion is described along in this chapter. The correlations are also presented for the non-dimensional results of the friction factor and mass transfer measurements.

The present work aims to give further insight into the phenomena of outgassing and its effect on momentum and mass transfer.

5.2 Friction Factor Measurement

For the present work, the friction factors are subject to the effect of blowing for the porous tube bank. The friction factor determination which was obtained from the pressure drop across the tube bank measurement and the row data for the pressure drop measurement consist of:

- The Δp from the Pitot probe, measuring the main flow rate (mm of gas oil)
- The pressure drop across the tube bundle (cm of gas oil)
- The volumetric flow rate through the air rotameter (m^3/hr)
- The temperature before the test section
- The ambient temperature

The measured pressure drop across the tube bank was non-dimensionalized to obtain an overall friction factor f , which is defined in this work as (eq. 3.6):

$$f = \frac{\Delta p}{n_{row} \rho \frac{U_s^2}{2}} \quad (3.6)$$

where,

$$\Delta p = \Delta h(\rho_m - \rho)g \quad (4.3)$$

The friction factors were measured for different values of Reynolds numbers in front of the test section, which was defined in this study as:

$$Re = \frac{U_s d}{\nu} \quad (3.4)$$

The blowing rate accounted by the blowing factor definitions, are given by:

$$\beta_f = \frac{\dot{m}}{G_\infty} \quad (3.8)$$

Here, the blowing factor definition represent the ratio of the mass flux through the wall of the tubes (mass flow rate per unit surface area of the tube, \dot{m}) to the free stream mass flux G_∞ . This mass flux was calculated based on Reynolds number in front of the test section (Re), i.e. neglecting the effect of the mass added to the bulk flow from the outgassing.

And, the other one:

$$\beta_f^* = \frac{\dot{m}/G_\infty}{f} \quad (3.9)$$

This is more complicated definition, β_f^* is really the same "blowing factor", but its physical interpretation differs. It is the ratio of the transpired momentum flux to the wall shear force [3].

5.2.1 Friction Factor Measurements for non-Blowing Case

The first tests that have done concern the pressure drop across the five row tube bank as a function of Reynolds number for non-outgassing cylinders. Since there is no blowing, these pressure drops are only dependent on Re . The obtained data of the measured variables are given in Table 5.1.

As shown in Fig. 5.1, the pressure drop is fitted well with the formula:

$$\Delta p(Pa) = 1.683 \times 10^{-5} Re^{1.79} \quad (5.1)$$

$$R^2 = 0.998$$

where Δp is the pressure drop across the tube bundle in Pa and Re is the Reynolds number in front of the test section as defined previously. This pressure drop was then non-dimensionalized to obtain an overall friction factor f by eq. 3.6.

The resulting friction factors are plotted versus Reynolds number in Fig.5.2 and yielded to the following correlation for the friction factor as a function of Reynolds number $f(Re)$:

$$f^o = 26.573 Re^{-0.212} \quad \text{for } 3000 < Re < 18000 \quad (5.2)$$

$$R^2 = 0.950$$

Table 5.1: Friction Factor Results for the Non-Blowing Case.

Exp. No.	Δh_{cl} (mm)	Q_{duct} (m ³ /s)	Δh (cm)	ΔP (Pa)	Re	f^o
1	0.25	0.0438	0.63	50.1257	3374	4.804
2	0.6	0.0676	1.23	97.8644	5200	4.172
3	0.9	0.0826	1.88	149.5688	6347	4.285
4	0.8	0.0779	1.74	138.4189	5983	4.276
5	0.9	0.0826	1.70	135.2598	6353	3.964
6	1.1	0.0912	2.29	182.1720	7002	4.198
7	1.2	0.0952	2.46	195.7943	7336	4.144
8	1.5	0.1063	2.87	228.4640	8206	3.819
9	1.8	0.1163	3.40	270.6322	8988	3.774
10	1.9	0.1194	3.63	288.9159	9223	3.789
11	2.2	0.1284	4.18	332.7993	9943	3.722
12	2.6	0.1395	4.92	391.7160	10798	3.739
13	2.9	0.1472	5.19	413.1793	11386	3.562
14	3.1	0.1521	5.61	446.4695	11724	3.591
15	3.5	0.1615	6.43	511.3811	12369	3.604
16	3.8	0.1682	6.84	543.9886	12882	3.587
17	4.1	0.1746	7.32	582.2640	13400	3.572
18	4.5	0.1829	7.84	623.4098	13979	3.505
19	4.9	0.1907	8.43	670.1458	14540	3.430
20	5.2	0.1964	9.05	719.4329	14973	3.441
21	5.7	0.2055	9.80	779.1726	15682	3.439
22	6.2	0.2142	10.63	845.0885	16332	3.412
23	6.7	0.2226	11.35	902.2479	16955	3.402
24	7.1	0.2291	12.00	953.9185	17447	3.369

5.2.1.1 Comparison with Literature

To verify the obtained friction factors, they were compared to values found in the literature by **Kays and London** [49]. These values are for a tube bank with a pitch of 1.5 (both longitudinal and transversal), which is similar to the tube bank used in this work. The friction factors measured by **Kay and London** [49] for smooth tubes without blowing are available for Reynolds numbers were below the values of Reynolds number worked in this study. This means the rigorous comparison between the present work and **Kays and London** work is not feasible. Therefore, by using the same definitions for Reynolds number and friction factor given previously as the same used by **Kays and London** , their data were compared with the measured friction factors for $\beta_f = 0$.

Debusschere-Ragland used the similar tube banks of **Kays and London** with the same definitions for Reynolds number and friction factor but for the Reynolds number range higher than in **Kays and London** work. **Debusschere and Ragland** got the following correlation for the non-blowing tube bank:

$$f^o = 39.0 Re^{-0.25} \quad \text{for } 3000 < Re < 16000 \quad (2.9)$$

while in the present work eq. 5.2 for the non-blowing case was obtained. Fig. 5.3 gives the comparison of the present work with **Kays-London** work [49] and **Debusschere-Ragland** work [11] for the non-blowing case. Present work gives a good agreement with **Debusschere-Ragland** work and with **Kays-London** work when extending Reynolds number range from 3000 to 18000.

5.2.1.2 Error Analysis

At lower values of Reynolds numbers ($Re < 8000$), some scatter was observed in the data as shown in Fig.5.2, and to analyze this error the predicted values of the friction factor versus the experimental values was plotted in Fig. 5.4 to show the deviation of the data points from 45° centre line, where this deviation increases at the higher values of friction factor (i.e. lower values of Reynolds number).

It is more obvious to analyze the data point by error bars. The absolute error definition was assumed to equal to the absolute error between the experimental values and the correlated ones. Fig.5.5 shows the error bars on the data points and shows generally that the error bars bigger at low Reynolds numbers, which is mostly due to the huge relative error on the pressure drop measurements by the Pitot tube. When the air flow rate gets very small, the pressure drop gets small accordingly this will cause an increase in the error on the velocity measurements due to the loss of accuracy in recording the small pressure drop, while at higher Reynolds numbers the errors get smaller because of pressure drop get bigger.

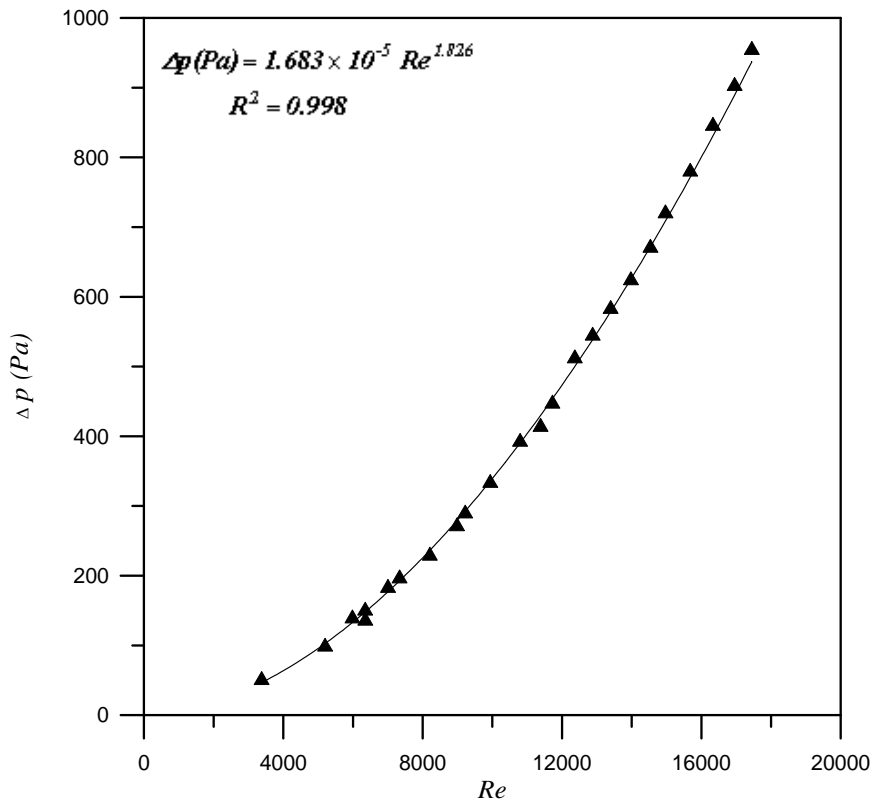


Fig. 5.1: Pressure Drop in the Non-Blowing Tube Bank.

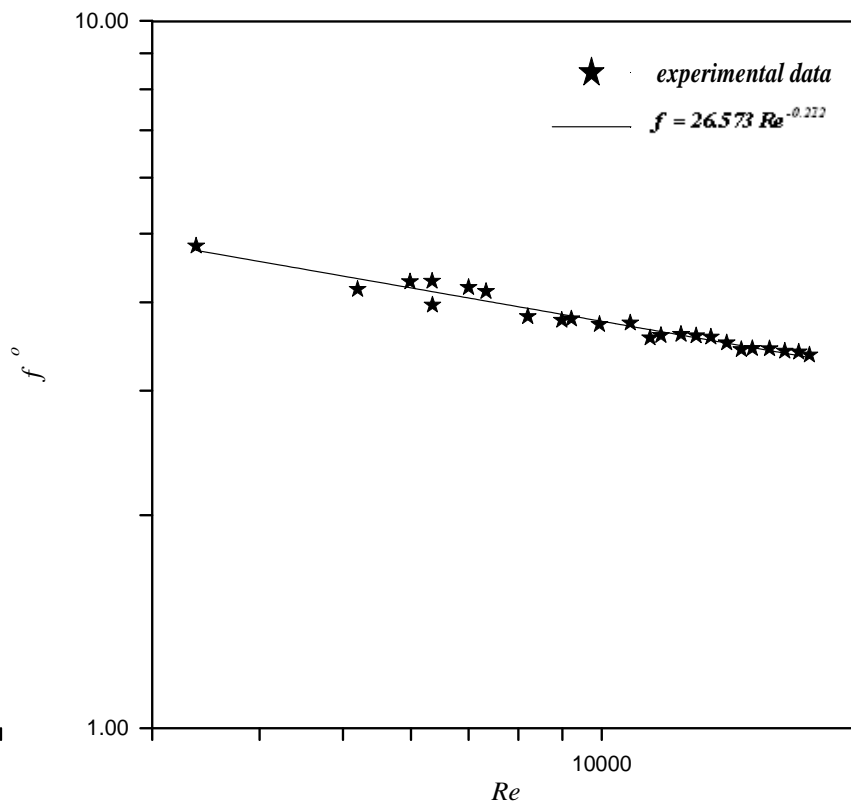


Fig. 5.2: Friction Factors for the Non-Blowing Tube Bank.

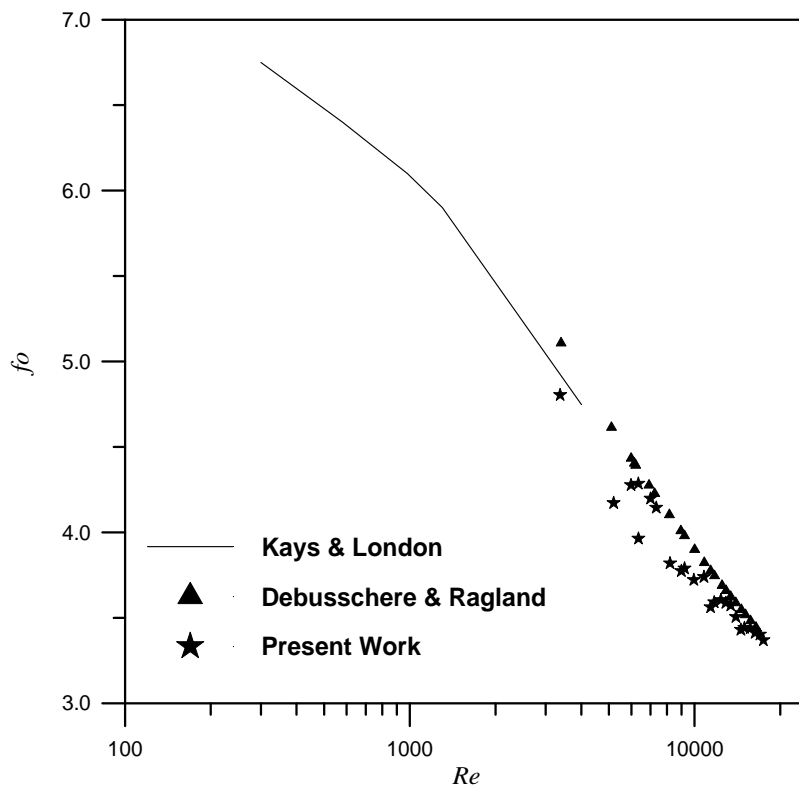


Fig. 5.3: Comparison of the Measured Friction Factor with the Literature for the Non-Blowing Case.

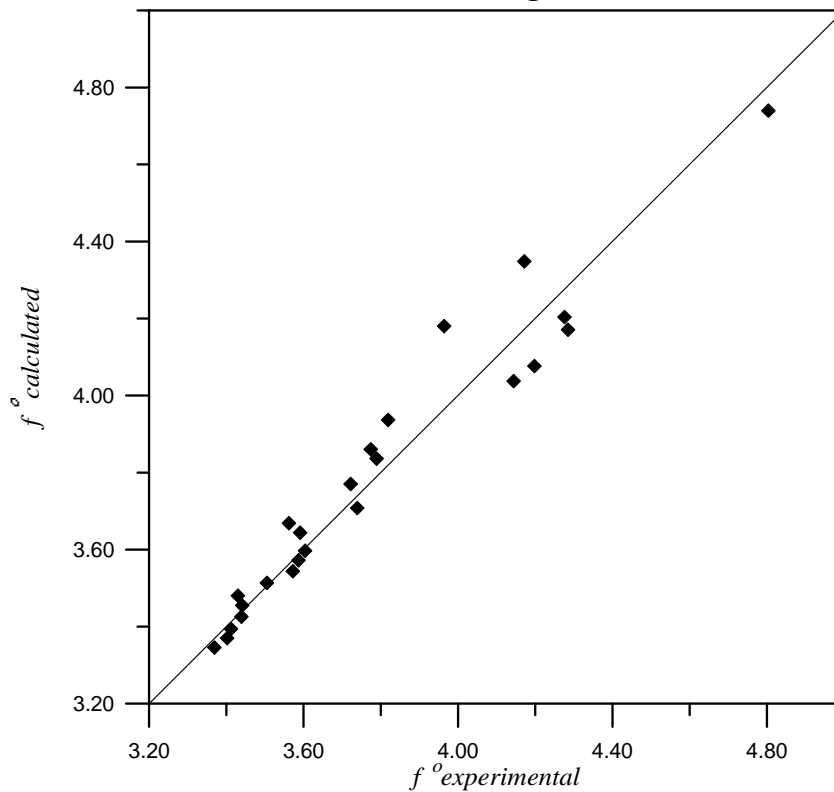


Fig.5.4: Expected Errors on the Predicted and Experimental Friction Factors in the Non-Blowing Tube Bank.

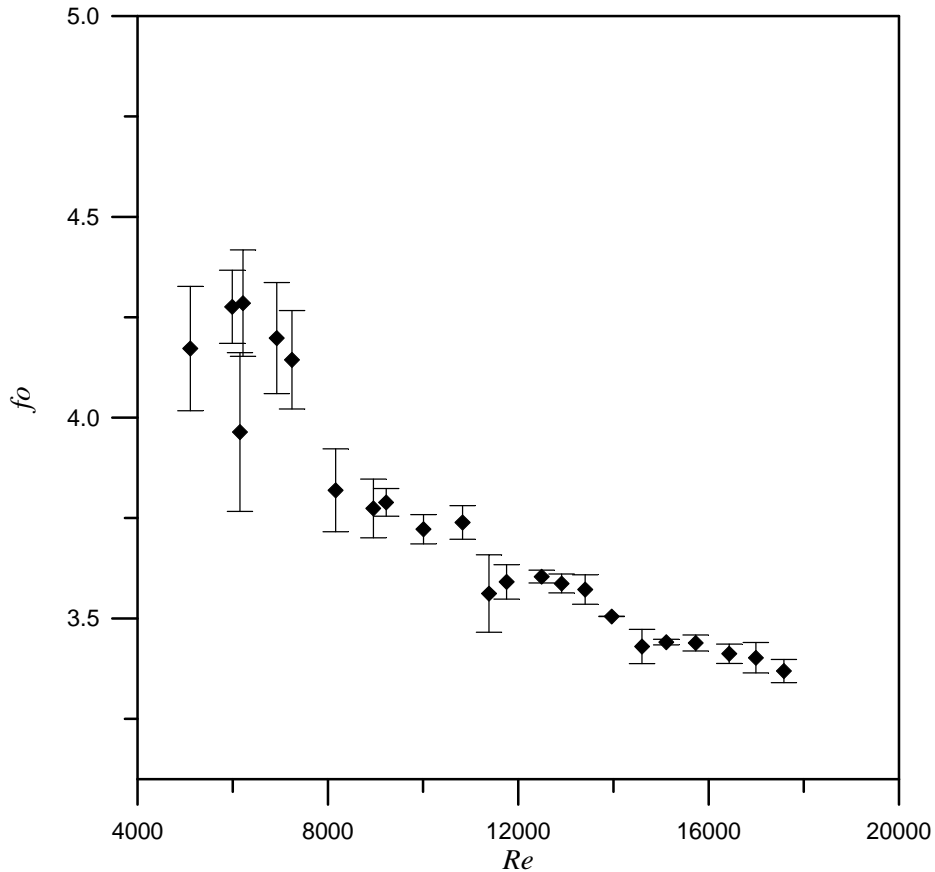


Fig.5.5: Expected Absolute Errors on the Friction Factors in the Non-Blowing Tube Bank.

5.2.2 Friction Factor Measurement with Blowing

The second set of data taken with an outgassing tube bank by blowing the compressed air through the walls of the tubes. The measured pressure drop again non-dimensionalized into friction factors. The blown air through the tube wall make a change in the momentum boundary layer, since the friction factors change as a function of both the *Reynolds number* in front of the test section, Re and the outgassing represented by the *blowing factor*, β_f

which is defined earlier in this chapter. The friction factor measurements in the case with blowing were measured once at constant blowing factor and another at constant Reynolds number. Most of the useful data for the two cases are listed in Tables 5.2 and 5.3. Part of these raw data is listed in Appendix C.

Table 5.2a: Friction Factor Measurements with $\beta_f = 0.0042$.

Exp. No.	$(Q_{\text{rot.}})_{\text{corr}} \times 10^3$ (m ³ /s)	$Q_{\text{duct}} \times 10^4$ (m ³ /s)	Δp (Pa)	Re	f
25	7.802	1770.016	848.2994	13759	5.04
26	7.085	1607.300	702.9902	12460	5.07
27	6.798	1542.725	657.6471	11949	5.15
28	6.368	1445.104	585.0817	11203	5.22
29	5.795	1314.528	490.1603	10218	5.28
30	5.077	1152.233	393.0036	8957	5.51
31	4.877	1106.659	365.0450	8595	5.55
32	4.074	924.414	260.7171	7186	5.679
33	3.500	794.239	199.1653	6180	5.875
34	3.356	761.456	186.7661	5935	5.99
35	3.070	696.843	157.9817	5432	6.05
36	2.639	599.172	119.6950	4670	6.20

Table 5.2b: Friction Factor Measurements with $\beta_f = 0.0031$.

Exp. No.	$(Q_{rot.})_{corr} \times 10^3$ (m ³ /s)	$Q_{duct} \times 10^4$ (m ³ /s)	Δp_s (Pa)	Re	f
37	6.368	1957.206	916.3848	15145	4.460
38	5.795	1780.927	766.0417	13806	4.500
39	4.934	1516.471	581.5344	11767	4.710
40	4.647	1428.301	524.2533	11073	4.788
41	4.074	1251.988	409.2895	9706	4.865
42	3.643	1120.121	339.8009	8683	5.046
43	3.356	1031.953	296.8335	8015	5.190
44	2.926	899.377	229.8947	6985	5.292
45	2.353	723.305	155.9912	5622	5.550
46	2.209	679.205	139.6610	5275	5.637
47	1.951	599.831	111.0354	4654	5.748
48	1.635	502.665	77.43111	3904	5.706

Table 5.2c: Friction Factor Measurements with $\beta_f = 0.0015$.

Exp. No.	$(Q_{rot.})_{corr.} \times 10^3$ (m ³ /s)	$Q_{duct} \times 10^4$ (m ³ /s)	Δp_s (Pa)	Re	f
49	3.213	2040.906	825.4634	15851	3.690
50	3.070	1949.809	768.1190	15143	3.762
51	2.639	1677.652	591.7057	13053	3.912
52	2.496	1586.493	540.5120	12344	3.996
53	2.353	1495.348	504.8664	11645	4.201

Table 5.2c: (Continued)

54	2.209	1403.278	447.9290	10938	4.230
55	2.066	1312.167	398.0053	10219	4.300
56	1.922	1221.067	356.3618	9509	4.446
57	1.635	1038.869	270.1327	8090	4.656
58	1.492	948.074	232.1514	7376	4.806
59	1.205	765.810	155.9596	5953	4.950
60	0.775	492.266	65.7439	3826	5.050

Table 5.3a: Friction Factor Measurements at $Re = 13446$.

Exp. No.	$(Q_{rot.})_{corr.} \times 10^3$ (m ³ /s)	Δp (Pa)	β_f	β_f^*	f
61	3.069	821.2305	0.001476	0.000381	3.873
62	3.786	877.0423	0.001821	0.000439	4.137
63	4.503	892.9885	0.002166	0.000516	4.212
64	5.221	916.9078	0.002511	0.000579	4.325
65	5.794	940.8272	0.002786	0.000629	4.438
66	6.368	956.7734	0.003062	0.000673	4.513
67	7.515	980.6927	0.003614	0.000782	4.626
68	8.376	1004.6120	0.004028	0.00085	4.738
69	8.663	1068.3970	0.004166	0.000827	5.039
70	9.523	1108.2630	0.00458	0.000877	5.227

Table 5.3b: Friction Factor Measurements at $Re = 10151$.

Exp. No.	$(Q_{rot.})_{corr.} \times 10^3$ (m^3/s)	Δp_s (Pa)	β_f	β_f^*	f
71	2.352	518.2523	0.001499	0.000347	4.289
72	2.639	526.2254	0.001681	0.000384	4.355
73	3.069	542.1716	0.001955	0.000446	4.487
74	3.786	558.1178	0.002412	0.000515	4.619
75	4.073	566.0909	0.002595	0.000553	4.685
76	4.647	574.064	0.00296	0.000621	4.751
77	5.507	597.9834	0.003508	0.000719	4.949
78	6.225	621.9027	0.003965	0.000764	5.147
79	6.655	637.8489	0.004239	0.000798	5.279
80	7.515	661.7683	0.004787	0.000883	5.477

Table 5.3c: Friction Factor Measurements at $Re = 5900$.

Exp. No.	$(Q_{rot.})_{corr.} \times 10^3$ (m^3/s)	Δp_s (Pa)	β_f	β_f^*	f
81	1.205	199.3278	0.001321	0.000268	4.884
82	1.492	207.3009	0.001635	0.000322	5.079
83	1.778	207.3009	0.00195	0.000383	5.079
84	2.209	215.274	0.002421	0.000452	5.275
85	2.496	215.274	0.002736	0.000507	5.275
86	3.069	223.2471	0.003364	0.000597	5.470
87	3.356	231.2202	0.003679	0.000648	5.666
88	3.786	239.1933	0.00415	0.000695	5.861
89	4.217	247.1665	0.004622	0.000758	6.056
90	4.647	263.1127	0.005093	0.000793	6.447

5.2.2.1 Friction Factor Measurement at Constant Blowing Factor

This part of experiment was taken at a constant blowing factor and a variable Reynolds number. The pressure drop across the tube bank was measured and plotted against Re as shown in Fig.5.6. It is obvious from Fig.5.6 that the pressure drop across the tube bank increases when a mass is added by the outgassing tubes.

Figure 5.7 gives the behavior of the friction factor as a function of Re with the blowing factor as a parameter, and shows the friction factor reduces with Reynolds number increase, while it increases as the blowing factor increases.

Figure 5.8 shows the comparison between the present work and **Debusschere-Ragland** work for different values of blowing factor and it can be concluded that the present work has a good agreement with **Debusschere-Ragland** work.

When the compressed air is blown through the pores of all tubes the over all friction factor increases by up to 50% as shown in Fig.5.9, where the increasing ratio varies from 10% to about 50% depending on the blowing rate. This increase in the friction factors with blowing is almost due to change in the boundary layer, affecting the shear stress distribution that causes an increase in the form drag around the cylinders.

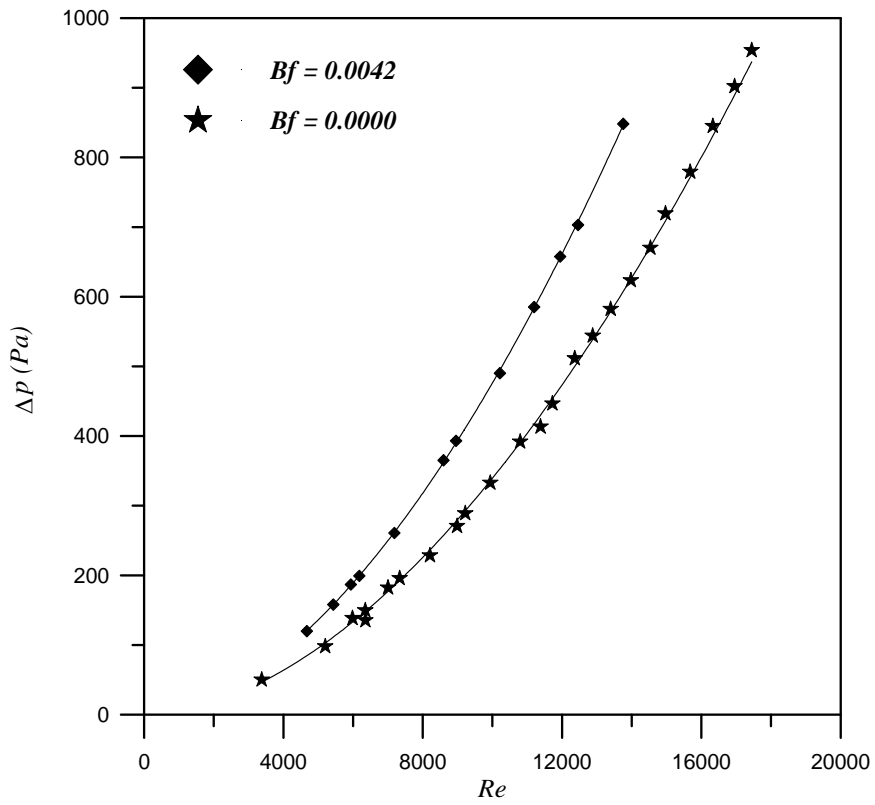


Fig. 5.6: Effect of the Re on the Pressure Drop.

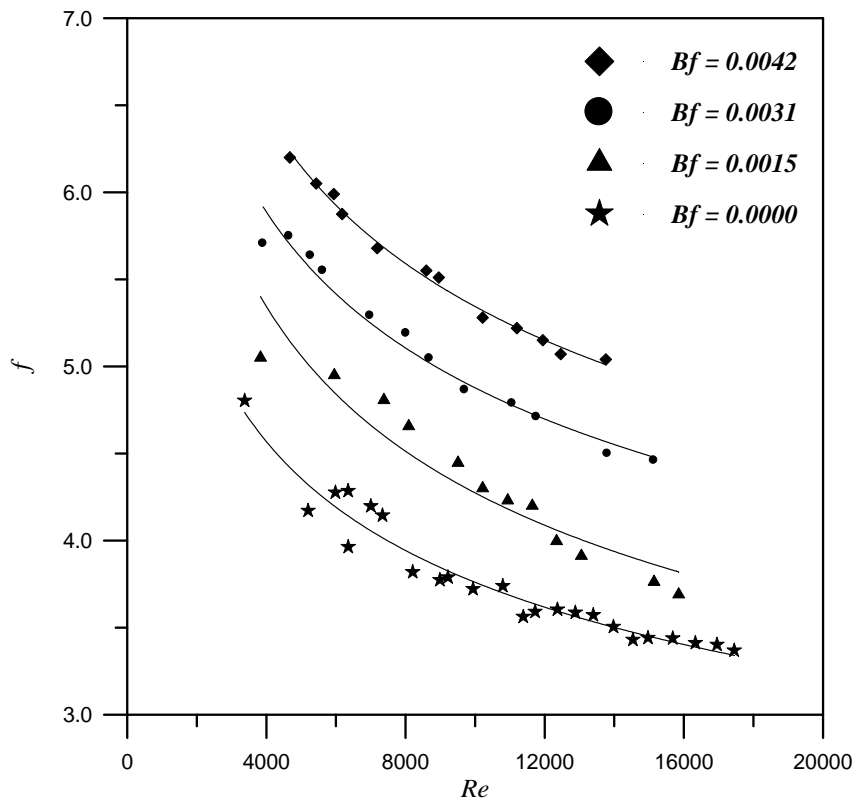


Fig. 5.7: Friction Factors in the Blowing Tube Bank as a Function of Re for Constant β_f .

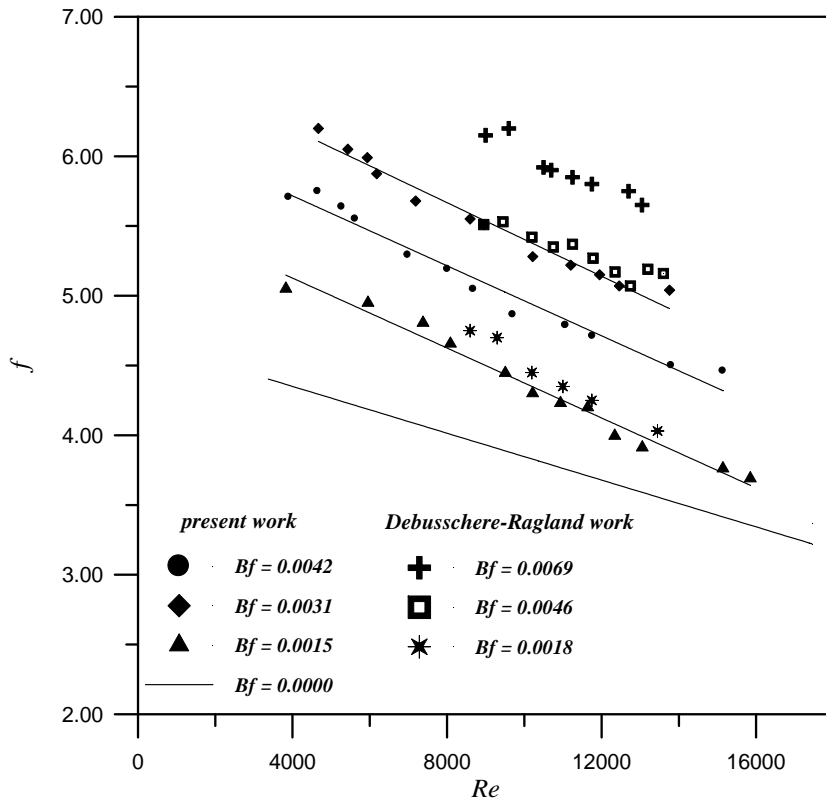


Fig. 5.8: Comparison the Data with Debusschere-Ragland Work with Different Blowing Factors.

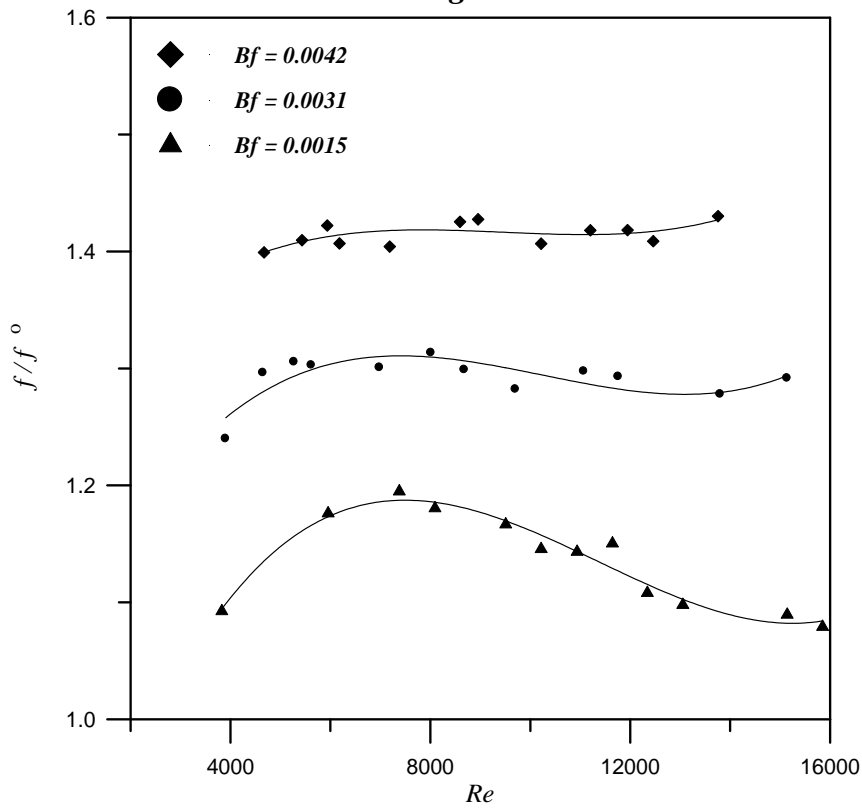


Fig. 5.9: f/f^0 for Different Values of Blowing Factors.

5.2.2.2 Friction Factor Measurement at Constant Reynolds Number

The friction factor measurement of the pressure drop across the tube bank with Re at constant blowing factor is shown in Fig.5.10, while Fig.5.11 gives the dependency of the friction factor on the blowing factor β_f for constant Re , and show how the friction factors reduce for the higher values of Reynolds number.

To extend the data in order to extend the investigation about the blowing effects on the friction factor measurement and to satisfy the obtained data with another definition of blowing factor given in [3], eq. 3.9:

$$\beta_f^* = \frac{\dot{m}/G_\infty}{f} \quad (3.9)$$

The relationship between the friction factor f and β_f^* is shown in Fig.5.12. The definition of β_f was more suitable for the present work results and gave more accurate results than that if the β_f^* definition was used for the blowing factor.

The difference obtained in the results between using the definitions of β_f and β_f^* is shown in Fig.5.11 and Fig.5.12. This is emphasized in Figs. 5.13 and 14 when f/f^o was plotted against β_f and β_f^* respectively, where

some scatter seems to appear in the data represented in Fig.5.14 where β_f^* definition for the blowing factor was used

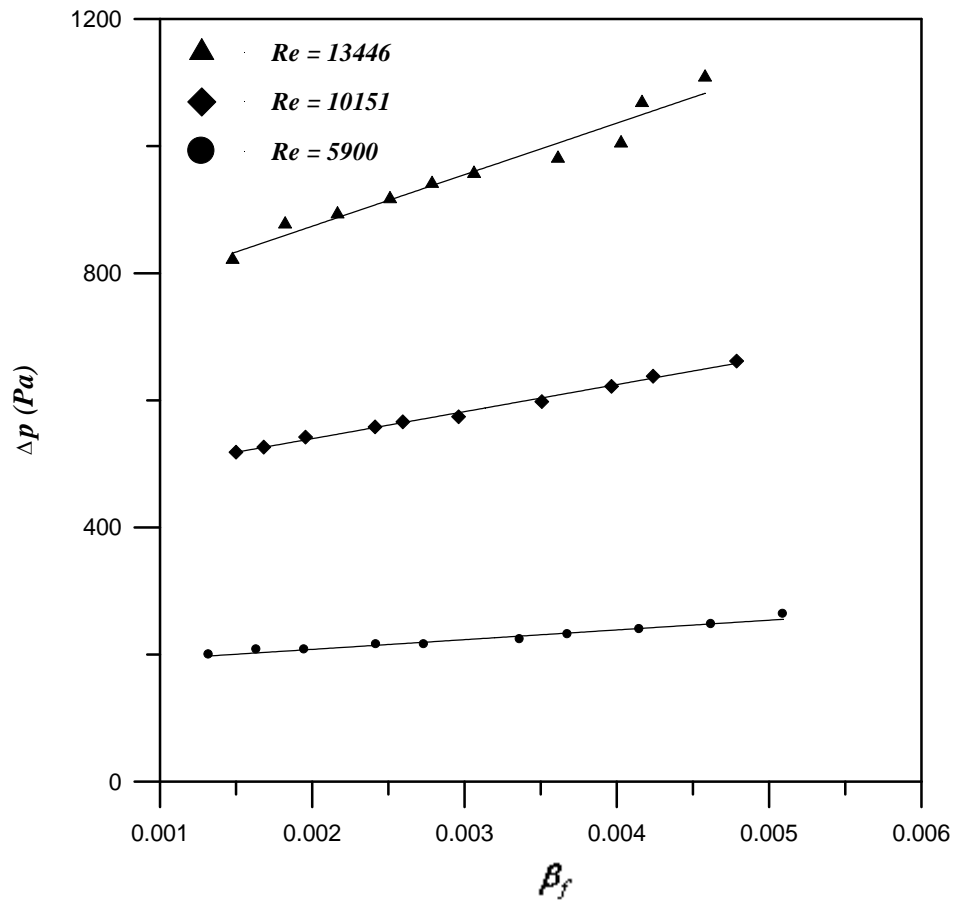


Fig.5.10: Pressure Drop Variation with the Blowing Factors.

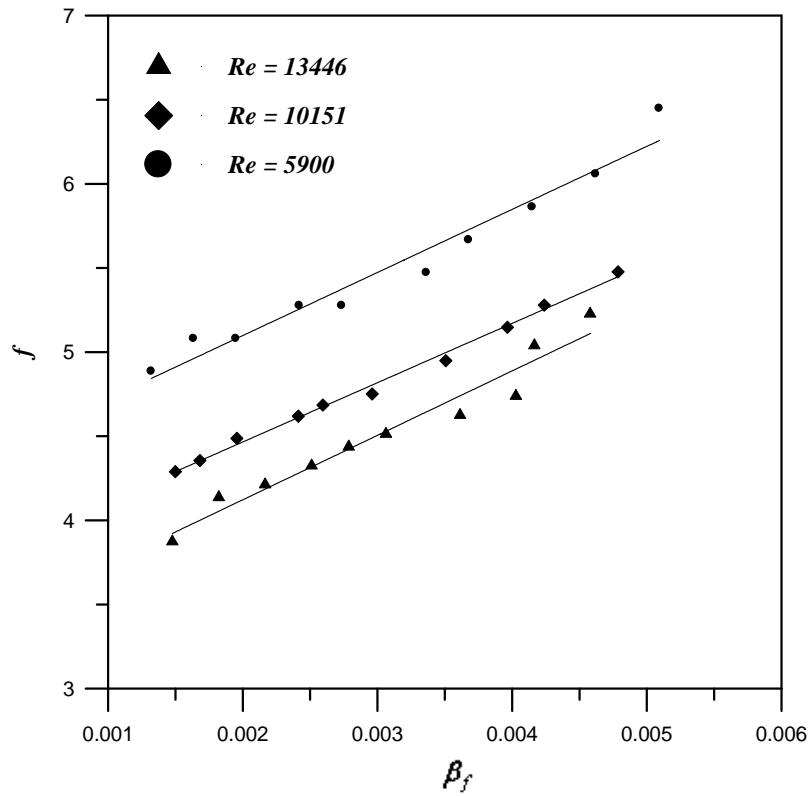


Fig.5.11: Friction Factors in the Blowing Tube Bank as a Function of β_f .

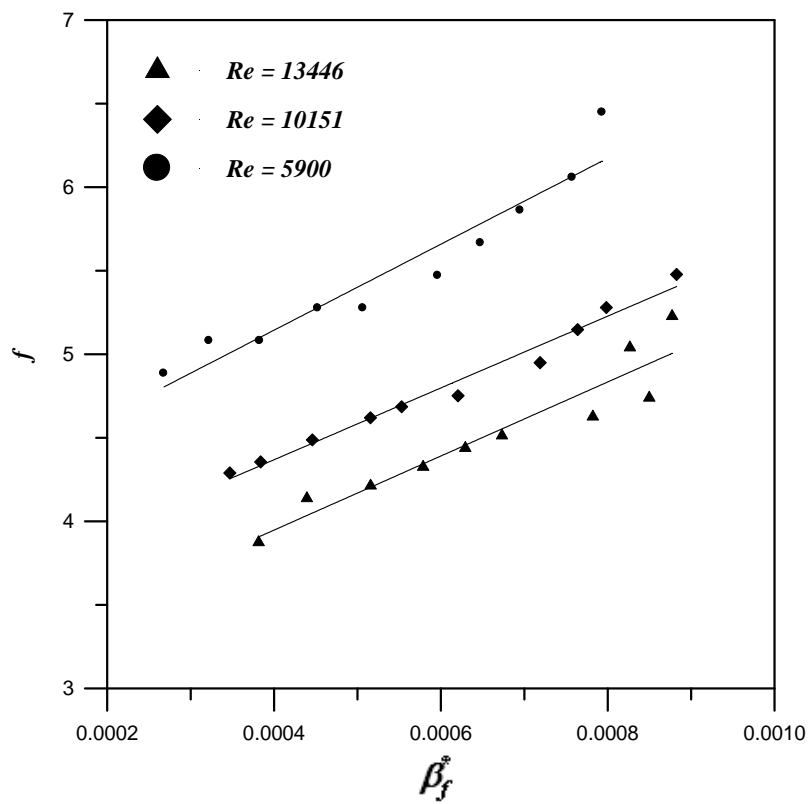


Fig.5.12: Friction Factors in the Blowing Tube Bank as a Function of β_f^* .

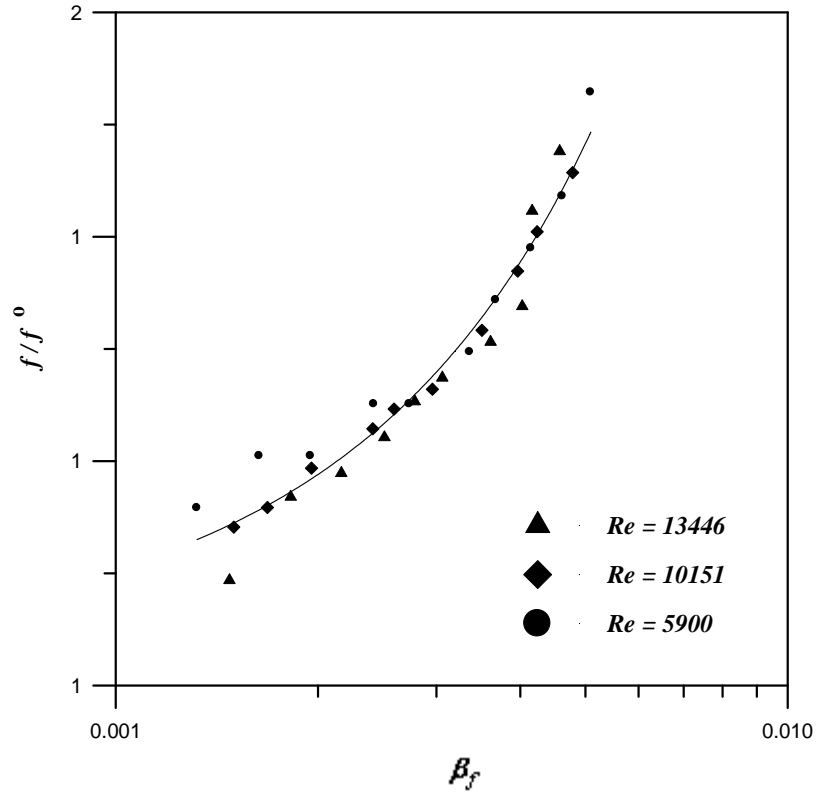
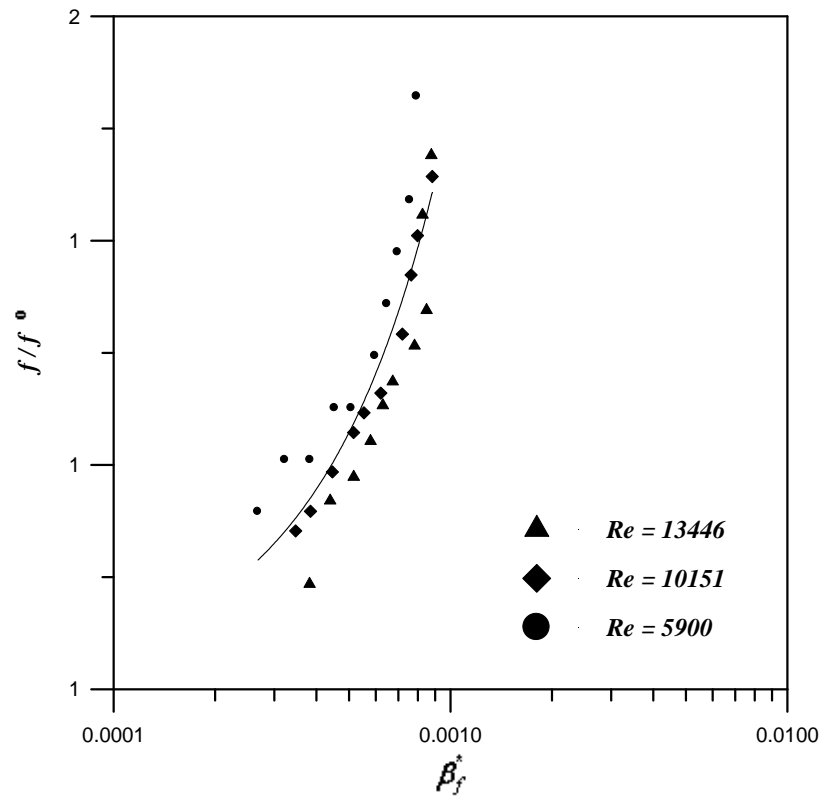


Fig.5.13: f/f^0 as a function of β_f .



*Fig 5.14: f/f^0 as a Function of β_f^**

5.3 Mass Transfer

This part of the present work is to represent the effect of the blowing on the mass transfer rate for a significant blowing rate and to get a correlation expressed in terms of many dimensionless groups.

The correlation developed from the mass transfer results can predict the mass transfer rate with blowing from the mass transfer data without blowing.

During the mass transfer measurements, the Reynolds number varied from 5000 to 16000 and the outgassing levels generated varies in the range $10^{-5} < \dot{m}/G_{\infty} < 10^{-3}$.

For the mass transfer data, several quantities were measured:

- The Δp from the Pitot probe measuring the main flow rate (mm of gas oil)
- The evaporated mass of water (g)
- The time taken for evaporating the mass of water (s)
- The relative humidity of the air before the test section ($^{\circ}\text{C}$)
- The temperature of the air before and after the test section, three readings log the y-axis of the duct ($^{\circ}\text{C}$)
- The surface temperature of the tube, three readings along the perimeter of the tube ($^{\circ}\text{C}$)
- The flow rate through the water rotameter
- The water heater temperature ($^{\circ}\text{C}$)

5.3.1 Mass Transfer Variables Measurements

From the mass transfer data, the variables of interest were calculated. The mass transfer coefficient h_m was calculated as:

$$h_m = \frac{\dot{m}}{B_m} \quad (3.15)$$

where \dot{m} is the mass flux averaged over the center tube surface, and B_m is the mass transfer driving forces and expressed as:

$$B_m = \frac{x_\infty - x_s}{x_\infty - 1} \quad (3.16)$$

The water vapor mass fraction at the surface tube wall (x_s) is obtained by assuming the average tube surface temperature, to be equal to the saturation temperature for the air-water mixture near the wall [11]. While the concentration in the bulk flow (x_∞) is obtained from the measured relative humidity, together with the air temperature.

The mass transfer data of the measured variables are given in Table 5.4, and the other mass transfer raw data are given in Appendix C.

5.3.2 Mass Transfer Results

5.3.2.1 *Mass Transfer Data Presentation*

The variables mentioned in the previous section are listed in Table 5.4 for different values of Re . By the variation of the water temperature inside the tube, the temperature of the equilibrium vapor pressure at the surface changed, giving a range of driving forces for evaporation by this way, different value of B_m are obtained.

Figure 5.15 shows a plot of the total evaporation flux, \dot{m} (kg/m²s) as a function of the tube surface temperature for different values of Reynolds number ($Re = 5414, 8322, 10186, 12530, 15778$). The surface temperature used is the average of the three temperatures measured along the perimeter in the middle of the tube. Fig.5.15 shows the evaporation rate directly proportional with the surface temperature for constant Re , and with Re for constant surface temperature. The evaporation rate does not depend on the surface temperature of the tube only, but rather on the difference in water vapor concentration between the surface and the bulk air flow, and that it was emphasized in Fig.5.16 by plotting the evaporation rate per unit tube surface versus mass transfer driving force B_m earlier defined:

$$B_m = \frac{x_\infty - x_s}{x_\infty - 1} \quad (3.16)$$

By introducing the parameter B_m , the influence of both the surface temperature (T_s) and the conditions of the bulk air are integrated in one variable, which makes the plot more general.

To account all the variables influencing the mass transfer rate using more general expressions the mass transfer coefficient ($h_m = \dot{m} / B_m$) versus the mass transfer driving force B_m as displayed in Fig.5.17.

The mass transfer coefficient (h_m) is in general a function of the system geometry, flow conditions (represented by Reynolds number and blowing factor), and the fluid properties (Sc), [50, 51]:

$$h_m = f(Re, Sc, \beta_m) \quad (5.3)$$

The dependency of the mass transfer coefficient on the blowing factor as a result of altering the flow pattern around the cylinder is caused by the outgassing.

The parameter β_m is the mass transfer blowing factor which expresses the amount of blowing in the boundary layer, as given by the expression [11, 3, 15]:

$$St_m Sc^{2/3} = \varphi(\beta_m) St^o Sc^{2/3}(Re) \quad (5.4)$$

Several definitions are possible for this blowing factor. More justifications for the blowing factor definitions will be given in the next sections when the actual form of the mass transfer correlations is determined.

Figures 5.15 to 5.19 represent all the relations between each of the interested variables with each others.

Table 5.4: Mass Transfer Results.

<i>Exp. No.</i>	<i>Re</i>	$\dot{m} \times 10^3$ (kg/m ² s)	<i>B_m</i>	$h_m \times 10^3$ (kg/m ² s)	<i>St Sc</i> ^{2/3}
1	8322	1.734	0.014	123.833	0.004798
2	8322	2.392	0.019	125.898	0.004877
3	8322	3.268	0.026	125.707	0.004891
4	8322	3.761	0.033	113.977	0.004432
5	8322	4.284	0.040	107.088	0.004162
6	8322	5.019	0.049	102.434	0.003981
7	8322	5.692	0.060	94.859	0.003685
8	8322	6.372	0.073	87.294	0.00339
9	8322	7.412	0.090	82.358	0.003205
10	10186	1.097	0.008	137.147	0.004359
11	10186	1.674	0.012	139.517	0.004431
12	10186	2.404	0.018	133.572	0.004238
13	10186	3.090	0.024	128.730	0.004087
14	10186	3.817	0.031	123.140	0.003908
15	10186	4.395	0.038	115.670	0.003668

Table 5.4: (Continued)

16	10186	5.377	0.047	114.396	0.003637
17	10186	6.432	0.056	114.851	0.003648
18	10186	6.859	0.068	100.874	0.003202
19	10186	8.145	0.084	96.962	0.003078
20	10186	9.067	0.098	92.518	0.002937
21	12530	1.096	0.007	156.553	0.004041
22	12530	1.803	0.012	150.288	0.003878
23	12530	2.674	0.017	157.291	0.004055
24	12530	3.41	0.022	155.013	0.003996
25	12530	4.466	0.029	153.999	0.00397
26	12530	4.977	0.036	138.243	0.003563
27	12530	5.818	0.044	132.232	0.003407
28	12530	6.525	0.053	123.11	0.003172
29	12530	7.129	0.064	111.396	0.002875
30	12530	8.411	0.077	109.24	0.002818
31	12530	9.375	0.086	109.017	0.002811
32	15778	1.186	0.0065	182.48	0.003737
33	15778	2.024	0.011	184.034	0.003768
34	15778	2.938	0.016	183.595	0.003759
35	15778	3.576	0.021	170.301	0.003485
36	15778	4.331	0.027	160.422	0.003287
37	15778	5.740	0.034	168.829	0.003459
38	15778	6.339	0.041	154.608	0.003167
39	15778	7.378	0.049	150.568	0.003082
40	15778	8.174	0.060	136.242	0.002797

Table 5.4: (Continued)

41	15778	8.936	0.073	122.412	0.002512
42	5414	1.218	0.011	110.759	0.006629
43	5414	1.665	0.016	104.042	0.006223
44	5414	2.196	0.022	99.815	0.005965
45	5414	2.767	0.029	95.413	0.005704
46	5414	3.307	0.037	89.381	0.005339
47	5414	4.002	0.046	86.990	0.005195
48	5414	4.418	0.056	78.892	0.004716
49	5414	5.428	0.068	79.830	0.004766
50	5414	6.342	0.085	74.616	0.004452
51	5414	6.423	0.108	59.472	0.003547
52	6892	8.025	0.130	61.728	0.002893
53	6892	1.626	0.014	116.135	0.005467
54	6892	3.289	0.034	96.731	0.004546
55	6892	4.497	0.043	104.579	0.004915
56	6892	6.692	0.078	85.799	0.004024
57	6892	7.395	0.096	77.032	0.003611
58	6892	8.225	0.120	68.542	0.003207
59	8641	2.416	0.019	127.173	0.004766
60	8641	3.605	0.032	112.648	0.004222
61	8641	5.276	0.051	103.450	0.003876
62	8641	8.534	0.089	95.891	0.003581
63	8641	9.148	0.110	83.168	0.003106
64	9563	1.754	0.013	134.903	0.004553

Table 5.4: (Continued)

65	9563	3.508	0.031	113.165	0.003826
66	9563	4.597	0.039	117.860	0.003985
67	9563	5.338	0.049	108.946	0.003683
68	9563	6.208	0.057	108.920	0.003681
69	10541	9.087	0.086	105.663	0.003239
70	10541	3.389	0.024	141.227	0.00433
71	10541	4.707	0.038	123.856	0.003796
72	10541	5.773	0.046	125.510	0.003846
73	10541	6.601	0.058	113.812	0.003488
74	10541	6.753	0.067	100.785	0.00309
75	11227	8.410	0.080	105.123	0.003024
76	11227	3.366	0.023	146.351	0.004216
77	11227	4.102	0.030	136.743	0.003933
78	11227	5.735	0.045	127.451	0.003677
79	11227	7.469	0.066	113.165	0.00325
80	11227	8.636	0.079	109.322	0.00314
81	11227	4.881	0.037	131.923	0.003813
82	14635	1.933	0.011	175.687	0.003891
83	14635	3.390	0.021	161.409	0.003574
84	14635	5.105	0.034	150.148	0.003324
85	14635	6.581	0.047	140.017	0.003096
86	14635	10.073	0.083	121.367	0.002682

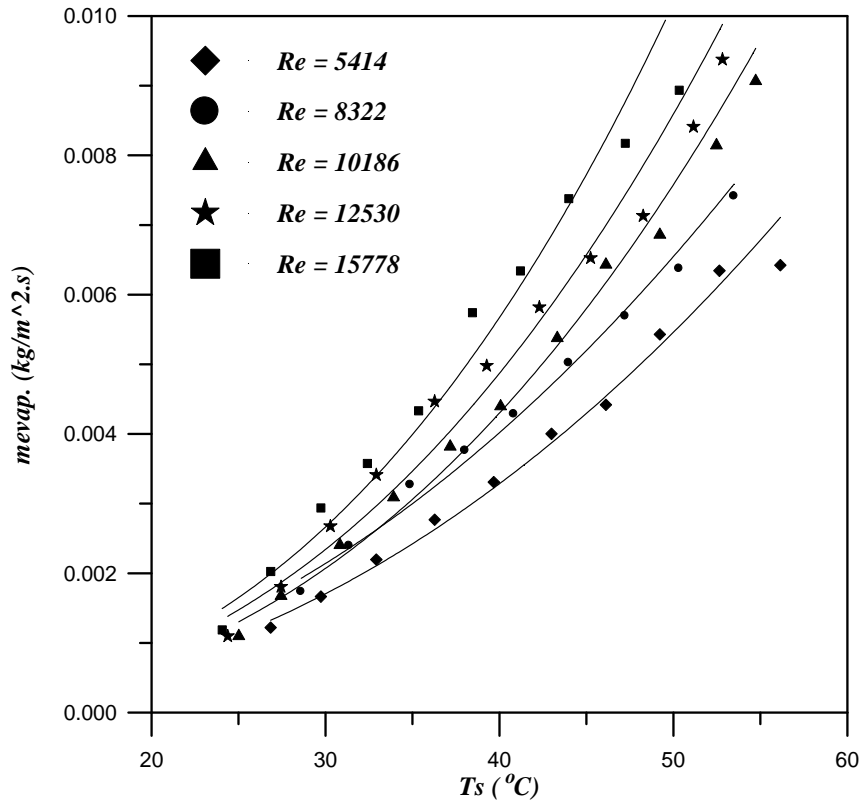


Fig.5.15: Evaporation Flux as a Function of Surface Temperature for Different Re .

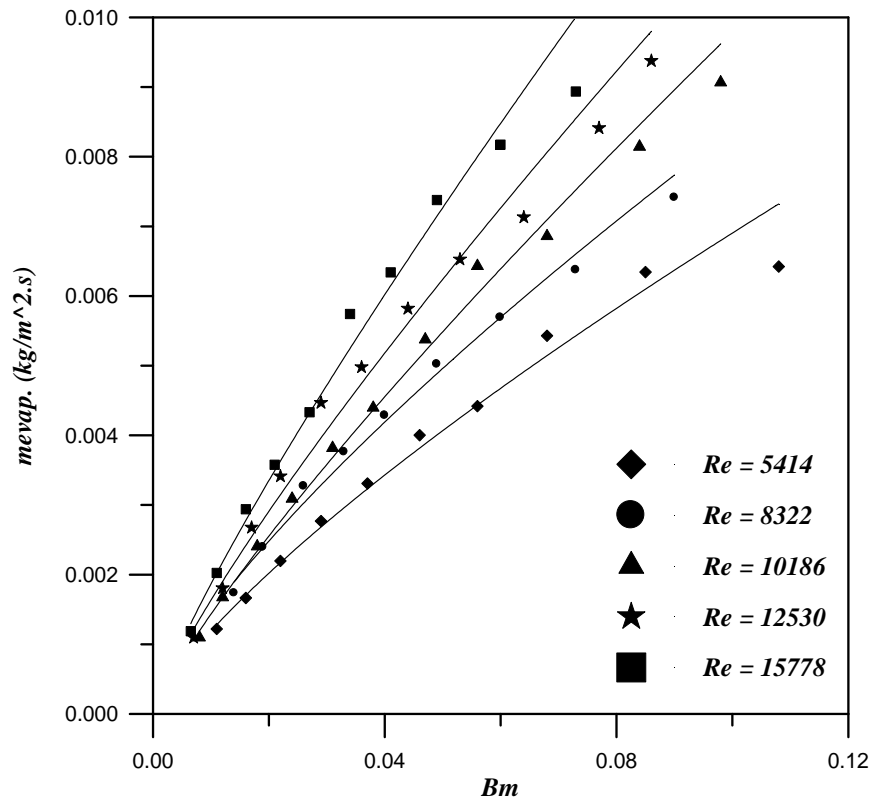


Fig.5.16: Evaporation Flux as Function of B_m for Different Re .

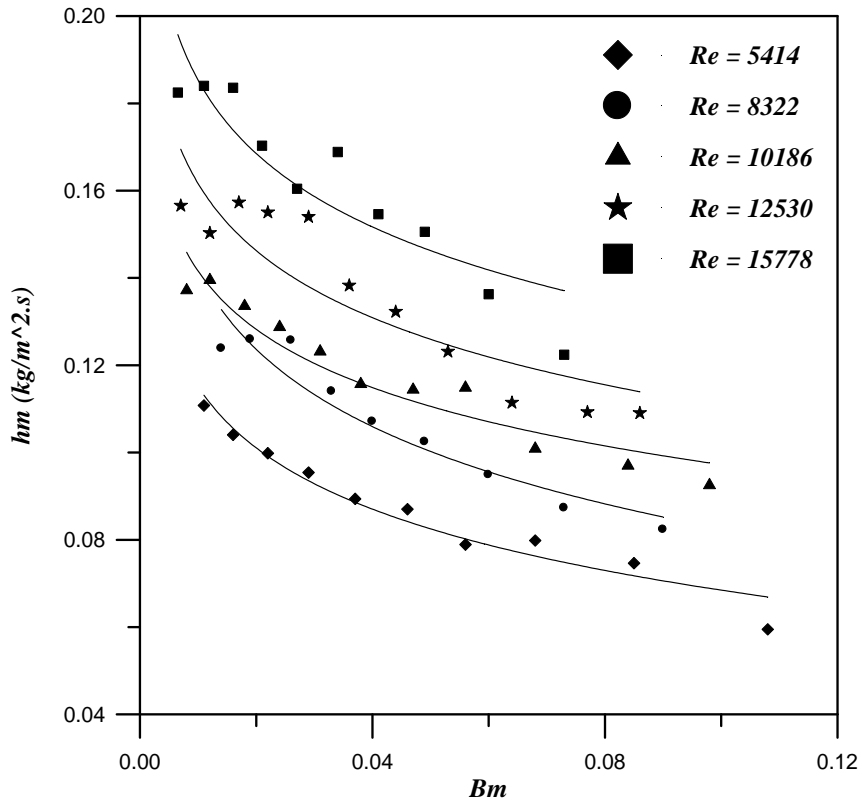


Fig.5.17: Mass Transfer Coefficient as a Function of B_m for Different Re .

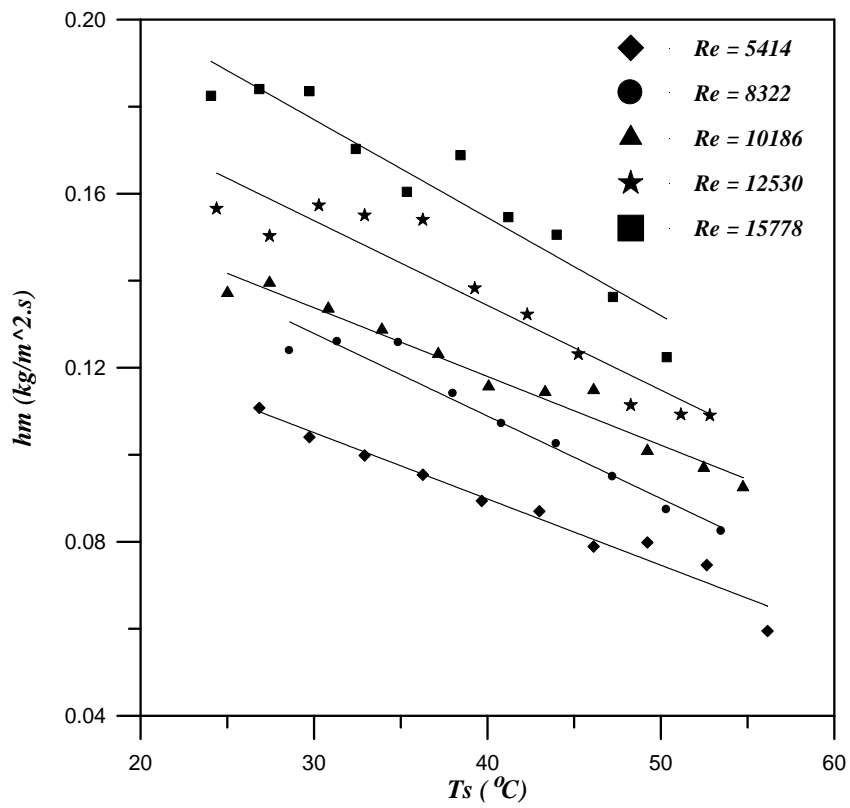


Fig.5.18: Mass Transfer Coefficient as a Function of Surface Temperature.

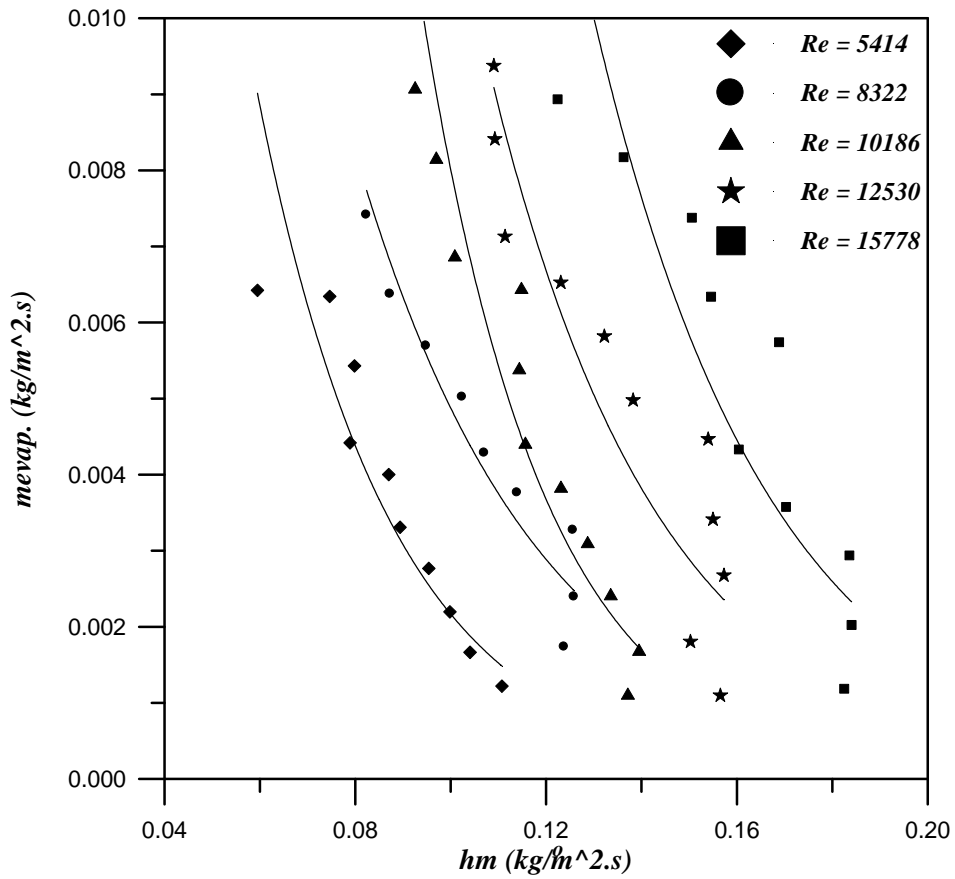


Fig.5.19: Evaporation Flux as a Function of h_m for Different Re .

5.3.2.2 Mass Transfer Correlations

This section describes the correlation of the data as a function of the influencing parameters Re , Sc and the blowing factor, β_m . To get correlations which are independent of the used units, the mass transfer coefficient h_m is non-dimensionalized into a mass transfer Stanton number (St_m) as given below:

$$St_m = \frac{h_m}{G} \tag{5.5}$$

This parameter exactly represents h_m by the dependence of the same variables. Because only one fluid was used in this study, it is not possible to examine the influence of the Schmidt number Sc , therefore, it is based on the **Chilton-Colburn** analogy, eq.5.4 is rewritten in the form:

$$St_m Sc^{2/3} = f(Re, \beta_m) \quad (5.6)$$

In the present work, the conducted experiments, the outgassing rate was set by the mass transfer rate; this implies that the mass transfer driving force contains an accurate expression for the amount of outgassing. The mass transfer driving force B_m is indeed a suitable definition to represent the blowing factor β_m as it was given in [3] and will be shown in the results analysis, therefore, the present work refers this fact to the data analysis, i.e.:

$$\beta_m = \frac{\dot{m}}{G_\infty} \frac{l}{St_m} = \frac{\dot{m}}{G_\infty} \frac{l}{h_m / G_\infty} = \frac{\dot{m}}{h_m} = B_m \quad (5.7)$$

By introducing the correction factor $\varphi(\beta_m)$ to account the influence of blowing as explained in the previous chapters, as given by:

$$\frac{St_m}{St_m^o} = \varphi(\beta_m) \quad (2.14)$$

The parameter St_m^o is the Stanton number for the case of negligible outgassing and it is a function of Re and system geometry only, that would be observed in a set-up with the same geometry and under the same conditions.

The direct measurement of St_m^o with the present set-up was difficult because of the loss of accuracy at very low evaporation rates. Therefore, it was assumed that for the range of Reynolds numbers used, St_m^o could be correlated as given by eq.3.18:

$$St_m^o Sc^{2/3} = a Re^b \quad (3.18)$$

The above form of eq.3.18 is frequently used for the correlation of heat and mass transfer data in geometries ranging from flat plates to single cylinders or tube banks in cross flow. The values for the parameter b range from about -0.4 to -0.54 ([3], [49], [52], as cited in [11]. The influence of outgassing can be accounted for by multiplying the mass transfer coefficients for the case of negligible blowing by a function $\varphi(\beta_m)$ of the mass transfer blowing factor β_m as given:

$$St_m Sc^{2/3} = \varphi(\beta_m) \times a Re^b \quad (5.8)$$

To fit the data to the above form, a formula $\varphi(\beta_m)$ must be chosen. Two forms were found in literature, the first one given by **Kays and Crawford** [3] for a flat plate given as:

$$\frac{St_m}{St_m^o} = \frac{\ln(1 + \beta_m)}{\beta_m} \quad (5.9)$$

This equation is indeterminate for $\beta_m = 0$, but

$$\lim_{\beta_m \rightarrow 0} \frac{\ln(1 + \beta_m)}{\beta_m} = 1.0 \quad (5.10)$$

The second form proposed by **Spalding and Evans** [15] for a specific geometry, which is more accurate than **Kays and Crawford** formula given as:

$$\frac{St_m}{St_m^o} = \frac{1}{(1 + \beta_m)^c} \quad (5.11)$$

This form contains only one parameter c and satisfies the condition $\varphi(0)=1$.

For the present work the two forms of the correction factors were examined. Correction function given by eq. 5.11 is more accurate than **Kays and Crawford** as recommended in [11]. Also correction function given by **Kays and Crawford** (eq. 5.9) was used to show how much the flat plate correction hold to cylinder.

In order to obtain more accurate results, eq.5.11 was modified by multiplying the left hand side by the density ratio $\left(\frac{\rho_\infty}{\rho_s}\right)^n$ to account the non-uniform properties within the boundary layer as recommended in [3], Thus eq. 5.11 become:

$$\frac{St_m \left(\frac{\rho_\infty}{\rho_s}\right)^n}{St_m^o} = \frac{1}{(1 + \beta_m)^c} \quad (5.12)$$

Substitute eq. 5.8 into 5.12, the overall model 1 becomes:

$$St_m Sc^{2/3} = \frac{a Re^b}{(1 + \beta_m)^c} \left(\frac{\rho_s}{\rho_\infty} \right)^n \quad (5.13)$$

The values for the parameter n range from 0.4 to 0.66 [3, 51], therefore, for the present work it was chosen to be equal to 0.4. The three parameters (a , b , c) in eq.5.13 were determined by fitting the curve to the data points using a least squares minimization method by a *STATISTICA* software version 5.0. This gave the following values for the parameters with the corresponding uncertainty intervals:

$$a = 0.51 \pm 0.02$$

$$b = -0.50 \pm 0.02$$

$$c = 4.7 \pm 0.3$$

The Schmidt number was assumed to be 0.6, which is the value for the diffusion of water vapor into air in the limit of a very dilute mixture. Fig.5.20, 21 and 5.22 show how the model fits the data. Fig.5.20 compares $\varphi(\beta_m)$ against the data points normalized as:

$$\frac{St_m Sc^{2/3}}{a Re^b}$$

where St_m is obtained from the measurements. Fig.5.21 shows a good agreement between model 1 and the data points dividing by $a Re^b$, where the coefficient of determination $R^2 = 0.933$. Fig.5.22 compares $St_m^o Sc^{2/3} = a Re^b$ against the measured values $St_m Sc^{2/3} / \varphi(\beta_m)$, with $R^2 = 0.950$.

The same procedure was followed for the application of the equation of **Kays and Crawford** given for flat plate. When the correction function of **Kays and Crawford** (eq.5.9) directly applied, the results obtained were not accurate; therefore, it required a modification to be applicable for cylinders by raising it to power m to get:

$$\frac{St_m}{St_m^o} = \left(\frac{\ln(1 + \beta_m)}{\beta_m} \right)^m \quad (5.14)$$

This form contains only one parameter m . Substitute eq.5.8 into eq.5.14 then the overall model 2 becomes:

$$St_m Sc^{2/3} = a Re^b \left(\frac{\ln(1 + \beta_m)}{\beta_m} \right)^m \quad (5.15)$$

The three parameters were determined and given:

$$a = 0.5 \pm 0.02$$

$$b = -0.5 \pm 0.04$$

$$m = 9.94 \pm 0.5$$

The results obtained for this model show that the correction $\varphi(\beta_m)$ for the flat plate is the same as for the cylinders ordered to power about 10. This will give an idea about the reduction in mass transfer coefficient for the cylinder is higher than the reduction in the flat plate geometry powered to 10 for the same blowing rate. Figure 5.23 and 24 show the data points fit for model 2 and their coefficient of determinations are: $R^2 = 0.920, 0.941$ respectively.

The Figures of the two models show a good agreement between the modified equations for model 1 and model 2 with the data points. Moreover there is no Reynolds number dependency left in the data after dividing by aRe^b , and similarly $St^o Sc^{2/3}$ is independent of the blowing factor after dividing $St_m Sc^{2/3}/\varphi(\beta_m)$.

Figures 5.21, 22 show a significant decrease in the surface transport coefficients due to the outgassing. Reductions up to 80 % (depending on the outgassing rate) have been measured, which affects the design of heat or mass transfer processes involving high outgassing rates. The correction function $\varphi(\beta_m)$ is to account for the effect of outgassing. When the transport coefficients for the non-blowing case are known, the ones for the outgassing case can be obtained through multiplication by the correction function $\varphi(\beta_m)$.

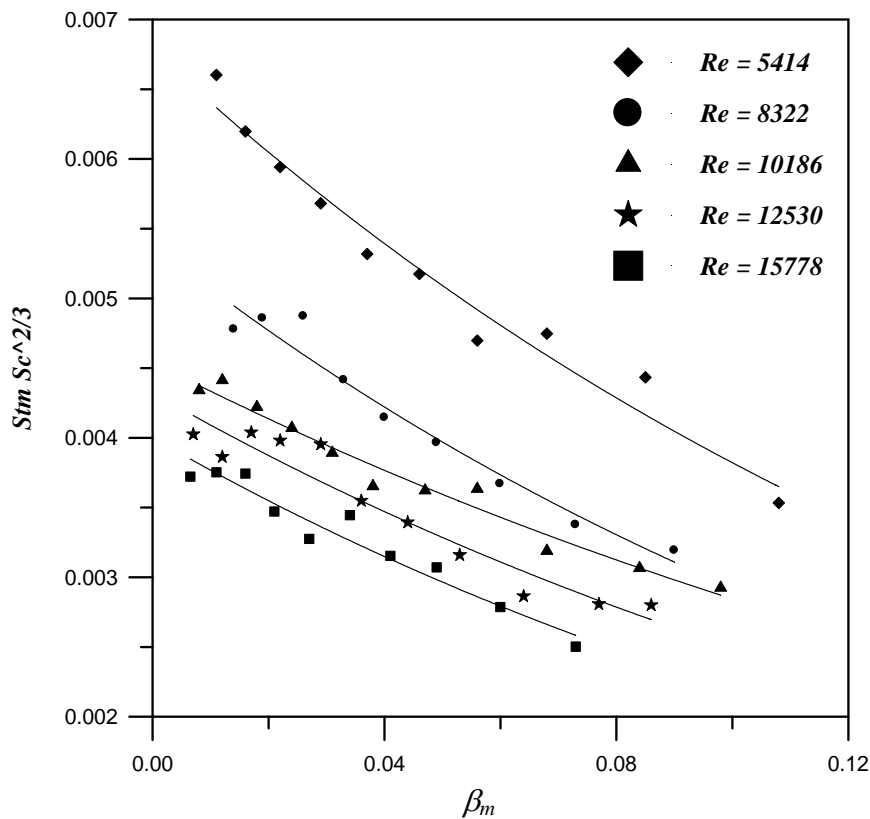


Fig.5.20: $St_m Sc^{2/3}$ as a Function of Blowing Factor for Different Re .

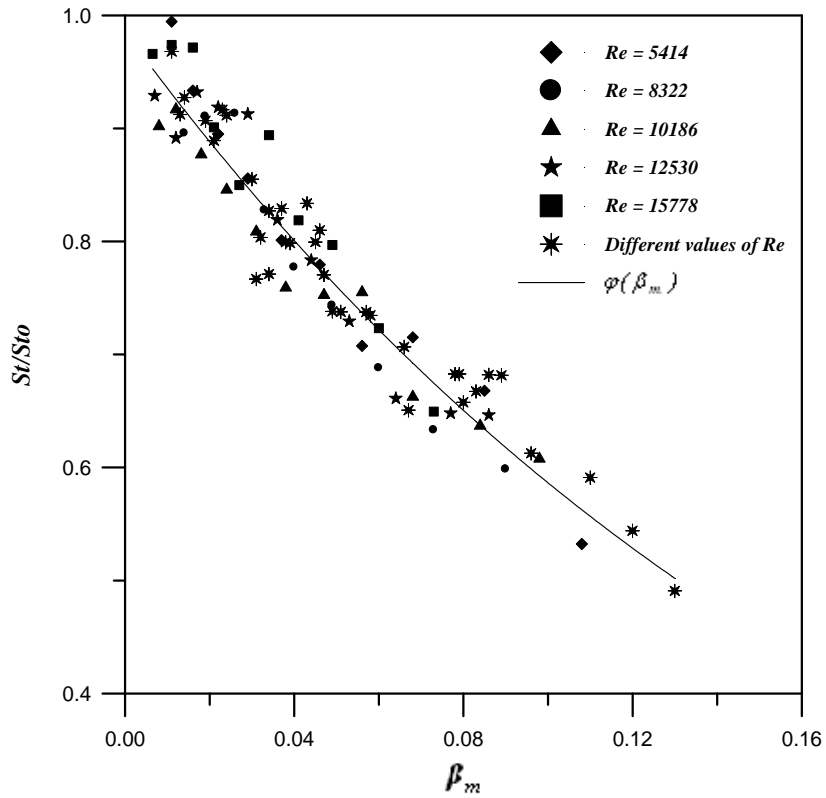


Fig.5.21: Comparison of the Correction Factor of Model 1 to the Data Points.

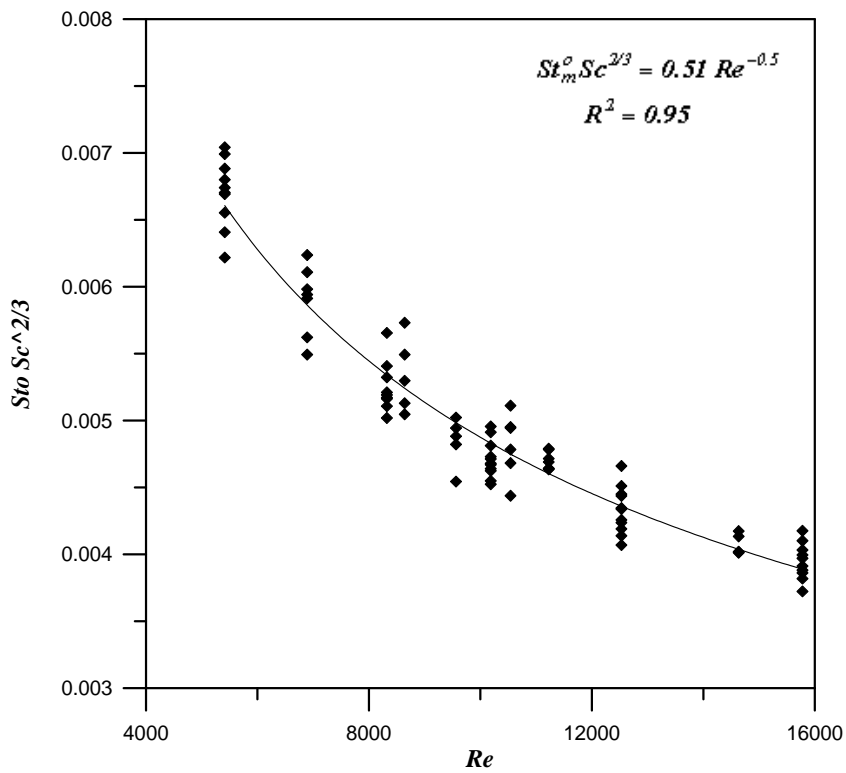


Fig.5.22: $St_m^0 \cdot Sc^{2/3}$ as a Function of Re of Model 1.

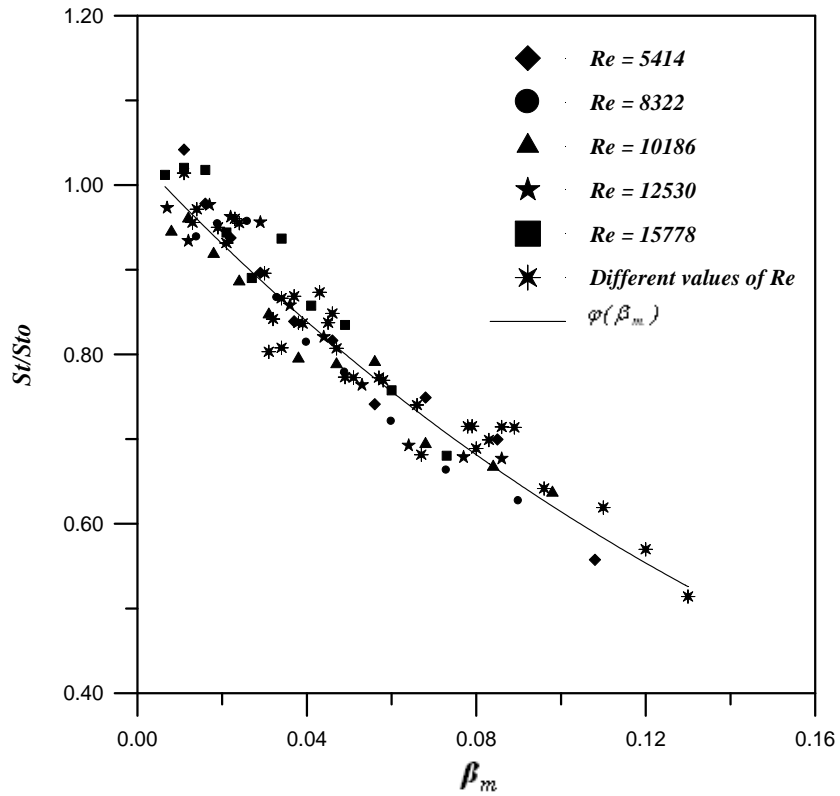


Fig.5.23: Comparison of the Correction Factor of Model 2 to the Data Points.

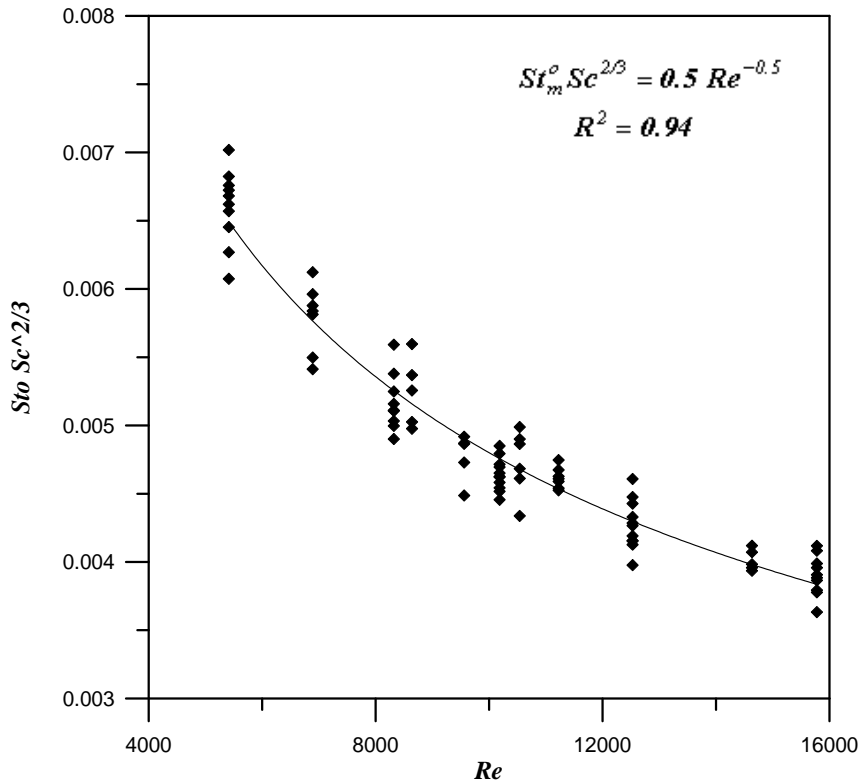


Fig.5.24: $St_m^o Sc^{2/3}$ as a Function of Re of Model 2.

5.3.2.3 Comparison with Literature

For both models (1& 2), the present work depended the mass transfer driving force to represent the mass transfer blowing factor, and both the correction function given by **Kays and Crawford** and **Spalding and Evans** were examined with some modifications as explained in the previous section. The two proposed models are successful and gave good accuracy for the experimental data. While **Debusschere and Ragland** [11] worked on the same geometry that was chosen for the present work and they modified the blowing factor definition by multiplying it with the density ratio between air water vapor. Including this density ratio in the blowing factor gives better representation for the physics of the boundary layer with non-uniform properties, which can be seen by expanding eq. 3.31 as given below:

$$\beta_m = \frac{\dot{m} \rho_a}{G \rho_w St_m} = \frac{v_o \rho_a (X_o - X_\infty)}{-\rho D \frac{\partial x}{\partial y} \Big|_o} = \frac{\text{convective transport}}{\text{molecular diffusion}} \quad (3.31)$$

The above equation makes the blowing factors get bigger. **Debusschere and Ragland** also used the model proposed by **Spalding and Evans** for the correction function definition (eq. 5.11). The results of **Debusschere and Ragland** are given in Figs.5.25 and 26 with the coefficient of determination $R^2 = 0.89$.

Figure 5.27 and 28 gives the **Debusschere-Ragland** data point fits to the proposed model 1 and respectively with good accuracy. This indicates that the suggested models of the present work more accurate than **Debusschere-Ragland** model.

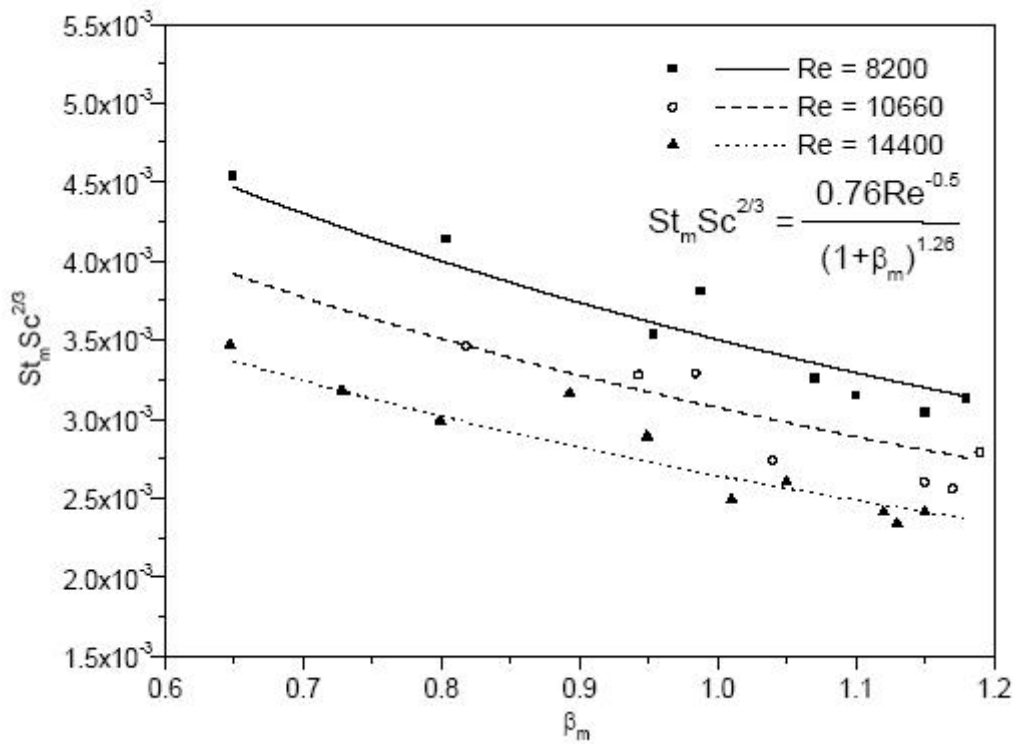


Fig.5.25: $St_m Sc^{2/3}$ as a Function of β_m for Different Re [11].

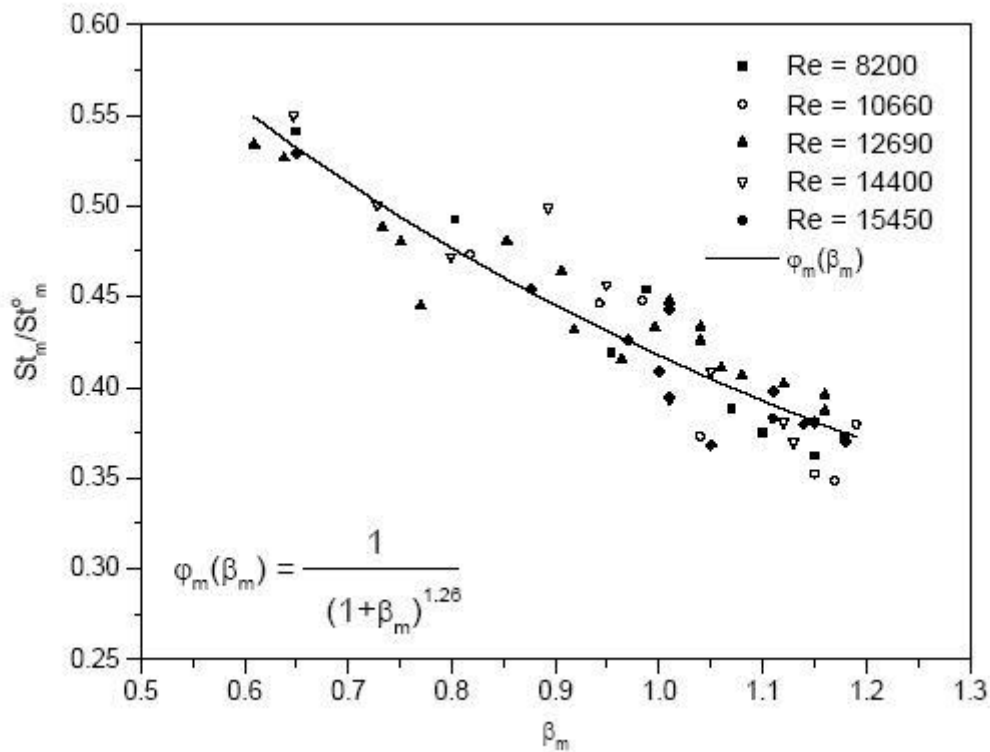


Fig.5.26: Comparison of the Correction Factor to the Data Points[11].

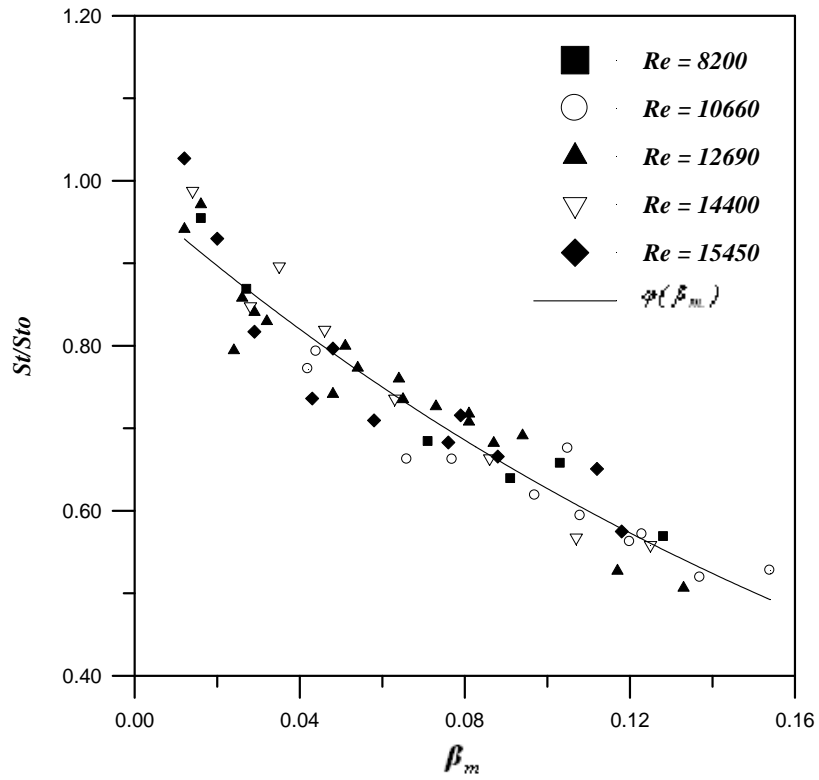


Fig.5.27: Comparison of the Correction Factor to the Debusschere-Ragland Data Points for Model 1.

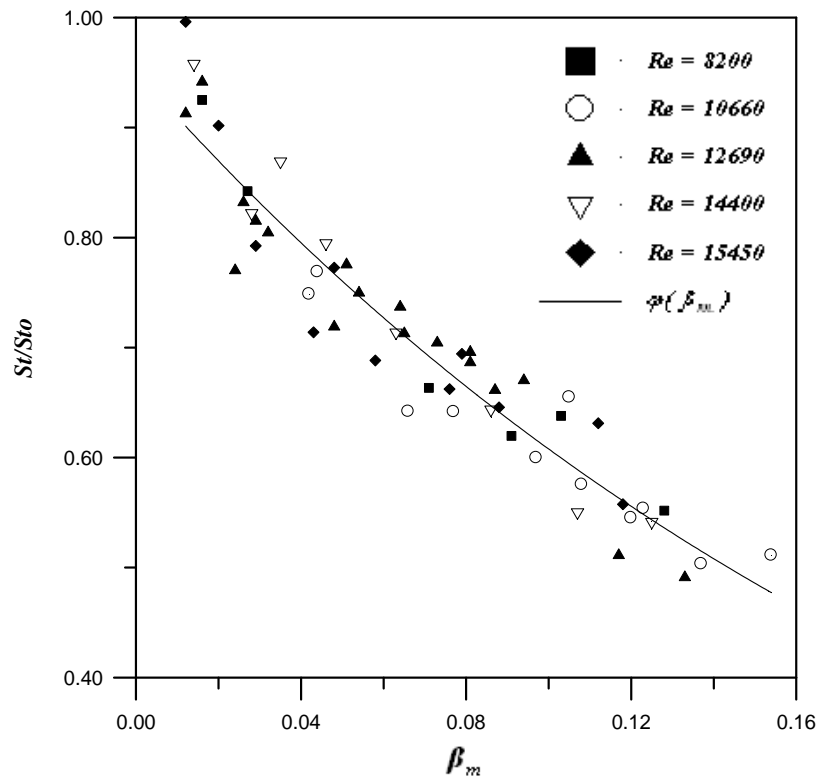


Fig.5.28: Comparison of the Correction Factor to the Debusschere-Ragland Data Points for Model 2.

5.3.2.4 Error Analysis

Fig.5.29 shows the residual between the data and the fitted model (model 1) as a function of β_m , while Fig.5.30 shows this error distribution as a function of Re .

Fig.5.29 shows that the residual randomly distributed along β_m and the error in β_m evaluation was indeed from the surface tube temperature measurement. Fig. 5.30 shows the residual slightly higher at low values of Re as discussed in friction factor part.

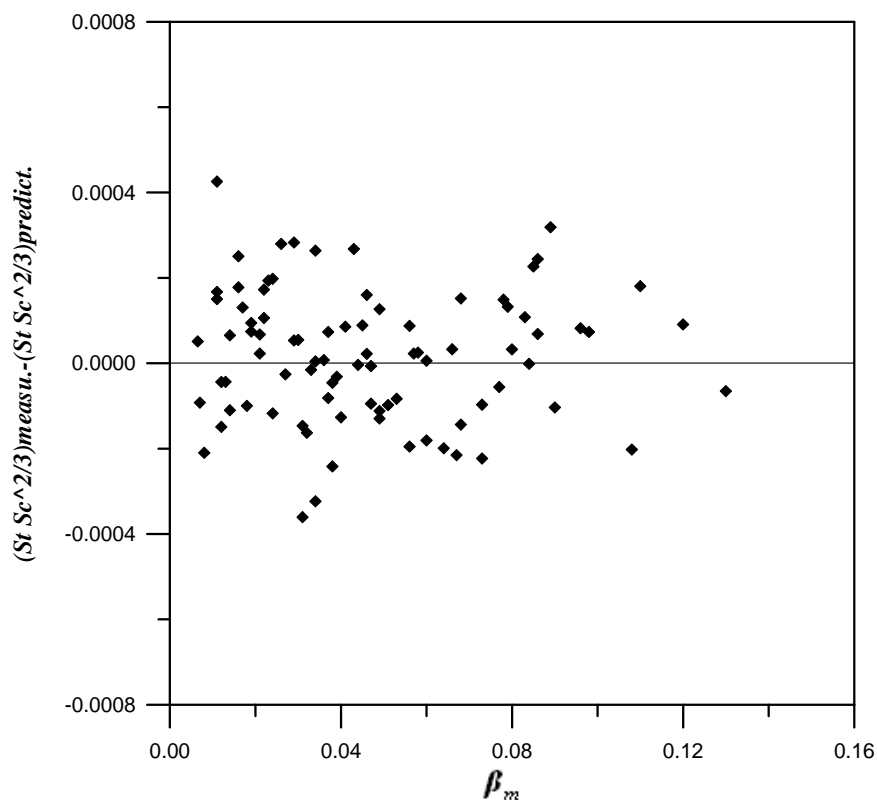


Fig.5.29: The Residual as a Function of the Blowing Factor.

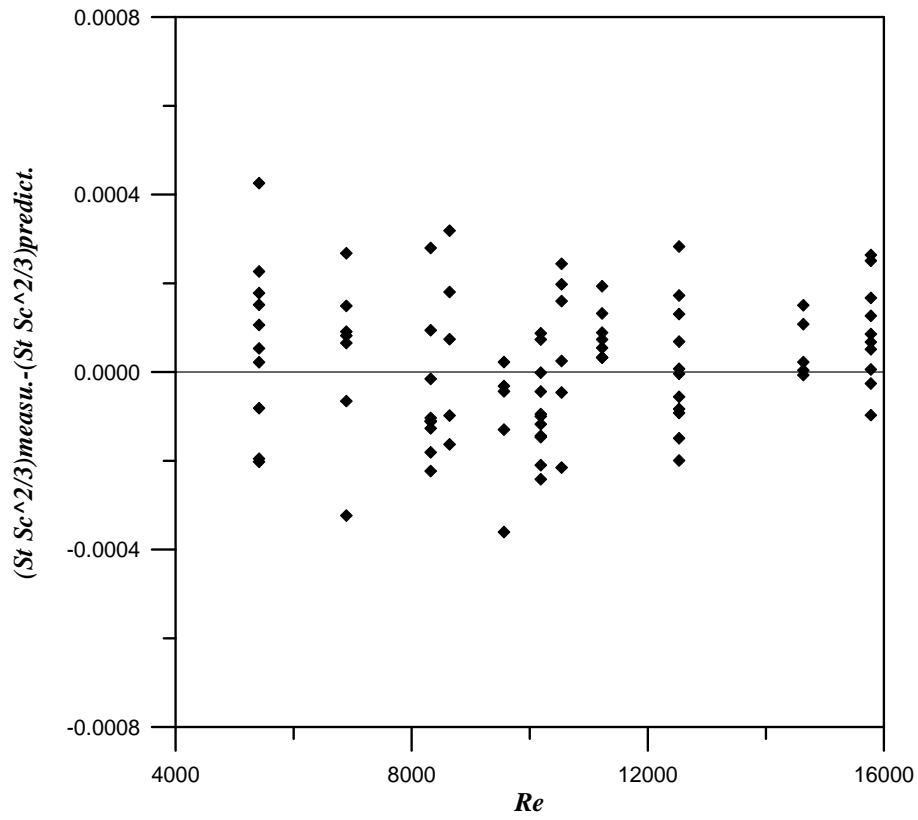


Fig.5.30: The Residual as a Function of Re .

CHAPTER SIX

Conclusions and Recommendations

6.1 Conclusions

1. The friction factors in an outgassing tube increase with outgassing rate. This is probably due to the effect of blowing on the form drag. The friction factor increased from 10-50% depending on the blowing rate.
2. The analogy as described by **Kays and Crawford** for flat plate will not hold for the tube bank geometry. It appears that the analogy only valid for skin friction. In a tube bank, the major pressure drop is due to form drag, caused by the separation of the boundary layer as explained in chapter two. This might explain why an increase in friction factors was observed, while **Kays and Crawford** predicts a decrease in friction factor for the blowing case.
3. The mass transfer driving force is the best expression for the mass transfer blowing factor for the cylinders.

4. The mass transfer coefficient for the outgassing case can be accounted from the non-outgassing mass transfer coefficient by multiplying the last one with the correction functions (φ).
5. The mass transfer coefficient was reduced up to 80% due to the outgassing, this is may be due to the thickening of the boundary layer caused by blowing.
6. The reduction in mass transfer coefficient for cylinders is much higher than for the flat plate by force 10. This is due to the separation in the boundary layer in cylinders.

6.1 Recommendations

For those who would carry future studies on related subject, the following recommendations may be considered:

1. Studying outgassing effects on heat transfer and make an analogy with mass transfer.
2. From the experimental work, a lot of information could be obtained to get a mathematical model to account the outgassing theories.
3. Study Schmidt number effect by using different fluids (e.g. by heating the air instead of water).

4. The use of electronic pressure transducers will be very helpful for the measurement of the very low pressure signals from the Pitot probe. This might make possible to get accurate results at very low flow rates to get more accurate correlations for the Reynolds number dependency of the transport coefficients.

5. Study the flow pattern around the cylinders by Laser Doppler Velocimetry analysis inside the tube bundle. The tube with the pressure taps along its perimeter could be inserted at various positions in the tube bundle

References

1. Bryden, K. M., Ragland, K. W. and Ostlie, L. D., Modeling the Performance of the Whole Tree Energy Combustor, Proceedings of the Sixth National Bioenergy Conference, 139-146, Nevada, 1994.
2. Bryden, K. M. and Ragland, K. W., Combustion of a Single Log Under Furnace Conditions. In Developments in Thermochemical Biomass Conversion, ed. A. V. Bridgwater and D.B. G. Bvock, Blackbie Academic and Professional Press, London, 1331-1345, 1997.
3. Kays, W. M. and Crawford, M. E., Convective Heat and Mass Transfer, 3rd Edition, McGraw-Hill, Inc., New York, 1993.
4. Basic Duct Hydraulics, at the site:
<http://ateam.lbl.gov/Design-guide/DGHtml/basicducthydraulics.htm>
5. White, F. M., Fluid Mechanics, 3rd Edition, McGraw-Hill, Inc., New York, 1994.
6. Boundary Layer Theory, Fluid Mechanics, at the site:
<http://www.freestudy.co.uk/fluid%20mechanics/t3203.pdf#search='fluid%20mechanics%20boundary%20layer%20theory'>
7. Flow analysis, at the site:
<http://www.engr.mun.ca/~yuri/Courses/MechanicalSystems/FlowAnalysis.pdf#search='equation%20for%20pipes%20and%20ducts%20flow'>
8. Holman, J. P., Heat Transfer, Eight Edition, McGraw-Hill, Inc., United States of America, 1990.
9. Brodkey, R., S. and Hershey, H., C., Transport Phenomena, 2nd Printing, McGraw-Hill, Inc., New York, 1989.
10. White, F. M., Viscous Fluid Flow, 2nd Edition, McGraw-Hill, Inc., New York, 1991.
11. Debusschere, B., and Ragland K., W., Measurement of Friction, Heat Transfer, and Mass Transfer in a Severely Outgassing Tube Bank, Int. J. Heat and Mass Transfer, 41(9), 3015-3024, 1998.
12. Mickley, H. A., Ross, R. C., Squires, A. L., and Stewart, A. A., "Heat, Mass and Momentum Transfer for Flow over a Flat Plate With Blowing or Suction," NACA TN 3208, 1954. [Cited in 35].
13. Simpson, R.L., Moffat, R. J., and Kays, W. M., "The Turbulent Boundary Layer on a Porous Plate: Experimental Skin Friction with Variable Injection and Suction", Int. J. Heat and Mass Transfer, 12, 771-789, 1969.
14. Julien, H. L., Kays, W. M., and Moffat, R. J., "Experimental Hydrodynamics of the Accelerated Turbulent Boundary Layer With

- and Without Mass Injection,” *Journal of Heat Transfer*, 93, 373-379, 1972. [Cited in 35].
15. Spalding, D. B. & Evans, H. L., Mass Transfer through Laminar Boundary Layers-3. Similar Solutions of the b-equation, *Int. J. Heat Mass Transfer* 2, 314-341, 1961.
 16. Lessner, P. and Newman, J, Hydrodynamics and mass transfer in a porous-wall channel, *J. Electrochem. Soc. ; Vol/Issue: 131:8*, 1984.
 17. Hirata, Y., Sakata, K. and Wada, H., Turbulence Transport Phenomena of Air Flow in a porous Tube with Injected Carbon Dioxide, *Heat Transfer-Japanese Research*, Vol/Issue:19:5, 1990.
 18. Mustafa, A., A., Study of Flow through a Porous Tubes, M. Sc. Thesis, Baghdad University, 1991.
 19. Danny, P., H., Experimental Study of Characteristics of Micro-Hole Porous Skins for Turbulent Skin Friction Reduction, ICAS Congress, 2101.1-2101.7, 2002.
 20. Inger, G.R. and Babinsky, H., Viscous Compressible Flow across a Hole in a Plate, *AIAA Journal of Aircraft*, 37(6), 1028-1032, 2000.
 21. Galluzzo, P.M., Babinsky, H. and Inger, G., "Viscous Compressible Flow through a Hole in a Plate, Including Entry Effects", *AIAA Journal of Aircraft*, 39(3), 516-518, 2002. At the site:
www2.eng.cam.ac.uk
 22. Galluzzo, P.M., Babinsky, H., Transpiration Flow through a Porous Plate, in the Absence of a Tangential Stream. At the site:
<http://www2.eng.cam.ac.uk/~pmg26/hpage/static.html>
 23. Bohning, R. and Doerffer, P., Effects of Tangential Stream on Porous Plate Transpiration, at the site:
<http://www2.eng.cam.ac.uk/~pmg26/hpage/bohndoerf.htm>
 24. Piomelli, U., Moin, P., and Ferziger, J., “Large Eddy Simulation of Flow in a Transpired Channel”, *Journal of Thermophysics*, 5(1), 124-128, 1991. [Cited in 45].
 25. Sumitani, Y., and Kasagi, N., “Direct Numerical Simulation of Turbulent Transport with Uniform Wall Injection and Suction”, *AIAA Journal*, 33(7), 1220-1228, 1995. [Cited in 35].
 26. Taylor, G. I., “Fluid Flow Regions Bounded by Porous Surfaces”, *Proceedings of the Royal Society of London, Series 234A*, Vol. 11199, 456-475, 1956. [Cited in 45].
 27. Culick, F. E. C., “Rotational Axisymmetric Mean Flow and Damping of Acoustic Waves in Solid Propellant Rocket Motors”, *AIAA Journal*, 4, 1462-1464, 1966.
 28. Beddini, R. A., “Injection Induced Flows in Porous-Walled Ducts”, *AIAA Journal*, 24(11), 1766-1773, 1986.

29. Traineau, J. C., Hervat, P., and Kuentzmann, P., "Cold-Flow Simulation of a Two-Dimensional Nozzleless Solid-Rocket Motor", AIAA Paper , 86-1447, 1986.
30. Balakrishnan, G., Linan, A., and Williams, F. A., "Rotational Inviscid Flow in Laterally Burning Solid-Propellant Rocket Motors", Journal of Propulsion and Power, 8(6), 1167-1176, 1992.
31. Dunlap, R., Blackner, A. M., Waugh, R. C., Brown, R. S., and Willoughby, P., G., "Internal Flow field Studies in a Simulated Cylindrical Port Rocket Chamber," Journal of Propulsion and Power, 8(6), 1167-1176, 1992.
32. Sabnis, J. S., Madabhushi, R. K., Gibeling, H. J., and McDonald, H., "On the Use of $k-\varepsilon$ " Turbulence Model for Computation of Solid Rocket Internal Flows", AIAA Paper 89-2558, 1989.
33. Tseng, I. S., "Numerical Simulation of Velocity-Coupled Combustion Response of Solid Rocket Propellants", Ph.D. Dissertation, Dept. of Mechanical Engineering, Pennsylvania State Univ., University Park, PA, 1992.
34. Nicoud, F., Poinso, T. J., and Minh, H. H., "Direct Numerical Simulation of a Turbulent Flow with Massive Uniform Injection", 10th Symposium on Turbulent Shear Flows, 3(29), 13-18, 1995.
35. Apte, S. and Yang, V., Unsteady Flow Evolution in Porous Chamber with Surface Mass Injection, Part 1: Free Oscillation, AIAA J., 39(8), 2001.
36. Thermal/Fluid Analysis of Perforated Plates for Transpiration Cooling Liquid Propellant Rocket Chambers, at the site:
http://prc.uah.edu/annual%20reports/fy99_3.pdf#search='Thermal%2FFluid%20Analysis%20of%20Perforated%20Plates%20for%20Transpiration%20Cooling%20Liquid%20Propellant
37. Collier Jr. F. S., and Schetz J. A., Injection into a Turbulent Boundary Layer through Different Porous Surfaces, AIAA Journal, 22(6), 839-841, 1984.
38. Eckert E. R. G., and Cho H. H., Transition from Transpiration to Film Cooling. Int. J. Heat and Mass Transfer, 37, Suppl. 1, 3-8, 1994.
39. Cheng Y. C., Hwang G. J., and Ng M. L., Developing Laminar Flow and Heat Transfer in a Rectangular Duct with One-Walled Injection and Suction, Int. J. Heat and Mass Transfer, 37, 2601-2613, 1994.
40. Robert J. C., Campolina-Franca G. A., Robert P. Pagnier, and Lallemand A., Experimental Study of Transpiration Gas Cooling through a Porous Wall, Revue Generale de Thermique, 37, 89-102, 1997.

41. Yang, J., T., Wang, H., W., Lin, Y., F. and Su, Y., C., Cooling Transience in a sudden-Expansion Channel with Various Wall Transpiration Rate, Proceeding of PSFVIP-4, Chamonix, France, June, 2003
42. Mehendale, A.B. and Han, J.C., Influence of High Mainstream Turbulence on Leading Edge Film Cooling Heat Transfer, ASME paper 90-GT-09, accepted for publication in the Transactions, 1990. [Cited in 45].
43. Karni, J. and Goldstein, R.J., Surface Injection Effect on Mass Transfer From a Cylinder in Cross flow: A Simulation of Film Cooling in the Leading Edge Region of a Turbine Blade, Journal of Turbomachinery, 112, 418-427, 1990. [Cited in 45].
44. Camci, C. and Arts, T., An Experimental Convective Heat Transfer Investigation Around a Film-Cooled Gas Turbine Blade, Journal of Turbomachinery, 112, 497-503, 1990. [Cited in 45].
45. Hoffs, A., Drost, U and Bolcs, A, An Investigation of Effectiveness and Heat Transfer on a Showerhead-cooled Cylinders. At the site: http://lttwww.epfl.ch/publications/pdf/hoffs_drost_bolcs_igti069_1997.pdf#search='hoffs_drost_bolcs_igti069_1997%20effectiveness%20heat%20transfer'
46. Ekkad, S., V., Zapata, D. and Han, J., C., Heat Transfer Coefficients over a Flat Surface with Air and CO₂ Injection through Compound Angle Holes Using a Transient Liquid Crystal Image Method, Journal of Turbomachinery, 119, Issue:3, 40, 1997. At the site: http://www.osti.gov/energycitations/product.biblio.jsp?osti_id=516729
47. Riabov, V., V. Heat Transfer on a Hypersonic Sphere with Diffuse Rarefied-Gas injection, 42nd AIAA Aerospace Science meeting and Exhibit, Reno, Nevada, 1-9, January, 2004.
48. Ogawa, M., Mass Transfer of Mixed Gas Flow Crossing a High Temperature Graphite Cylinder with Chemical Reactions and In-Pore Diffusion, Int. J. Heat Mass Transfer 30(5), 1017-1026, 1987.
49. Kays, W. M. and London, A. L., Compact heat exchangers, 3rd Edition, McGraw-Hill, Inc., New York, 1984.
50. Geankoplis, C., J., Transport processes: Momentum. Heat and Mass, Allyn and Bacon, Inc., 1983.
51. Geankoplis, C., J., Mass Transport Phenomena, Sixth Printing, Edward Brothers, Inc., 1984.
52. Sherwood, T. K. and Pigford, R. L., Absorption and Extraction, 2nd Edition, McGraw-Hill, Inc., New York, 1952.
53. Chilton, T., H. and Colburn, A., P., Mass Transfer (Absorption) Coefficients, Ind. Eng. Chem., 26(11), 1183-1185, 1934.

Table A.1: Properties of Air at $P=101.325$ kPa, $Mwt=28.966$ [8].

T (K)	T (°C)	Density (Kg/m ³)	Viscosity (kg/m.s)
283	9.85	1.2473	1.76867E-05
293	19.85	1.2047	1.81669E-05
300	26.85	1.1766	1.85315E-05
303	29.85	1.165	0.00001864
313	39.85	1.1277	1.91145E-05
323	49.85	1.0928	1.9572E-05
333	59.85	1.06	2.00234E-05
343	69.85	1.0291	2.04688E-05
350	76.85	1.0085	2.08054E-05

Table A.2: Water Density at Different Temperatures[51].

T (°C)	Density (kg/m ³)
25	997.08
30	995.68
40	992.25
50	988.07
60	983.24
70	977.81
80	971.83
90	965.34

Table A.3: Properties of Water Vapor[51].

T (°C)	T (K)	P (kPa)	Density (kg/m ³)
25	298.15	3.169	0.023063
30	303.15	4.246	0.030401
35	308.15	5.628	0.039868
40	313.15	7.384	0.051222
45	318.15	9.593	0.065539
50	323.15	12.349	0.083112
55	328.15	15.758	0.104515
60	333.15	19.94	0.130361
65	338.15	25.03	0.161368
70	343.15	31.19	0.198334
75	348.15	38.58	0.242072
80	353.15	47.39	0.293513

Derivation of Kays and Crawford Correction Equation for the Blowing Flat Plate [3]

When eq. 2.5 is substituted into eq. 2.3, the momentum differential equation for the constant property turbulent boundary layer becomes:

$$\bar{u} \frac{\partial \bar{u}}{\partial x} + \bar{v} \frac{\partial \bar{u}}{\partial y} = -\frac{1}{\rho} \frac{d\bar{P}}{dx} + \frac{\partial}{\partial y} \left((\nu + \varepsilon_M) \frac{\partial \bar{u}}{\partial y} \right) + \frac{1}{\rho} \frac{d\bar{P}}{dx} = 0$$

Under the conditions of no pressure gradient, and apply the Couette flow approximation the above equation becomes:

$$\nu_o \frac{\partial \bar{u}}{\partial x} - \frac{\partial}{\partial y} \left((\nu + \varepsilon_M) \frac{\partial \bar{u}}{\partial y} \right) = 0$$

Let the boundary conditions be

$$\bar{u} = 0, \quad \frac{\tau_o}{\rho} = \nu \left(\frac{d\bar{u}}{dy} \right)_o \quad \text{at } y = 0$$

$$\bar{u} = u_\infty \quad \text{at } y = \delta$$

Integrating once and applying the first boundary condition,

$$\nu_o \bar{u} - \left((\nu + \varepsilon_M) \frac{\partial \bar{u}}{\partial y} \right) = \frac{\tau_o}{\rho}$$

Rearranging, and integrating across the boundary layer,

$$\int_0^{u_\infty} \frac{du}{\nu_o \bar{u} + \tau_o / \rho} = \int_0^\delta \frac{dy}{\nu + \varepsilon_M}$$

that is,

$$\frac{1}{v_o} \ln\left(1 + \frac{v_o u_\infty \rho}{\tau_o}\right) = \int_0^\delta \frac{dy}{v + \varepsilon_M}$$

But note that

$$\frac{v_o u_\infty \rho}{\tau_o} = \beta_f = \frac{v_o / u_\infty}{f}$$

Then

$$\ln(1 + \beta_f) = f \beta_f u_\infty \int_0^\delta \frac{dy}{v + \varepsilon_M}$$

$$f = \frac{\ln(1 + \beta_f)}{\beta_f} \frac{1}{u_\infty} \left(\int_0^\delta \frac{dy}{v + \varepsilon_M} \right)^{-1}$$

This equation is indeterminate for $\beta_f = 0$, but

$$\lim_{\beta_m \rightarrow 0} \frac{\ln(1 + \beta_m)}{\beta_m} = 1.0$$

So,

$$f^o = \frac{1}{u_\infty} \left(\int_0^\delta \frac{dy}{v + \varepsilon_M} \right)^{-1}$$

where superscript o refers to the $\beta_f = 0$ case.

Then if we make the assumption (obviously not proved) that the two integrals are independent of β_f , dividing the two equations yields eq.2.6,

$$\frac{f}{f^o} = \frac{\ln(1 + \beta_f)}{\beta_f} = \varphi(\beta_f) \tag{2.6}$$

Table C.1: Friction Factor Results at Constant β_f

$\beta_f = 0.0042$					$\beta_f = 0.0031$					$\beta_f = 0.0015$				
<i>Exp.</i> <i>No.</i>	T_{air} (°C)	Δh_{cl} (mm)	Δh (cm)	f/f^o	<i>Exp.</i> <i>No.</i>	T_{air} (°C)	Δh_{cl} (mm)	Δh (cm)	f/f^o	<i>Exp.</i> <i>No.</i>	T_{air} (°C)	Δh_{cl} (mm)	Δh (cm)	f/f^o
25	32.5	4.2	10.64	1.430	37	33.0	5.0	11.50	1.291	49	32.6	5.5	10.36	1.078
26	32.8	3.5	8.82	1.408	38	32.8	4.2	9.61	1.278	50	32.6	5.0	9.64	1.089
27	32.9	3.2	8.25	1.418	39	32.7	3.0	7.30	1.293	51	32.4	3.8	7.42	1.097
28	32.8	2.8	7.34	1.418	40	32.8	2.7	6.58	1.297	52	32.4	3.4	6.78	1.108
29	32.5	2.3	6.15	1.406	41	32.8	2.0	5.13	1.282	53	32.3	3.0	6.33	1.150
30	32.5	1.8	4.93	1.427	42	32.8	1.7	4.26	1.298	54	32.2	2.5	5.62	1.143
31	32.6	1.6	4.58	1.425	43	32.6	1.5	3.72	1.313	55	32.3	2.3	4.99	1.145
32	32.5	1.2	3.27	1.404	44	32.6	1.1	2.88	1.300	56	32.3	2.0	4.47	1.166
33	32.4	0.80	2.49	1.407	45	32.5	0.7	1.95	1.302	57	32.3	1.5	3.39	1.180
34	32.2	0.70	2.34	1.422	46	32.6	0.6	1.75	1.305	58	32.4	1.2	2.91	1.194
35	32.2	0.65	1.98	1.409	47	32.7	0.5	1.39	1.296	59	32.5	0.8	1.95	1.176
36	32.2	0.50	1.50	1.399	48	32.6	0.3	0.97	1.239	60	32.5	0.3	0.82	1.092

Table C.2: Friction Factor Results at Constant Re.

<i>Exp. No.</i>	$(Q_{rot.})_{uncorr.}$ (m^3/hr)	Δh (cm)	f/f^o	<i>Exp. No.</i>	$(Q_{rot.})_{uncorr.}$ (m^3/hr)	Δh (cm)	f/f^o	<i>Exp. No.</i>	$(Q_{rot.})_{uncorr.}$ (m^3/hr)	Δh (cm)	f/f^o
61	10.5	10.3	1.094	71	8.0	6.5	1.141	81	4.0	2.5	1.158
62	13.0	11.0	1.168	72	9.0	6.6	1.158	82	5.0	2.6	1.204
63	15.5	11.2	1.189	73	10.5	6.8	1.194	83	6.0	2.6	1.204
64	18.0	11.5	1.221	74	13.0	7.0	1.229	84	7.5	2.7	1.251
65	20.0	11.8	1.253	75	14.0	7.1	1.246	85	8.5	2.7	1.251
66	22.0	12.0	1.274	76	16.0	7.2	1.264	86	10.5	2.8	1.297
67	26.0	12.3	1.306	77	19.0	7.5	1.316	87	11.5	2.9	1.343
68	29.0	12.6	1.338	78	21.5	7.8	1.369	88	13.0	3.0	1.389
69	30.0	13.4	1.423	79	23.0	8.0	1.404	89	14.5	3.1	1.436
70	33.0	13.9	1.476	80	26.0	8.3	1.457	90	16.0	3.3	1.529

- f^o (13446) = 3.5414
- f^o (10151) = 3.7589
- f^o (5900) = 4.2171

Table C.3: Debusschere-Ragland Results of Friction Factor.

$\beta_f = 0.0018$		$\beta_f = 0.0046$		$\beta_f = 0.0069$	
Re	f	Re	f	Re	f
8600	4.75	8950	5.46	9000	6.15
9300	4.70	9450	5.49	9600	6.20
10200	4.45	10200	5.42	10500	5.92
11000	4.35	10750	5.31	10700	5.90
11750	4.25	11250	5.37	11250	5.85
13450	4.03	11780	5.27	11750	5.80
		12350	5.17	12700	5.75
		12750	5.07	13050	5.65
		13200	5.17		
		13600	5.14		

Table C.4: Mass Transfer Raw Data.

Exp. No.	T_{heate} ($^{\circ}C$)	Δm (g)	Time (s)	Δh_{cl} (mm)	T_{air} ($^{\circ}C$)	RH%	$(T_s)_{ava.}$ ($^{\circ}C$)	$Q_{water\ rot..}$ (ml/min)
1	45	54.54	1942	1.94	27.3	50.1	28.599	50
2	49	76.76	1981	1.95	29.1	41.5	31.357	50
3	55	99.75	1884	1.91	28.8	43.2	34.878	50
4	60	127.59	2094	1.91	27.6	41.9	38.028	50
5	64	135.73	1956	1.92	27.8	42.8	40.837	50
6	69	150.75	1854	1.92	27.8	45.8	43.992	50
7	75	84.27	914	1.92	28.0	50.0	47.233	100
8	80	103.95	1007	1.92	28.1	54.4	50.336	100
9	85	115.03	958	1.91	29.8	49.8	53.495	300
10	40	28.20	1587	2.88	29.5	49.5	25.007	200
11	44	47.57	1754	2.89	27.7	50.7	27.437	200
12	50	76.88	1974	2.90	28.1	44.8	30.822	50
13	55	112.26	2243	2.89	27.8	42.5	33.911	100
14	60	133.39	2157	2.90	28.0	41.0	37.164	100
15	65	143.19	2011	2.91	26.9	44.4	40.068	100

Table C.4: (Continued)

16	70	176.64	2028	2.87	27.3	46.5	43.332	100
17	74	101.27	972	2.88	28.8	46.0	46.126	300
18	79	102.12	919	2.89	28.9	50.5	49.225	300
19	85	107.40	814	2.89	28.7	53.3	52.474	300
20	88	242.06	1648	2.89	28.6	52.5	54.735	50
21	40	29.41	1657	4.40	28.6	53.4	24.376	200
22	45	56.24	1925	4.40	27.9	50.2	27.437	200
23	50	55.36	1278	4.42	28.3	44.9	30.279	200
24	54	62.81	1137	4.42	28.3	41.6	32.913	200
25	60	93.90	1298	4.42	28.3	40.2	36.272	200
26	65	65.94	818	4.43	28.4	40.3	39.272	300
27	70	86.14	914	4.43	28.5	42.4	42.299	300
28	75	100.62	952	4.43	28.5	45.8	45.243	300
29	80	102.90	891	4.40	27.8	52.7	48.264	300
30	84	147.16	1080	4.41	28.0	55.1	51.158	200
31	87	148.54	978	4.42	28.2	55.0	52.824	200
32	40	47.05	2449	7.05	28.2	55.5	24.058	100
33	45	66.93	2041	7.05	28.3	50.0	26.843	100
34	50	94.12	1978	7.05	28.3	45.7	29.728	100

Table C.4: (Continued)

35	55	143.56	2478	7.06	28.4	42.3	32.403	100
36	60	71.78	1023	7.02	27.9	41.5	35.350	300
37	65	91.50	984	7.03	28.0	41.0	38.450	200
38	69	113.26	1103	7.04	28.1	42.3	41.212	200
39	74	226.49	1895	7.05	28.3	44.5	43.992	50
40	80	260.88	1970	6.95	27.1	52.8	47.233	50
41	85	275.34	1902	6.97	27.3	56.8	50.336	50
42	40	41.74	2115	0.79	27.0	54.0	26.843	100
43	45	54.71	2029	0.80	27.3	48.5	29.728	100
44	50	90.96	2557	0.80	27.6	43.8	32.913	100
45	55	94.62	2111	0.80	27.5	42.0	36.272	100
46	60	114.91	2145	0.80	27.8	42.0	39.673	100
47	65	76.94	1187	0.80	27.9	44.6	42.994	200
48	70	86.17	1204	0.80	27.5	50.0	46.126	200
49	74	164.53	1871	0.80	28.0	53.4	49.225	50
50	80	103.87	1011	0.80	28.3	54.7	52.650	200
51	85	96.56	928	0.81	28.4	51.2	56.151	200
52	92	117.90	907	1.32	28.3	54.9	59.134	200
53	44	44.85	1703	1.29	26.5	52.2	28.599	200

Table C.4: (Continued)

54	59	57.43	1078	1.30	27.2	42.7	38.450	200
55	65	720.26	9887	1.30	27.2	45.1	41.943	200
56	80	199.59	1841	1.31	28.0	55.5	51.356	300
57	84	213.12	1779	1.31	28.9	51.0	54.436	50
58	90	211.72	1589	1.33	29.0	49.0	57.764	50
59	50	84.90	2169	2.06	27.3	46.3	31.357	50
60	60	122.69	2101	2.05	27.2	42.9	37.600	100
61	71	159.48	1866	2.06	27.4	48.1	44.628	100
62	85	249.68	1806	2.09	29.0	52.5	53.331	100
63	90	244.09	1647	2.09	28.7	50.2	56.423	100
64	45	56.48	1988	2.57	28.6	47.4	28.022	100
65	59	139.29	2451	2.54	27.9	41.0	37.164	100
66	65	192.78	2589	2.54	27.9	42.2	40.456	100
67	70	204.18	2361	2.54	27.9	45.7	43.992	100
68	74	201.55	2004	2.55	28.1	48.8	46.410	100
69	86	199.91	1358	3.11	28.2	55.0	52.824	200
70	55	54.46	992	3.11	28.1	41.7	33.911	200
71	65	106.82	1401	3.11	28.2	41.3	40.068	200
72	70	923.51	9874	3.11	28.3	43.6	42.994	200

Table C.4: (Continued)

73	76	106.50	996	3.11	28.2	48.9	46.689	200
74	79	122.62	1121	3.11	28.1	52.6	48.991	200
75	84	1222.75	8975	3.54	28.3	54.5	51.740	200
76	54	84.30	1546	3.52	27.8	42.8	33.416	200
77	60	84.00	1264	3.54	28.4	40.0	36.722	200
78	69	158.32	1704	3.49	27.2	46.0	42.649	200
79	79	116.76	965	3.57	29.0	49.6	48.753	300
80	84	123.54	883	3.57	29.0	52.4	51.549	300
81	65	85.24	1078	3.46	26.4	45.5	39.673	300
82	45	32.09	1025	5.96	26.9	54.3	26.843	300
83	54	98.73	1798	5.96	27.0	46.0	32.403	100
84	64	202.70	2451	5.97	27.1	43.0	38.450	100
85	73	91.89	862	6.00	27.5	46.1	43.332	200
86	88	178.04	1091	6.02	27.4	57.4	52.295	200

Table C.5: Debusschere - Ragland Results for Mass Transfer [11].

Re	B_m	β_m	$St Sc^{2/3}$	Re	B_m	β_m	$St Sc^{2/3}$	Re	B_m	β_m	$St Sc^{2/3}$
8200	0.016	0.618	0.00454	12690	0.064	0.977	0.00287	14400	0.063	0.987	0.0026
8200	0.103	1.074	0.00313	12690	0.073	1.002	0.00273	14400	0.028	0.778	0.00299
8200	0.091	1.058	0.00304	12690	0.081	1.033	0.00271	14400	0.035	0.862	0.00316
8200	0.071	0.991	0.00326	12690	0.094	1.066	0.00261	14400	0.107	1.099	0.002
8200	0.027	0.766	0.00414	12690	0.016	0.659	0.00402	14400	0.125	1.134	0.00197
8200	0.128	1.146	0.00271	12690	0.026	0.811	0.00324	15450	0.043	0.951	0.00252
10660	0.097	1.079	0.00256	12690	0.051	0.958	0.00302	15450	0.088	1.088	0.00228
10660	0.077	1.015	0.00315	12690	0.065	0.994	0.00278	15450	0.112	1.132	0.00223
10660	0.108	1.095	0.00282	12690	0.087	1.056	0.00258	15450	0.118	1.14	0.00197
10660	0.123	1.127	0.00271	12690	0.012	0.61	0.00355	15450	0.079	1.034	0.00239
10660	0.137	1.158	0.00215	12690	0.029	0.774	0.00346	15450	0.058	0.948	0.0024
10660	0.154	1.189	0.00251	12690	0.024	0.723	0.003	15450	0.048	0.969	0.00273
10660	0.044	0.894	0.00328	12690	0.032	0.877	0.00313	15450	0.076	1.05	0.00234
10660	0.105	1.089	0.00279	12690	0.117	1.122	0.00199	15450	0.012	0.61	0.00352
10660	0.066	0.982	0.00274	12690	0.133	1.149	0.00191	15450	0.029	0.827	0.0028
10660	0.12	1.126	0.00233	12690	0.081	1.072	0.00268	15450	0.02	0.775	0.00318
10660	0.042	0.873	0.00292	14400	0.014	0.602	0.00347				
12690	0.048	0.922	0.0028	14400	0.046	0.901	0.00289				
12690	0.054	0.937	0.00292	14400	0.086	1.052	0.00234				

الخلاصة

توجد دراسات كثيرة عن انتقال الزخم و الحرارة و الكتلة. معظم هذه الدراسات حول السطوح غير النفاذة. من المعلوم دراسات الاسطح المسطحة ان النفخ خلال الطبقة التاخمة يقلل قيم معاملات الانتقال (معامل الاحتكاك و معاملا انتقال الكتلة و الحرارة). في هذه الدراسة تم بحث تأثير النفخ على معامل الاحتكاك و معامل انتقال الكتلة لجريان عمودي على حزمة انابيب مثقبة لغرض النفخ. و تم قياس هذه المعاملات لمديات مختلفة من عدد رينولدز و معدلات نفخ و تم التعبير عنهما بمجاميع خالية من الوحدات.

تم بناء منظومة لغرض هذا البحث و تتكون من قناة هوائية مستطيلة ($20,3 \times 11,3$ سم). تحتوي كذلك على خمسة اسطر من الانابيب المثقبة بترتيب متردد (staggered) مثبتة بشكل متقاطع مع مجرى القناة الهوائية و بأبعاد $1,5$ (للبعدين الطولي و العرضي).

تم قياس معامل الاحتكاك لمدى عدد رينولدز من $5000 < Re < 16,000$ و معدل نفخ يصل الى 4×10^{-3} . وجد من خلال هذه الدراسة ان النفخ يزيد معامل الاحتكاك للانابيب الاسطوانية من 10% و يصل الى 50% اعتمادا على معدل النفخ.

تم حساب معامل انتقال الكتلة لعدد رينولدز من $5000 < Re < 16,000$ و معدل نفخ $10^{-3} < \dot{m}/G_{\infty} < 10^{-5}$. استخدم تعريف قوة الدفع لأنتقال الكتلة للتعبير عن معدل النفخ. تم تطوير صيغتان ناجحتان لأحتواء تأثير النفخ على معامل الكتلة. من الامكان حساب معامل الكتلة للانابيب الاسطوانية في حالات النفخ من خلال حساب معاملات الكتلة لحالات خالية من النفخ و ضربها بمعامل تصحيح ϕ . بالنسبة للصيغة الاولى تم تطويرها لأحتواء التغير في الكثافة خلال الطبقة المتاخمة و كانت الصيغة النهائية المقترحة هي:

$$St_m Sc^{2/3} = \frac{0.51 Re^{-0.5}}{(1 + \beta_m)^{4.7}} \left(\frac{\rho_s}{\rho_\infty} \right)^{0.4}$$

و الصيغة الثانية تعتمد على معامل التصحيح للاسطح المسطحة و الصيغة النهائية للمعادلة هي:

$$St_m Sc^{2/3} = 0.5 Re^{-0.5} \left(\frac{\ln(1 + \beta_m)}{\beta_m} \right)^{9.94}$$

تعطي هاتان الصيغتان نتائج جيدة مع النتائج المختبرية التي تم الحصول عليها و نتائج الدراسات الموجودة في الادبيات.

تم الحصول على تقلص بمعامل الكتلة يصل ال حوالي ٨٠ % في حالات النفخ.

شكر و تقدير

اتقدم بجزيل الشكر و الثناء الى كل من:

- الأستاذة الدكتورة ندى بهجت نقاش و الدكتور محمد نصيف لأشرافهم و توجيههم لي و حرصهم و تقويمهم الثمين طيلة فترة انجاز البحث.
- اهلي و اتقدم لهم بالشكر الخاص و الامتنان لصبرهم و دعمهم لي طيلة سنين الدراسة.
- عمادة كلية الهندسة و قسم الهندسة الكيماوية/ جامعة النهريين لدعمهم المتواصل لنا.
- اساتذة قسم الهندسة الكيماوية و منتسبي القسم و العمادة كافة.

تأثير النفخ خلال الجدران الاسطوانية على معاملات الانتقال

رسالة مقدمة الى كلية الهندسة في جامعة النهرين
و هي جزء من متطلبات نيل درجة دكتوراه فلسفة
في الهندسة الكيمياوية

من قبل

لمى حكمت ياسين

١٩٩٧ بكالوريوس علوم في الهندسة الكيمياوية
٢٠٠٠ ماجستير علوم في الهندسة الكيمياوية

١٤٢٧
٢٠٠٦

جمادى الاخرة
تموز